The accuracy of filtered basis functions for the first principles modelling of defects in semiconductors

by Fadil E. Shrif

A thesis submitted to Newcastle University for the degree of Doctor of Philosophy.
April 2013.

Dedicated to

My family and my parents, without whose support I would never have made it to this stage.

Declaration

This thesis has not previously been submitted by the candidate for a degree in this or any other university.

Fadil Shrif.

April 2013.

Acknowledgements

First of all I thank my God for giving me the strength and guidance during my studies. I would also like to thank my supervisors, Dr. Patrick Briddon and Dr. Jonthan Goss have extended along with much needed motivation, understanding and assistance and support throughout my studies and for allowing me to study in their research group. I will not forget the help you gave me during my studies, and I really appreciate your efforts. Most especially, I would like to thank my (wife and sons), and my Mum and Dad, sisters and brothers for their love and support. Also, to my colleagues and friends in Newcastle University for regular discussion on all things physics, or other things.

Abstract

This work presents the results of calculations using filtered basis functions performed with the *ab initio* modelling program (AIMPRO). The filtration method works by projecting out (filtering) components of a reference basis function that are not required for a description of the occupied states, thereby producing functions that are localised in energy. This leads to a significant reduction in the number of functions that are needed. It is demonstrated that when studying diamond, silicon and defects in these materials, the use of filtered basis sets using just four basis functions per atom can achieve a comparable accuracy to conventional calculations that use 30–40 basis functions. This enables a massive increase in computational efficiency that could have far reaching consequences for first principles modelling calculations.

The accuracy of the filtration method is first examined for the bulk materials diamond and silicon, in which the energy, lattice constant, bulk modulus and band structure are studied. It is shown that the filtration approximation applied with an efficient spatial cut-off is able to reproduce current calculated values for these to a very high degree of accuracy.

A study of the energies of various reconstructed surfaces in diamond and silicon is then presented. It is first demonstrated that the AIMPRO modelling software without filtration reproduces previous published values of surface energies to within about 100 meV per 1x1 surface cell, with this difference being related to different choices for the pseudo-potential and other details of the calculation. It is also demonstrated that

changes of this degree also occur when changing the exchange-correlation functional used to model the surface. In contrast, the use of filtered basis sets changes these energies by only 1–2 meV, one hundred times smaller, indicating the excellence of this approach and showing that filtered basis calculation with efficient cut-off radii are of essentially equal quality to those of conventional localised basis functions.

Finally a series of defect structures in diamond is considered, including both native defects and nitrogen containing defects. Properties studied include formation energies, binding energies, localised vibrational modes, and hyperfine coupling matrices. In all these cases it is shown that the filtration method produces results which closely match those with conventional basis sets and demonstrate that this method has excellent potential for modelling defecting semiconductor structures in the future. The asymptotic speed up of two to three orders of magnitude will then enable a new range of systems with significantly increased size and complexity to be modelled.

Contents

List of Figures

List of Tables

Publications and Conferences

List of Publications

1. **F. E. Shrif**, P. R. Briddon, J. P. Goss, M. K. Atumi, and M. J. Rayson, The Accuracy of filtration basis calculations for the modelling of defects in diamond, in preparation.

2. M. K. Atumi, J. P. Goss, P. R. Briddon, **F. E. Shrif** and M. J. Rayson, Hyperfine interactions at nitrogen interstitial defects in diamond, *J.Phys. – Condens.Matter*, 25, 065802 (2013).

List of Conferences

1. Postgraduate Research Conference 2010, 13 - 14 January 2010, School of Electrical, Electronic & Computer Engineering, Newcastle University, Newcastle upon Tyne, UK.

2. AIMPRO meeting 2010, 19 - 22 April 2010, University of Nottingham, Nottingham, UK.

3. Postgraduate Research Conference 2011, 26 - 27 January 2011, School of Electrical, Electronic & Computer Engineering, Newcastle University, Newcastle upon Tyne, UK.

4. AIMPRO meeting 2011, 13 - 15 June 2011, University of Strathclyde, Glasgow, UK.

5. Postgraduate Research Conference 2012, 25 - 26 January 2012, School of Electrical, Electronic & Computer Engineering, Newcastle University, Newcastle upon Tyne, UK.

Chapter 1

Introduction

1.1 Introduction

The use of computational modelling techniques has become widespread in many scientific subjects, for instance, physics, chemistry and biology. Simulation techniques can be used to analyse many complex problems in science and modern technology. Introducing modelling techniques also has many advantages in industry, for example, saving time and effort, only requiring computers, being safer (e.g. testing aircraft flight), allowing experiments to be more targeted, and allowing behaviour under extreme condition to be investigated safely.

The interest in this thesis is in the modelling of materials. This area of modelling is very important technologically, for example developing an understanding of a material's strength (mechanical applications), optical properties, electronic properties and magnetic properties. Realistic modelling must not be limited to ideal cases (e.g. the conductivity of perfect silicon), but must take into account the complex defects and imperfections in materials as these often dominate properties. For example a small amount of carbon in steel increases its strength; a small concentration of impurities can change the colour of glass (or diamonds); small concentrations of impurities can determine the conductivity of semiconductors. There is also interest in modelling processing, such as the migration of impurities as part of an annealing process for

example. In conclusion, we need the ability to calculate many properties of materials, particularly the total energy as this will determine stability, but also other properties that can link with experiment properties. These are all determined by the interaction between atom nuclei and the electrons (which of course adapt to the chemical environment), and therefore, we need to perform quantum mechanics calculations.

The simulation technique that has been applied within this work is density functional theory (DFT) a technique commonly used in quantum mechanical calculations. This theory has been used as a basic theory in this work using an implementation incorporated in the `AIMPRO` software [12, 13], density functional theory enables what are known as *ab initio* calculations, there are very powerful and can be predictive. Because experimental input is not required by the calculation there are no fitted parameters except the atomic numbers of the atoms present. In an *ab initio* calculation a carbon atom is treated just as a carbon atom, there are no assumptions with regard to the type of its bonding or chemical environment. Diamond, graphite, graphene or carbon nanotubes are thus treated using exactly the same theory. It is the absence of empirical input relating to the properties of these different materials that gives *ab initio* calculations there great predictive powers.

An important consideration in all materials modelling methods is the size of system that has to be modelled to represent the real problem. Many properties are controlled by point defects, that is imperfections in a crystal that may involve only a few (e.g. 1-10) atoms being displaced significantly from their crystalline positions. Such defects can be modelled using a large unit cell of (e.g. 100-200) atoms. Other problems involve surfaces or line defects (e.g. dislocations). These can often require larger unit cells (1000s atoms). It has become clear that a category of problem exists for which a defective solid can be modelled using 100-10000 atom unit cells. The technique of choice for systems of this size is density functional theory (DFT). This is discussed in detail in chapter (2).

1.2 The AIMPRO modelling code and Filtration method

The solution of the equations of DFT is very complex. In this thesis a computer code AIMPRO will be used. AIMPRO is a software package which solves the Kohn-Sham [14, 15] equations of density functional theory and enables it to be applied to solids and molecules [12]. The AIMPRO acronym has been derived from four words (*ab initio* modelling program). Over 20 years, the code has been written by Briddon, Jones and Rayson [16, 17]. The code is discussed in detail in chapter 2, but the main feature is that it performs calculations largely in real space, using localised basis functions. This gives it the ideal character for studies of molecules, such as C_{60} [18, 19]. It can however also be used to model solids by introducing supercells. The supercells used throughout this thesis contain (2–1000) atoms. Speed and time are important -1000 atom cells are still time consuming on modest computing resources; and there is therefore much interest in improving the speed of calculation while maintaining control over the accuracy achieved. Recently, the AIMPRO code has been improved by introducing the filtration method, which uses a filtered basis set. An overview of the computational steps in aimpro is given in figure 1.1. In this thesis, the emphasis is on a comparison of the relative accuracies of the standard and filter diagonalisations. The importance of this is that diagonalisation is the time dominant step in large simulations and filtration can reduce the time for this (by a factor of up to 1000). More details are given in chapter (3). Filtration has been introduced relatively recently and published results have so far focused on total energies of silicon based structures. This thesis will extend the application to another material , diamond and to several other calculated properties. Using the AIMPRO code, one can compute many experimental observables that can be predicted and give an understanding of experimental quantities, such as vibration modes, heat capacity, electronic structure, band structure, surface energy, hyperfine interactions and minimum energy paths, that to enable us to compare the results.

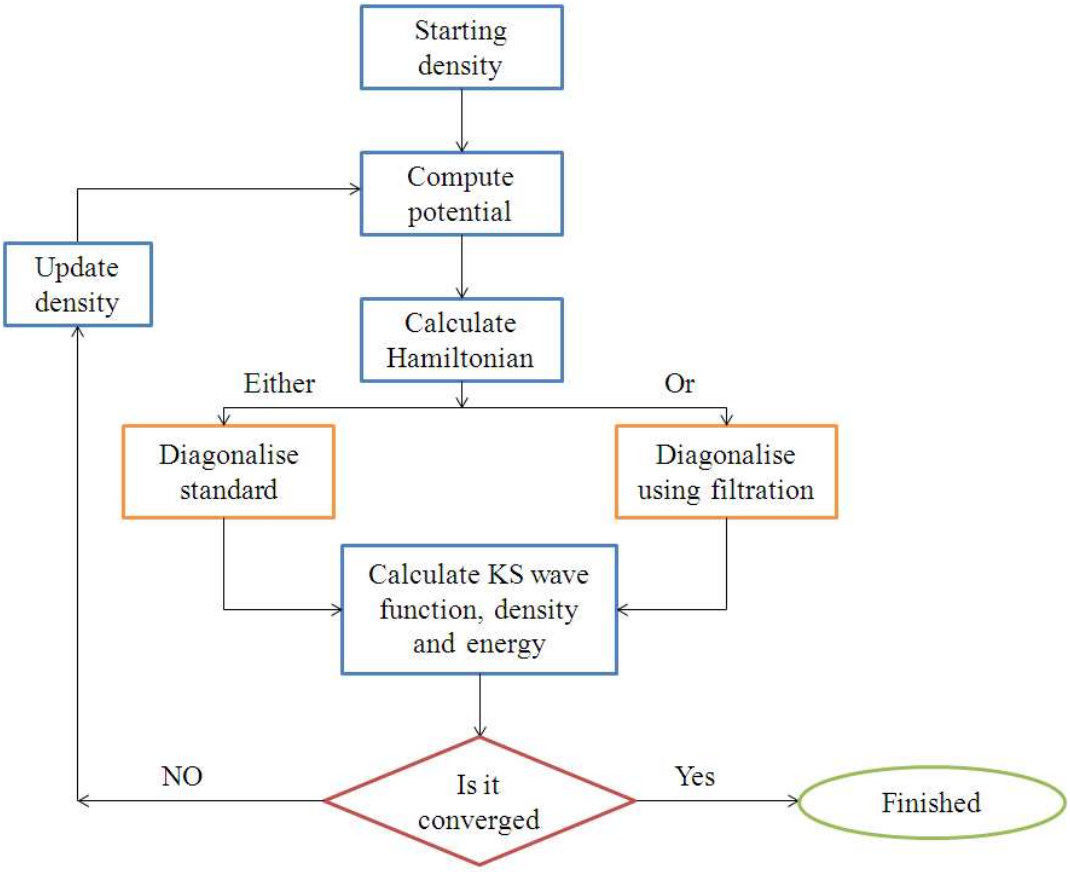

Figure 1.1: Schematic show the working of the AIMPRO simulation process.

1.3 Other simulation methods

In this section, two other approaches which may be used to model large systems will be considered. These are tight binding and the use of generalised Wannier functions.

1.3.1 Tight binding

Originally, the empirical tight binding method was derived as an approximation to the method of linear combination of atomic orbitals (LCAO) [20–22]. The idea is that matrix elements of the Hamiltonian are only evaluated for nearby atoms (within a cut-off radius or even just for nearest neighbours). These elements are usually either fitted or obtained from a very much simplified form of density functional theory

(DFT) [23–25]. The integrals are tabulated as a function of distance and interpolated between these values when a real simulation is done. The Hamiltonian matrix is then diagonalised and the band structure energy found. This is supplemented by a repulsive energy term which is generally fitted, either to experimental data or to results from *ab initio* calculations [26].

There is a superficial resemblance to the filtration approach used in this thesis, but in comparison,

■ In tight binding (TB) calculations, no integrals (matrix elements) are found in the full run (i.e. on the solid or cluster). This makes TB much faster for this part of the calculation, something that was a crucial advantage in the past. However, in most modern codes, integral evaluation does not determine the overall run time when large systems are modelled reducing the advantage that this gives.

■ Diagonalisation, TB uses 4 functions per atom in silicon, much less than a usual `AIMPRO` run but the same as filtration. This part of the calculation does scale as $O(N^3)$, and therefore the conclusion is that the asymptotic speed is the same.

■ The filtration method uses specially constructed functions, whereas TB involves significant assumption and parametrisation, even in the more sophisticated implementations [26].

■ TB does have the advantage of producing very sparse Hamiltonian matrices very quickly, and this could be useful in implementing linear scaling codes.

1.3.2 Generation of Wannier Functions: the ONETEP code

ONETEP [1, 27–29] is a code which uses an apparently similar approach to filtration in that it uses a large starting basis and, in the case of silicon or carbon, generates four basis functions per atom, termed non-orthogonal generalised Wannier functions (NGWFs) from this. There are however important differences. ONETEP uses a starting basis set which is made up from psinc functions. These functions have the advantage of forming a systematic basis set so that the total energy can (in principle, at least) be converged in a simple way. However, they have the disadvantage that

the representation of the NGWFs is less compact, making the code potentially slower and more demanding in terms of memory usage. ONETEP has the ability to perform linear–scaling calculations using these, but this is not what is being considered in this work. Linear scaling approaches to the modelling of large systems work best in systems which have large band gaps, and metals are still problematic for many linear scaling approaches. ONETEP can also operate in a $O(N^3)$ scheme and some comparison with results when run in this mode will be given later in this thesis.

1.4 The choice of diamond

We have chosen diamond due to its interesting properties that enable a broad range of applications, particularly when these properties are combined. In this section, we have used diamond as a material to test the validity and sufficiency of the modified (filtered) basis set. Diamond is classified as an insulator and possesses a wide indirect band gap, compared with other elements in the same group in the periodic table. For example, the band-gap of silicon is around 1.12 eV, and for diamond is around 5.47 eV at 300 K [30]. It is well known that diamond possesses unique properties such as high thermal conductivity, which depends upon the percentage of impurities such as nitrogen [31] and upon the temperature, where its range is 8.95 - 23 W/cm.K at 300 K [32]. This is a very large value compared with the thermal conductivity in silicon, 1.48 W/cm.K at 300 K. Diamond is also characterised by a high optical transparency in the near ultraviolet, visible, and infrared spectra. The filtration method has previously only been tested for silicon, the calculations were in good agreement with other theoretical and experimental results [33], and so application to diamond represents a new test. There is also significant experience in the modelling of this material in Newcastle University. This facilities the further evaluation of filtration by calculating other derived quantities such as hyperfine couplings.

1.5 Thesis Summary

The thesis is divided into three parts, theoretical background, applications and conclusions and future work. Each part is subdivided into chapters and a summary.

1.5.1 Part I -Theory and methodology

Chapter 2 -Theoretical Background and AIMPRO Package

This chapter gives details of the theoretical background which underpins the AIMPRO package, discussing approximations which have been used to solve the many-body Schrödinger equation. This starts with the Born-Oppenheimer approximation, and moves to discussion of the first principle density functional theory (DFT), which has made obvious advances in the provision of computation accuracy. The exchange-correlation term approximations, such as the local density and the generalised gradient approximations are also presented, followed by a brief treatment of the pseudopotential approximation, which replaces the movement of the core electrons of an atom and its nucleus. Ultimately, an extensive dialogue is then given of the execution of quantum mechanical density functional theory using the *ab initio* modelling program (AIMPRO). This comprises the conventional basis set, self-consistency, structure optimisation, the supercell approximation, and Brillouin zone sampling.

Chapter 3 -The Modelling Technique Filtration

This chapter presents the filtration method. It discusses how a small number of chosen filtered basis functions can be used to obtain accurate energies. It also explains the most important parameters, which are required to use the technique, such as the filtration radius, and the filtration temperature.

Chapter 4 -The AIMPRO Calculation of Observables

This chapter discusses the main quantities that have been tested to study the working accuracy and efficiency of the filtered basis approach and also explains the relationship

which links density functional theory with the relevant experimental technique.

1.5.2 Part II -Applications

Chapter 5 -The Accuracy of Filtration applied to Diamond and Silicon

This chapter presents the results associated with the examination of density functional methods by using filtered and unfiltered basis sets to determine the optimised geometries, electronic structures, phonon frequencies, and specific heat capacities of bulk diamond and silicon. The data have been obtained using both the LDA and GGA functionals to enable a conclusion regarding the validity of the modified basis set.

Chapter 6 -Semiconductor surfaces

The chapter shows testing of the filtered basis set on the clean diamond and silicon surfaces, in addition to testing the electron affinity of diamond, and comparing the results with standard *AIMPRO* findings and with experimental values.

Chapter 7 -Native Defects in Diamond

Since many of the defects of interest in diamond are complexes of selected native defects (self-interstitials), in this chapter a study of the properties of native defects is offered. In particular, their energies and geometries are reviewed, all the findings have been computed with the GGA approach, also with filtered and standard basis functions and, where appropriate, compared with each other and with values from the experimental and theoretical publications.

Chapter 8 -Impurities in diamond

The final chapter focuses on testing the filtration method on some impurities in diamond, and examining the validity of the filtered basis function to study some physical and chemical properties, for instance the vibrational modes, electronic structure, band

structure and hyperfine interactions. The calculations have been done with and without filtered basis sets, and comparing with each other and with measured experimental values.

1.5.3 Part III -Conclusions

Chapter 9-Summary

In the final chapter overall conclusions are presented from the thesis. Suggestion for developments of the work are presented and future avenues of research to achieve enhanced methods such as screened exchange, the calculation other properties and the application of the filtration technique to other materials problems.

1.6 Abbreviations

The following abbreviations have been used within this thesis.

Abbreviation	Definition
AIMPRO	*Ab Initio* Modelling PROgram.
DFT	Density Functional Theory.
HF	Hartree-Fock theory.
HK	Hohenberg and Kohn.
KS	Kohn Sham.
BZ	Brillouin Zone.
LDA	Local Density Approximation.
GGA	Generalised Gradient Approximation.
HGH	Hartwigsen-Göedecker-Hutter.
PBE	Perdew, Burke and Ernzerhof.
PW	Plane Wave.
CGOs	Cartesian Gaussian Orbitals.
MP	Monkhorst-Pack.
EA	Electron Affinity.
EPR	Electron Paramagnetic Resonance.
LVM's	Local Vibrational Modes.
ZPE	Zero-Point Energy.
VBM	Valence Band Maximum.
CBM	Conduction Band Minimum.
FPMM	First Principles Marker Method.
FEM	Formation Energy Method.
Filt	Filtered.
Unfilt	Unfiltered.
Abs-errors	Absolute errors
Per-errors	Percentage errors

1.7 Notation

The following notations have been used throughout this thesis.

Notation	Definition
$\hat{H}^{Har}$	Hartree Hamiltonian.
E_{Gs}	Ground State Energy.
T_{s}	Non-interacting Kinetic Energy.
V_{ext}	External Potential.
ε_{xc}	Exchange Correlation Energy.
E_x	Exchange Energy.
E_H	Hartree Energy.
V^H	Hartree Potential.
V_{ps}	Psudopotential.
Ry	Rydberg.
k_B	Boltzmann constant.
C_v	Specific heat capacity at constant volume.
E_{bs}	Band Structure Energy.
E^f	Formation Energy.
E^b	Binding Energy.
E_{VAC}	Vacuum Energy Level.
E_{VBM}	Energy of Valence Band Maximum.
R_c	Cut-off Radius.
μ_i	Chemical Potential.
ψ_{filt}	Filtered Function.
T	Temperature.

Part I

Theoretical Background and AIMPRO Package

Chapter 2

Theoretical Background and AIMPRO Package

2.1 Many-body wavefunction method

In principle, many-body theory [34], can be used to find properties of molecules and other systems for a specific configuration of atoms by solving the many-body Schrödinger equation,

$$\hat{H}\Psi_i = E_i\Psi_i \tag{2.1}$$

where $\hat{H}$ represents the many-body Hamiltonian and Ψ_i represents the many-body wave function, determining the total energy for the i^{th} state. The Hamiltonian operator includes the usual kinetic and potential operators for the system, given by

$$\hat{H} = \hat{T}_e + \hat{T}_n + \hat{V}_{ee} + \hat{V}_{en} + \hat{V}_{nn} \tag{2.2}$$

and, in full, is given by,

$$\hat{H} = -\frac{1}{2}\sum_{i=1}^{N}\nabla_i^2 - \frac{1}{2M_\alpha}\sum_{\alpha=1}^{M}\nabla_\alpha^2 - \sum_{i=1}^{N}\sum_{\alpha=1}^{M}\frac{Z_\alpha}{r_{i\alpha}} + \sum_{i=1}^{N}\sum_{j>i}^{N}\frac{1}{r_{ij}} + \sum_{\alpha=1}^{M}\sum_{\beta>\alpha}^{M}\frac{Z_\alpha Z_\beta}{R_{\alpha\beta}} \tag{2.3}$$

where M_α is the mass of nucleus α, Z_α is the charge on nucleus α, $R_{\alpha\beta} = |R_\alpha - R_\beta|$ where R_α is the coordinate of nucleus α , and $r_{ij} = |r_i - r_j|$ where r_i is the coordinate

of electron i. The parameters($e, \hbar, m$ and $4\pi\epsilon_\circ$) are unity in the atomic units (a.u.) system, where 1 a.u of energy is 2Ry (Rydberg) = 27.211652 eV = 4.359748×10^{-18} J), and 1 a.u of length is equivalent to (1 Bohr radius = 0.5291 Å= 5.291×10^{-11} m). Solving the Schrödinger equation for larger systems, which contain many electrons and ions is an impossibly complicated problem, and in order to achieve the high accuracy in the calculations, we shall also need to use a significant series of approximations. The next section will present some of them.

2.1.1 The Born-Oppenheimer Approximation

Fundamentally, the Born-Oppenheimer approach [35] is based upon the separation of the motion of nuclei and electrons as a consequence of their different masses. Since the electron mass is thousands of times smaller than the nuclei mass, the motion of the nuclei is much slower than that of the electrons. Therefore, it is possible to consider that the electrons are moving in a potential field generated by fixed nuclei. By separating the total wave function, which describes the movement of the nuclei and the electrons, into two terms ($\Psi_{\text{elec},R}(r), \Psi_{\text{nucl}}(R)$), the mathematical formula for this approach is written as shown,

$$\Psi_T(r, R) = \Psi_{\text{elec},R}(r)\Psi_{\text{nucl}}(R) \tag{2.4}$$

Here, $\Psi_{\text{elec},R}(r)$ is the wave function of the electrons, calculated assuming the nuclei are fixed at positions R, and $\Psi_{\text{nucl}}(R)$ is the wave function for the nuclei, r and R represent all coordinates of the electrons and nuclei. As a result, the problem (2.2, 2.4) is reduced to the simpler equation:

$$\hat{H}\Psi_R(r_1, r_2, ..., r_N) = E\Psi_R(r_1, r_2, ..., r_N) \tag{2.5}$$

$$\hat{H} = \frac{1}{2}\sum_{i=1}^{N}\nabla_i^2 + \frac{1}{2}\sum_{i\neq j}\frac{1}{\mid r_i - r_j \mid} - \sum_{i,a}\frac{Z_a}{\mid r_i - R_a \mid} \tag{2.6}$$

with a second equation available to calculate $\Psi_{nucl}(R)$. The potential energy term in the Schrödinger equation is still complicated and does not allow us to treat the electrons as independent. A further approximation is thus made in the next section.

2.2 The Hartree and Hartree-Fock schemes

Hartree simplified the above equation, by proposing a form for the wave function:

$$\Psi(r_1, r_2, ...r_N) = \Psi_1(r_1)\Psi_2(r_2)\Psi_3(r_3) \tag{2.7}$$

which corresponds to the idea of placing on electron into each state (i.e. first electron goes into Ψ_1, second one goes into Ψ_2). This enables a simplification of equations 2.5 and 2.6 to a one electron equation for the states $\Psi_1(r_1), \Psi_2(r_2)$,...

$$\hat{H}^{Har}\Psi_i(r) = E_i(r)\Psi_i(r) \tag{2.8}$$

where

$$\hat{H}^{Har} = -\frac{1}{2}\nabla^2 + V^H(r) - \sum^{j\alpha} \frac{Z_\alpha}{|r - R_\alpha|} \tag{2.9}$$

and where the Hartree potential $V^H(r)$ is given by,

$$V^H(r) = \sum_i \int \frac{|\Psi(r')|^2}{|r - r'|} dr' \tag{2.10}$$

This has produced a one electron equation, which can be solved much more easily.

The Hartree-Fock method is an attempt to improve the Hartree approach [36–39] to compute the ground state wave function and ground state energy. The Hartree-Fock approximation has described the wave function by a Slater determinant [40, 41], given by,

$$\Psi(r_1, r_2....., r_N) = \frac{1}{\sqrt{N!}} \begin{vmatrix} \Psi_1(r_1) & \Psi_1(r_2) & ... & \Psi_1(r_N) \\ \Psi_2(r_1) & \Psi_2(r_2) & ... & \Psi_2(r_N) \\ ... & ... & ... & ... \\ ... & ... & ... & ... \\ \Psi_N(r_1) & \Psi_N(r_2) & ... & \Psi_N(r_N) \end{vmatrix} \tag{2.11}$$

This approximation leads to another type of potential (the exchange potential) influencing the electrons, which reflects the Pauli exclusion principle associated with the anti-symmetrised wavefunction. The exchange energy contribution then may be

written,

$$\left\{-\frac{1}{2}\nabla^2 + V(r) + \sum_j \int \frac{\mid \Psi_j(r^{'}) \mid^2}{\mid r - r^{'} \mid} dr^{'}\right\} \Psi_i(r) + \sum_j{}^{'} \Psi_j(r) \int \frac{\mid \Psi_j^*(r^{'})\Psi_i(r^{'}) \mid}{\mid r - r^{'} \mid} dr dr' = \epsilon_i \Psi_i(r) \tag{2.12}$$

where the sums are over occupied states and the prime indicates only states of the same spin as ψ_i should be summed over, ϵ_i represents one-electron energy eigenvalues.

The exchange energy term in the Hartree-Fock equation has resulted from the correlated movement of the electrons. The appearance of this term in the total energy equation complicates the calculations. Density functional theory is one approach to develop these theories further.

2.3 Density Functional Theory (DFT)

The Thomas-Fermi method was the first DFT based method and was first proposed in 1927 [23–25], well before the fundamentals of density functional theory were presented by Hohenberg and Kohn in 1964 [15]. The basic variable in this theory is the electron density $n(r)$ and not the many-electron wave function [42]. Since then, this theory has been applied to many systems, and DFT has been become one of the most widely used tools to determine the ground state energy and properties of many atoms, molecules and solids. The simplest system to which it can be applied is an electronic system with a non-degenerate ground state. Since, the charge density $n(r)$ is considered as the basic variable, we need to have it as a function of three variables the Cartesian coordinates (x, y and z), instead of the $3N$ variable problem represented by equation 2.2

2.3.1 The Hohenberg Kohn Theorem

Hohenberg and Kohn (HK) developed density functional theory from two important fundamental theorems.

The first theorem :

For a system with a non-degenerate ground state, the external potential $V(r)$ is determined to within an additive constant by the electron density $n(r)$. This means that in principle the total energy E can be written down as a functional of density: $E[n]$ [13].

This can be seen as follows. Suppose have a system of N particles in the ground state, with a wave function Ψ_1 and a charge density $n(r)$, the electrons move in an external potential $V_1(r)$ and have an energy E_1. Also suppose that there exists another system having an external potential $V_2(r)$, with wave function Ψ_2 and total energy E_2. However, we will assume the electron density of this second system is identical to that of the first system, namely $n(r)$. The Hamiltonians of two systems are related by:

$$\hat{H}_1 - \hat{V}_1(r) = \hat{H}_2 - \hat{V}_2(r) \tag{2.13}$$

Clearly,

$$E_1 < \langle \Psi_2 | H_1 | \Psi_2 \rangle \tag{2.14}$$

by the usual variation principle. Now,

$$\hat{H}_1 = \hat{H}_2 + V_1 - V_2 \tag{2.15}$$

So that,

$$E_1 < \langle \Psi_2 | \hat{H}_2 | \Psi_2 \rangle + \langle \Psi_2 | V_1 - V_2 | \Psi_2 \rangle \tag{2.16}$$

or

$$E_1 < E_2 + \int n(r)(V_1 - V_2)dr \tag{2.17}$$

Similarly,

$$E_2 < \langle \Psi_1 | H_2 | \Psi_1 \rangle \tag{2.18}$$

$$E_2 < E_1 + \int n(r)(V_2 - V_1)dr \tag{2.19}$$

Adding (2.17 and 2.19) gives

$$E_1 + E_2 < E_2 + E_1 \tag{2.20}$$

This result is logically impossible. This means that it can not be possible for the two systems to both have the same density $n(r)$. In other words the external potential and therefore the energy E are uniquely determined by the density, and therefore, the charge density $n(r)$ can be used as the basic variable in density functional theory (DFT).

The second theorem:

If the functional $E[n]$ is known, the charge density can be found as that charge density which minimizes $E[n]$ subject to the constraint that $n(r)$ is consistent with an N particle density (e.g $n > 0$; n is normalised correctly) [15].

This can be seen as follows, clearly the true ground state energy can be written as,

$$E_{GS} = \lim_{\Psi} \langle \Psi | \hat{H} | \Psi \rangle \tag{2.21}$$

This can be written as,

$$E_{GS} = \lim_{n} E[n] \tag{2.22}$$

where

$$E[n] = \lim_{\Psi \to n} \langle \Psi | \hat{H} | \Psi \rangle \tag{2.23}$$

or in other words $E[n]$ has been minimised with respect to all wave functions consistent with a given n(r).

Once these theorems are accepted, the obvious question is: what is the formula $E[n]$? If this is known, the energy can be calculated.

Clearly, we may write,

$$E_v[n(r)] = \int V(r) n(r) dr + F[n(r)] \tag{2.24}$$

where

$$F[n(r)] = \langle \Psi | (T + U) | \Psi \rangle \tag{2.25}$$

where $F[n(r)]$ is a universal functional, T and U are operators of the kinetic energy and electron-electron interaction energy, respectively. Clearly, $F[n]$ is a large term as

it includes the electron-electron interaction. We may write

$$F[n] = \frac{1}{2}\int \frac{n(r_1)n(r_2)dr_1dr_2}{|r_1 - r_2|} + G[n(r)] \tag{2.26}$$

where $G[n(r)]$ is a universal function of the density $n(r)$. The important step is that G will be more easily approximated than $F[n]$. However, direct approximation of $G[n]$, by HK, was not successful. Instead, progress was made by Kohn and Sham one year later.

2.3.2 The work of Kohn and Sham

Initially, Hohenberg and Kohn tried to develop a formula for $E[n]$ based on slowly varying charge densities. This was not successful and in 1966, Kohn and Sham published a paper in which they described a new idea to solve this problem by introducing another system which involves N non-interacting electrons in an external potential $V_{\text{ext}}(r)$, so that the charge density in that system is the same as the charge density in the interacting system i.e.

$$\sum_{\lambda=1}^{N} |\Psi_\lambda(r)|^2 = n(r) \tag{2.27}$$

where N is the number of electrons. The wavefunctions $\Psi_\lambda(r)$ can be used to compute the kinetic energy $T_s[n(r)]$ of the non-interacting system, which will then be close to the correct kinetic energy of the interacting system. Thus, the total energy is written as follows:

$$E_{\text{total}}[n(r)] = T_s[n(r)] + U_{\text{ext}}[n(r)] + E_H[n(r)] + E_{\text{xc}}[n(r)] \tag{2.28}$$

where T_s represents the kinetic energy of the non-interacting system

$$T_s[n(r)] = \sum_{\lambda=1}^{N} \langle \Psi_\lambda | -\frac{1}{2} \bigtriangledown^2 | \Psi_\lambda \rangle \tag{2.29}$$

The second term in equation (2.28) is the energy associated with the interaction between the electrons and the external potential and that is:

$$U_{ext} = \int V_{ext}(r)n(r)dr \tag{2.30}$$

The third term in (2.28) is the Hartree energy which is given by,

$$E_H[n(r)] = \frac{1}{2}\int \frac{n(r_1)n(r_2)}{|r_1 - r_2|} dr_1 dr_2 \tag{2.31}$$

A last term is $E_{xc}[n(r)]$ which represents the exchange and correlation energy. For more details see for example [14, 42], and the following section. $E_{xc}[n(r)]$ is hard to find and an approximation must be developed, for this (see next section).

2.4 Approximations for $E_{xc}[n]$

2.4.1 Local Density and Local Spin Density Approximations

The local density approximation (LDA) [14, 43, 44] is one of the most important approximations proposed to study electronic systems, which have a zero spin. The LDA expresses the exchange-correlation energy (E_{xc}), of the electronic system by,

$$E_{xc}^{\mathrm{LDA}}[n(r)] = \int n(r)\varepsilon_{xc}[n(r)]dr \tag{2.32}$$

where $\varepsilon_{xc}[n]$ represents sum of the exchange $\varepsilon_x(n)$ and correlation $\varepsilon_c(n)$ energies per electron for a homogeneous electron gas. It can be shown that the total exchange energy is,

$$E_x = -\frac{3}{4}\left(\frac{3}{\pi}\right)^{\frac{1}{3}} n^{\frac{4}{3}} \tag{2.33}$$

The LDA may then written as,

$$E_x[n(r)] = -\frac{3}{4}\left(\frac{3}{\pi}\right))^{\frac{1}{3}} \int [n^{\frac{4}{3}}(r)]dr \tag{2.34}$$

The correlation energy per electron in a homogeneous electron gas in harder to determine, but an approximation to this can be found [45]. The LDA is formed by assuming that the homogeneous electron gas formula $\varepsilon_{xc}[n]$ can be used as in 2.32.

Von Barth and Hedin extended this to a spin polarized system [43], where $n(r)$ represents the charge density, that possessing the spin-up ($n_\uparrow$) and spin-down ($n_\downarrow$) electron densities, respectively.

$$E_x[n(r)] = -\frac{3}{2}\left(\frac{3}{4\pi}\right)^{\frac{1}{3}} \int \left(n_\uparrow^{\frac{4}{3}}(r) + n_\downarrow^{\frac{4}{3}}(r)\right) dr \tag{2.35}$$

2.4.2 Generalised Gradient Approximation

Owing to the appearance of some inadequacies in the LDA, the generalised gradient approximation attempted to improve this by addition of another factor to Eqn (2.32) by modifying the LDA expression as to become,

$$E_{xc}^{\mathrm{GGA}}[n(r)] = \int n(r)\varepsilon_{xc}[n]f_{xc}[n_{\uparrow}(r), n_{\downarrow}(r), |\nabla n_{\uparrow}(r)|, |\nabla n_{\downarrow}(r)|]dr \tag{2.36}$$

The GGA therefore includes a factor f_{xc} to include higher orders in the gradient of the charge density, in order to give more accuracy to the exchange correlation contribution. A popular approximation of this form has developed by Perdew, Burke and Ernzerhof [PBE] [46]. In fact the GGA does improve binding energies for small molecules. It generally slightly weakens the strength of bonds leading to slightly larger lattice constants and smaller bulk modulii than the LDA (but still very close to experiment). The band gap however is not improved.

2.5 Pseudopotentials

One of the extremely significant components in $ab-initio$ methods used to model the properties of many body systems is the pseudopotential [47]. Core electrons do not play a significant direct role in chemical bonding they largely retain the wave functions that describe them in atoms. In contrast, valence electrons in atoms have wave functions which overlap neighbouring atoms and hence control the strengths of bonds. It is desirable for a calculation to take into account the effect of core electrons on the valence shells without the need to calculate them explicitly [47,48]. This is done by replacing the $-\frac{Z}{r}$ potential by a pseudopotential (see Figure 2.1). This removes the fast oscillations in the valence states and this in turn makes it much easier to expand them in terms of basis functions (see section 2.8).

We therefore replace the nuclear potential $-\frac{Z}{r}$ by a pseudopotential $V_{\mathrm{ps}}(r)$. This potential is sensed by valence electrons and in this way accounts for the effect of the core electrons. On the other hand, the approximation of the pseudopotential has

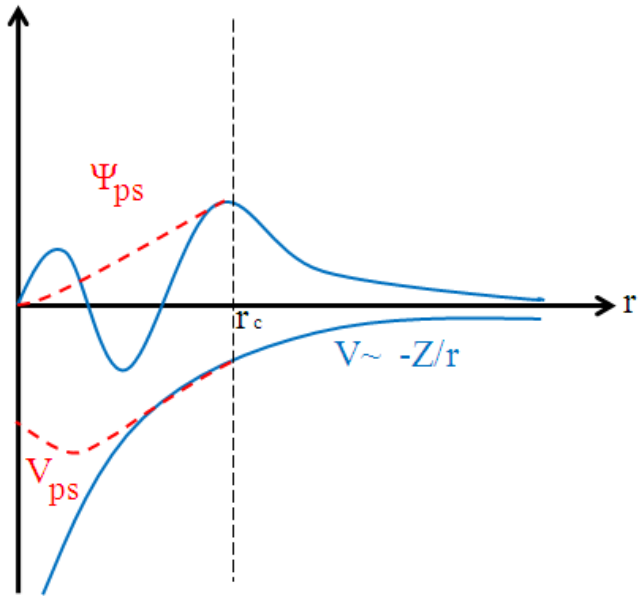

Figure 2.1: Schematic illustrating the pseudo-wave function (top) and the pseudopotential (bottom) core electrons. The cut-off radius r_c indicates the defined region at which point the systems must match. The pseudo-wave function and potential are plotted with a red line whilst the true all-electron wave function and core potential are plotted with the blue lines.

some disadvantages, particularly in the associated calculations of certain quantities which require details of the core states, for instance hyperfine tensors. The idea of the pseudopotential is based on a number of assumptions, first one is a frozen core, that the wave functions of the core states are supposed to be unaffected by the local environment of the atom, so that this supposition enables the pseudopotential to be transferable between systems. The second supposition assumes the exchange-correlation energy E_{xc} can be split into contributions from core electrons and valence electrons :

$$E_{\mathrm{xc}}(n_{\mathrm{c}} + n_v) = E_{\mathrm{xc}}(n_{\mathrm{c}}) + E_{\mathrm{xc}}(n_v) \tag{2.37}$$

where n_{c} represents the core electron density, n_v represents the electron density. This assumption is wrong if there is overlap between the core electrons and valence electrons

wave functions [49–51]. The pseudopotentials used throughout this work are developed by Hartwigsen, Goedecker and Hutter [51](HGH).

2.6 Basis sets

One of the most significant features of any first principle modelling code is the choice of basis set functions used to expand the Kohn-Sham states. Plane waves (PW) and Cartesian Gaussian functions are possibly the most popular options to use for a representation of the basis functions [52]. We will here focus more on Gaussian functions for their importance in this study. A wavefunction ψ_λ is expanded in terms of basis functions thus;

$$\psi_\lambda = \sum_i C_i^\lambda \phi_i(r) \tag{2.38}$$

where ϕ_i represents on uncontracted Cartesian Gaussian function, where these functions are used to build the basis set (primitive). They are given by the following equation,

$$\phi_i(r) = (x - R_{ix})^{n_1}(y - R_{iy})^{n_2}(z - R_{iz})^{n_3} \exp[-\alpha_i(r - R_i)^2] \tag{2.39}$$

where n_1, n_2 and n_3 are positive integers. If these integer numbers are all zero, the function corresponds to an s-orbital and has spherical symmetry, an orbital of P_x symmetry has $n_1 = 1$, otherwise zero, whilst, if $\sum n_i = 2$ the orbitals correspond to the five d-like orbitals and one s-like orbital. R_i indicates the centre of the function and is generally chosen to be an atom location, α_i is an exponent with controls the width of the Gaussian type orbital. For each atom one must specify the Gaussian functions but this requires considering both the exponents and their coefficient functions in 2.39. To yield 4 functions for angular-momentum up to $\ell = 1$ or 10 functions for up to $\ell = 2$ involves multiplying the function $\exp[-\alpha_i(r-R_i)^2]$ by all their factors of the Cartesian (n_x, n_y, and n_z), where the $n_x + n_y + n_z \leq l$, thus, one can be illustrated briefly by this example. We typically label the basis sets as ($ddpp$). The four letters indicate the use of 4 exponents, where the first and second letters (dd) represent exponents which

have 10 functions for each of them and the last two letters (pp) have 4 functions for each of them. The overall basis therefore has 28 functions.

The Cartesian Gaussian Orbitals (CGOs) have some advantages and drawbacks. The first advantage is the low number of functions required, for instance, if using between 20 to 40 functions per atom, the CGOs will give an acceptable result, in contrast to the plane waves, where a larger number of basis functions are used. Another important characteristic is the flexibility (adaptability) where additional basis set functions can be placed on any atom within the system. For example, if the system has an extra atom, such as an impurity with a higher angular-momentum, such as f-orbitals, the CGOs enables us to treat that defect by putting additional functions on that atom only. The rapid decay is another significant advantage for the CGOs, this feature is very useful in reducing the number of the elements of the Hamiltonian matrix which we store. On the other hand, one of the disadvantages of the CGOs is especially when we are deal with large numbers of basis functions levels, for example, if two basis functions with a similar exponents are placed on the same atom this will make the calculation unstable [52].

2.7 Self-consistency

Self-consistency is a process by which charge is redistributed around the system to obtain the minimum energy. The process is

1. start with an input density $n_0^{in}(r)$. Solve the Kohn-Sham equations, and determine the output density, $n_0^{out}(r)$ from the Kohn-Sham states.

2. An updated density is chosen for the input density of the next iteration, i.e. $n_1^{in}(r)$. A simple choice would be:

$$n_1^{in}(r) = n_0^{in}(r) + \alpha(n_0^{out} - n_0^{in}) \tag{2.40}$$

with a suitable value of the constant α. Typically $\alpha \sim$ 0.1-0.3.

3. An improvement is the use of an optimised α, rather than fixed α, this is achieved for example by the DIIS method, e.g. Pulay [53], Bowler and Gillan [54].

4. This method proved unstable in certain situations, for example large metallic cells, or strongly inhomogeneous systems. As a result a preconditioning operator is introduced:

$$n_1^{in}(r) = n_0^{in}(r) + \alpha \hat{P}[n_0^{out} - n_0^{in}] \tag{2.41}$$

The details of a suitable operator $\hat{P}$ are given in the work of Kresse and Furthmuller [55], and this operator has been used in this work.

2.8 Structural optimisation

Structural optimisation is the process by which atoms are moved to minimise the energy, this will result in the equilibrium structure. To do this the forces on the atoms are calculated,

$$f_{i\alpha} = -\frac{\partial E}{\partial R_{i\alpha}} \tag{2.42}$$

where $f_{i\alpha}$ is the α component (x, y and z) of the force on atom i [13]. The atoms can be relaxed using a series of line minimisations:

$$R'_{i\alpha} = R_{i\alpha} + \omega f_{i\alpha} \tag{2.43}$$

where ω is chosen to minimise the energy. This method, the steepest descent can be slow to converge and so the conjugate gradient [56, 57] is used instead. Here we use

$$R'_{i\alpha} = R_{i\alpha} + \omega d_{i\alpha} \tag{2.44}$$

where $d_{i\alpha}$ is a search direction determined from the force in the current and previous iterations [57]. Typically structures are optimised until the change in energy between iterations is smaller than 10^{-5} Ha, and forces are below 10^{-4}a.u.

2.9 Supercell technique

A supercell is usually a large unit cell created by putting together many primitive unit cells, for example in diamond, the conventional cell has 8 atoms, but supercells used for modelling point defects may have 64, 216, 512 or 1000 atoms. This is important as a single defect placed in a large unit cell will be separated from the corresponding defect in neighbouring cells by a distance large enough to ignore the resulting interactions. The advantage gained by this is that periodic boundary conditions can still be used to model a periodic problem, so that the crystal can still be described by a small number of atoms in a repeating unit cell.

2.10 Brillouin Zone sampling

To calculate many observables within the supercell framework, one must complete a Brillouin-zone (BZ) integration. This is needed in order to compute the total energy, and charge density. For example,

$$n(r) = \sum_{\lambda k} |\Psi_{\lambda k}|^2 \tag{2.45}$$

where λ the labels occupied bands (including spin) and k all allowed values in the Brillouin zone. Clearly, the number of allowed values of k is equal to the number of unit cells in the crystal (impossibly large number). As a result, a smaller number of sampling points are chosen to approximate this sum:

$$n(r) = \sum_{\lambda \alpha} \omega_\alpha |\Psi_{\lambda k_\alpha}|^2 \tag{2.46}$$

where different prescriptions are given for the special point k_α and weights ω [58, 59]. In this work the points k_α defined by Monkhorst and Pack [60] are used. An $n_1 \times n_2 \times n_3$ grid of points having the same symmetry as the lattice is used. Typically for a 216 atom diamond cell, a $2 \times 2 \times 2$ grid is sufficient to converge the energy and this is referred to as an MP 2^3 grid elsewhere in this thesis.

2.11 Conclusion

In this chapter some methods of treating many electron systems have been presented, with attention focusing on DFT, and pseudo-potentials. The next chapter will present the filtration method, which presents a new type of basis function (filtered basis function).

Chapter 3

The Modelling Technique `Filtration`

3.1 Introduction

The simulation method (Filtration) has been introduced into the `AIMPRO` code by Rayson and Briddon in Newcastle in 2009. The main idea in this technique is to optimise the generation of basis functions so that between 2-4 basis functions per atom is sufficient in diamond or silicon, and to filter out the elements of high energy states, which have no significant role in the properties of the ground state of the material. The Gaussian function is the fundamental starting point to build these functions for its features, such as rapid decay, flexibility and a capacity for small memory requirement. This technique creates a new basis set (filtered basis set), that contains admixtures of the atomic (s, p, d and f or g) basis functions. The filtration method enables us to increase the number of the atoms in the system being modelled up to 10,000 atoms, minimising the running time of solving the eigenvalues (Hamiltonian matrix), increasing the speed up of the computational processes, whilst maintaining the accuracy of the calculations, and hence allowing simulation of a larger number of atoms.

3.2 The concept of the filtration method

This method uses an automated projection scheme to produce a small number of basis functions that gives a good description of the occupied states, and for elements like C or Si produces a basis set with 4 functions per atom. This technique produces quite similar results in terms of accuracy to calculations which use 28 functions for each atom. As the time taken is proportional to N^3 this will asymptotically make the run $(\frac{28}{4})^3$ times faster, also it could obtain an higher accuracy in the calculations in a shorter time.

3.2.1 The filtration basis set technique

In `AIMPRO` the solutions to the KS equations are expressed in terms of ϕ_i a set of localised basis functions:

$$\psi_\lambda(r) = \sum_\lambda c_{i\lambda}\phi_i(r) \tag{3.1}$$

where λ is the energy level, and $c_{i\lambda}$ points to the coefficients of the energy level. For more detailed discussion of this technique see for example Ref [13]. The filtered basis is defined in terms of the primitive basis:

$$\phi_I^{'}(r) = \sum_i K_{iI}\phi_i(r); [I = 1, 2, ..., n'] \tag{3.2}$$

where K_{iI} is the filtration coefficients matrix. This work will provide an automatic construction method for the optimal set of the coefficients K_{iI} without returning to atomic results. This technique enables us to filter the elements of the high-energy non-desirable states from the primitive basis to give a much smaller basis which still spans the occupied subspace adequately. This approximation is built on the contracted diagonalisation algorithm of Neuhauausev [61] and the Fermi operator projection method of Goedecker [62].

3.2.2 The overall process in the calculation

The filtration calculation works as follows:

1. First the Hamiltonian matrix, $H_{ij} = \int \phi_i \hat{H} \phi_j dr$ and overlap matrix $S_{ij} = \int \phi_i \phi_j dr$ are found for the system being modelled.

2. Cycle through all atoms. For each atom:

   (a) Identify all basis functions atoms with centres which lie within a cut-off radius R_c of the given atom.

   (b) Extract the parts of the matrices H_{ij} and S_{ij} which correspond to these.

   (c) Solve the eigenvalue problem 3.9 for this small set of basis functions to determine the charge density matrix b_{ij}.

   (d) The corresponding row of K_{iI} is obtained from a column of this matrix .

The size of the eigenvalue problem in (c) above is $n \sim 500 - 1000$. The amount of work is $N_{atom} \times 3n^3$ which clearly scales linearly with N_{atom} and will not be important for large N_{atom} [33].

3.2.3 Primitive set$\longrightarrow$ subset transition

After executing the last stage at each atom, this will be create a new matrix (K), therefore, to form the subspace eigenproblem, one can use this equation.

$$H'_{IJ} = \int \phi'_I(r) \hat{H} \phi'_J(r) dr \tag{3.3}$$

$$= \sum_i^n \sum_j^n K_{iI} K_{jJ} \int \phi_i(r) \hat{H} \phi_j(r) dr \tag{3.4}$$

If we define

$$H_{ij} = \int \phi_i(r) \hat{H} \phi_j(r) dr \tag{3.5}$$

then,

$$H'_{IJ} = \sum_i^n \sum_j^n K_{iI} K_{jJ} H_{ij} \tag{3.6}$$

$$H' = K^T H K \tag{3.7}$$

To construct the overlap matrix, we follow the same steps,

$$S' = K^T S K \tag{3.8}$$

so, the subspace eigenproblem is given by

$$H^{'}c^{'} = S^{'}c^{'}\Lambda^{'} \tag{3.9}$$

where $\Lambda^{'}$ is a diagonal matrix containing the eigenvalues. This may be solved by using direct diagonalisation, thus the subset eigenproblem will be have the smallest basis calculations, for instance, each carbon or silicon atom in the approach of pseudopotential will have just four functions, so we can be calculated the density matrix $b^{'}_{IJ}$ of the subset directly together with the band structure by using this equation [33].

$$b^{'}_{IJ} = \sum_{\lambda} f(\varepsilon_{\lambda}) c^{'}_{I\lambda} c^{'}_{J\lambda} \tag{3.10}$$

where $f(\varepsilon_{\lambda})$ gives the occupancy of a KS state of energy ε. The band structure energy is then,

$$E_{bs} = \sum_{\lambda} f(\varepsilon_{\lambda})\varepsilon_{\lambda} = \sum_{IJ}^{n'} b^{'}_{IJ} H^{'}_{IJ} \tag{3.11}$$

3.2.4 Subset$\longrightarrow$ primitive set transition

In order to transition the density matrix $b^{'}_{IJ}$ which was formed in the subspace $b^{'}_{IJ}$ to the primitive set we are using, we proceed thus:

$$n(r) = \sum_{IJ}^{n^{'}} b^{'}_{IJ} \phi^{'}_{I}(r) \phi^{'}_{J}(r) \tag{3.12}$$

$$n(r) = \sum_{IJ}^{n^{'}} \sum_{ij}^{n} K_{iI} K_{jJ} b^{'}_{IJ} \phi_i(r) \phi_j(r) \tag{3.13}$$

$$n(r) = \sum_{ij}^{n} b_{ij} \phi_i(r) \phi_j(r) \tag{3.14}$$

where

$$b_{ij} = \sum_{IJ}^{n'} b^{'}_{IJ} K_{iI} K_{jJ} \tag{3.15}$$

This is in the form of a matrix product:

$$b = K b^{'} K^{T} \tag{3.16}$$

where the matrices b, b' and K are all sparse

3.3 The filtration process

The filtration process begins by describing the Kohn-Sham levels in terms of the Gaussian basis set, $\phi_i(r)$, and by inverting the equation 3.1, we will obtain:

$$\phi_i(r) = \sum_\lambda d_{i\lambda}\psi_\lambda(r) \tag{3.17}$$

where

$$d_{i\lambda} = \int \psi_\lambda(r)\phi_i(r)dr = \sum_j S_{ij}c_{j\lambda} \tag{3.18}$$

then, the filtered function $\phi_{\mathrm{i}}^{'}$(r) can be generated from equation 3.17 as follows,

$$\phi'_{\mathrm{i}}(\mathrm{r}) = \hat{F}\phi_i(r) = \sum_\lambda f_\lambda d_{i\lambda}\psi_\lambda(r), \tag{3.19}$$

where

$$f_\lambda = f_{FD}(E_\lambda) \tag{3.20}$$

where $f_{FD}(E_\lambda$ is the Fermi Dirac function. By putting Eq. 3.18 into 3.19 we will obtain the final filtered function formula

$$\phi'_i(r) = \sum_k K_{ki}\phi_k(r) \tag{3.21}$$

as used previously (equation 3.2)

The most important feature of this procedure is that the filtered function ϕ'_i is *Localised* provided the FD function is at a high enough temperature. This means that it can be constructed from functions $\phi_i(r)$ that are nearby in space. In other words the sum in 3.2 is limited to including Gaussian functions ϕ_i which are centred on atoms close to 'i'. This means that the matrix K is sparse. In practice this may be done by including only those Gaussian whose centres are inside a cut-off radius (see figure 3.1).

This filtration radius or R_c is one of the most significant parameters, which the filtration functions depend upon, and has the main role of maintaining and increasing the accuracy of the filtration method. The effect of the filtration radius depends upon the shape of the filtered function and the filtration temperature (kT). This parameter

is chosen to reproduce a calculations using an established basis set (i.e.(*dddd* or *ddpp*) for Si). Typical values that give an acceptable accuracy, with keeping a sufficiently small radius are $R_c = 7$ or $R_c = 8$ a.u in diamond, or $R_c = 10$ or $R_c = 12$ a.u in silicon. The number of functions included can be further reduced (trimmed) using parameters referred to as `rad_trim` and `tol_trim`. These have the following meaning:

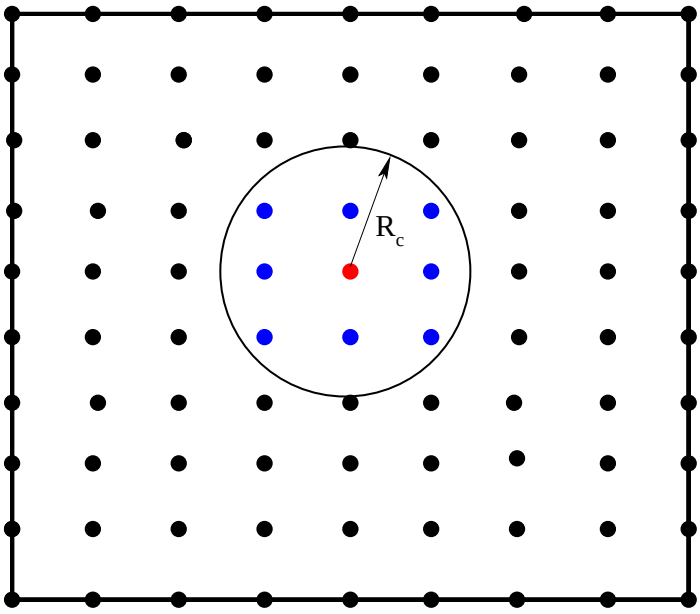

Figure 3.1: A schematic showing the subspace and the cutoff radius (R_c) which includes a limited number of atoms. The filtered basis functions are constructed only from Gaussians on these atoms.

Suppose a sphere of radius `rad_trim` is drawn around the atom in question (i.e. the one for which we are determining the filtered function). Primitive basis functions with centres outside this sphere (but still within the cut-off radius R_c) will only be included to build the filtered function if they have a value greater than exp[tol_trim] on the surface of the sphere. This greatly reduces (i.e. trims down) the number of primitive functions used. This significantly speeds up the filtration process, but has not been used in the work presented here.

3.4 The filtration Fermi temperature

The insertion of the occupancy f_λ in equation 3.3 introduces a chemical potential and a filtration temperature into the calculation. It is very important that we do not confuse the filtration temperature with the usual temperature which controls the occupancy of the KS states, just as in a conventional run. The filtration temperature is chosen to be high (e.g ∼2-3 eV in Si) for a few reasons. First and most importantly, it is the filtration temperature that makes the functions ϕ_i' exponentially localised in metals (without it, they would not have this essential property). Further a high temperature will increase the localisation of the functions, contributing to a small cutoff radius being possible. The temperature can be automatically optimised given the constraints of the imposed R_c values and the predefined number of filtration functions. The chemical potential introduced in the filtration step is given an initial approximate value and this too is then optimised as part of the self-consistency cycle.

3.5 Evaluation of the filtered forces

Forces in an *ab initio* calculation are found using the Hellmann-Feynmann theorem:

$$f_\beta = -\frac{\partial E}{\partial R_\beta} = -\sum_\lambda \langle \Psi_\lambda | \frac{\partial \hat{H}}{\partial R_\beta} | \Psi_\lambda \rangle \tag{3.22}$$

$$f_\beta = -\sum_{ij} b_{ij} \frac{\partial H_{ij}}{\partial R_\beta} \tag{3.23}$$

where the potential is the only part of the Hamiltonian that depends explicitly on atomic positions. When using localised atom centred basis sets, it is necessary to also differentiate the basis function with respect to the centre. This leads to an additional Pulay term

$$-f_\beta = \frac{\partial E}{\partial R_\beta} = \sum_{ij} \frac{\partial H_{ij}}{\partial R_\beta} b_{ij} - \sum_{ij} \frac{\partial S_{ij}}{\partial R_\beta} \omega_{ij} \tag{3.24}$$

$$\omega_{ij} = \sum_\lambda c_i^\lambda c_j^\lambda \varepsilon^\lambda f(\varepsilon_\lambda) \tag{3.25}$$

However, in a filtration calculation the matrix K will also depend on atomic position. This will lead to additional terms in the force but we have checked that these are

not significant for the cut-off radii used in this work, typically being smaller than the errors due to residual non-self consistency. Numerical demonstrations of this are given in [34]. Further evidence is given by the accuracy of optimised structures presented later in this work.

3.6 Filtration contrasted with contraction

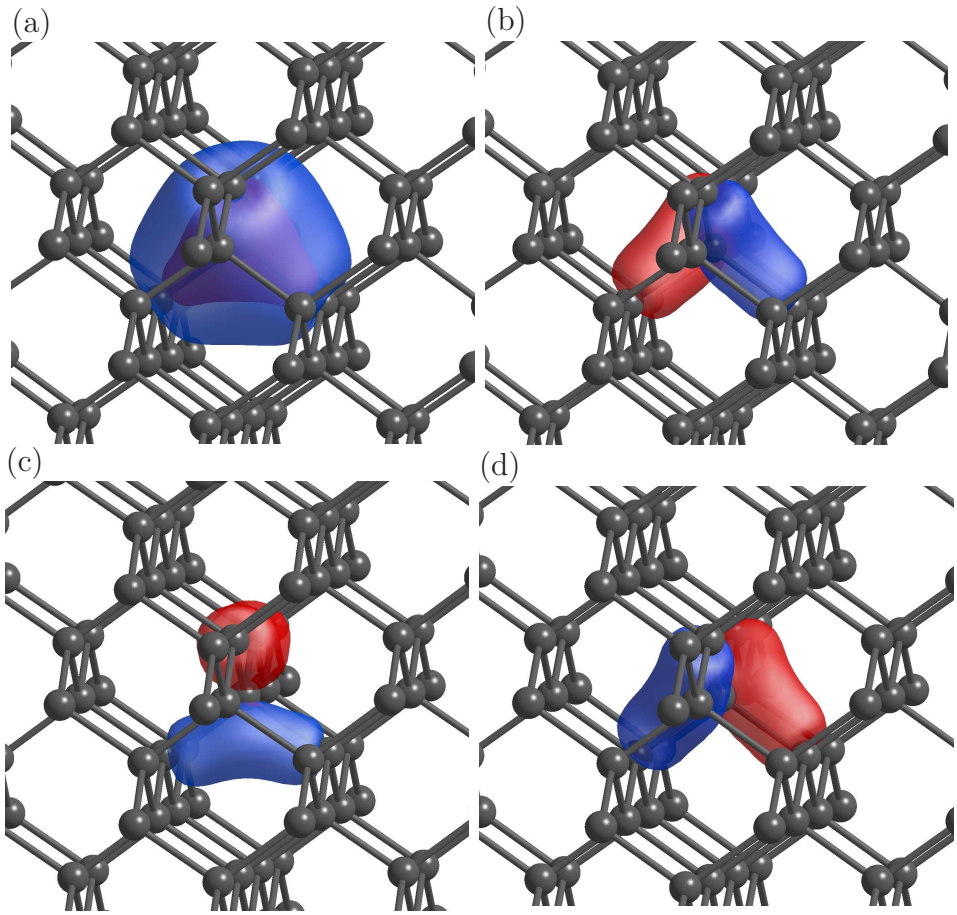

Figure 3.2: Filtered basis functions generated for a single atom in bulk diamond. The four functions have been projected from (a) S, (b) P_x (c) P_y, and (d) P_z Cartesian Gaussian functions. The red and blue surface are positive and negative iso-surfaces of the filtered functions.

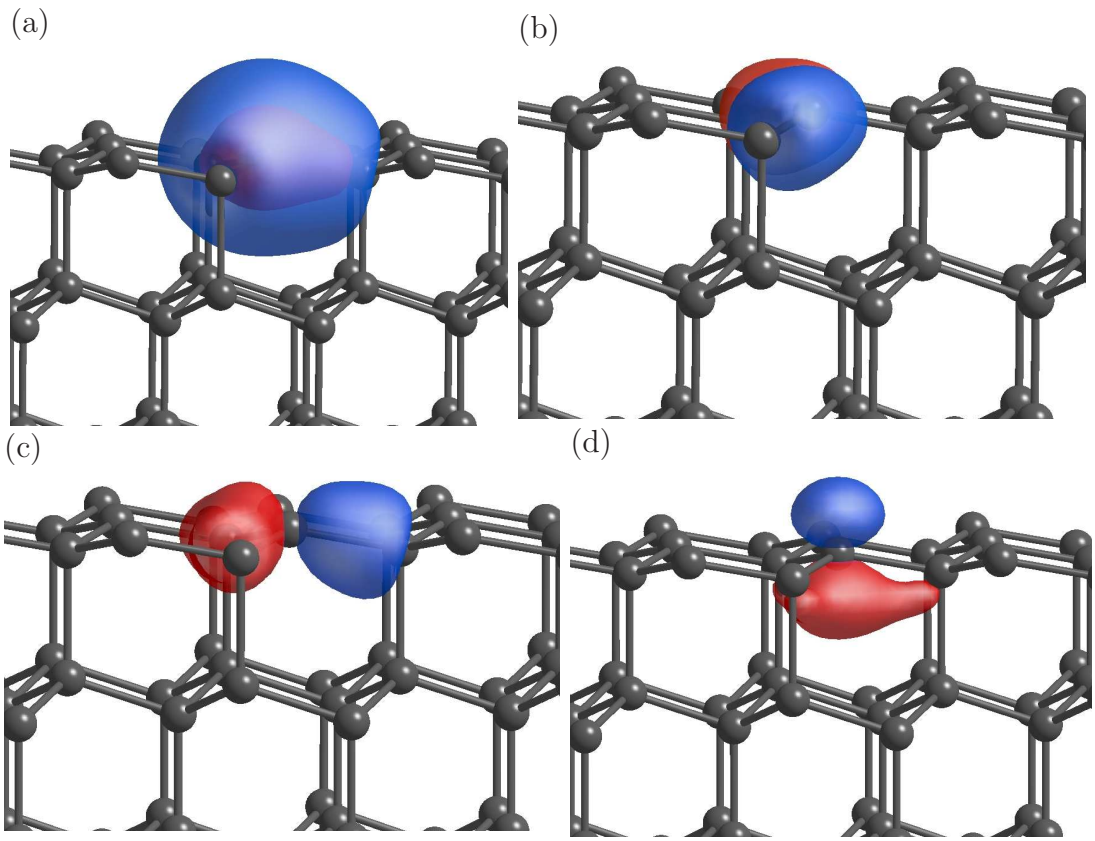

Figure 3.3: Filtered basis functions generated for a single atom at a (111) surface in diamond. The four functions have been projected from (a) S, (b) P_x (c)P_y, and (d)P_z. Cartesian Gaussian functions. The red and blue surface are iso-surfaces of the filtered functions.

The process indicated by equation 3.2, where a small number of basis functions are constructed from a much larger number of starting functions does have an apparent resemblance with that of basis set contraction, frequently used in quantum chemistry [63] and indeed also in previous `AIMPRO` calculations. The idea of contraction is usually that a reference system is defined (e.g. an atom or a solid [52] and that the matrix K_{iI} in 3.2 is optimised, for example to give the lowest energy for that system. In the standard quantum chemistry basis sets 6-311G* the valence shell of carbon is represented by 3 s-type functions, 9 p-type functions and 6 polarisation functions giving 18 functions in total. These are contracted from 26 functions, a modest im-

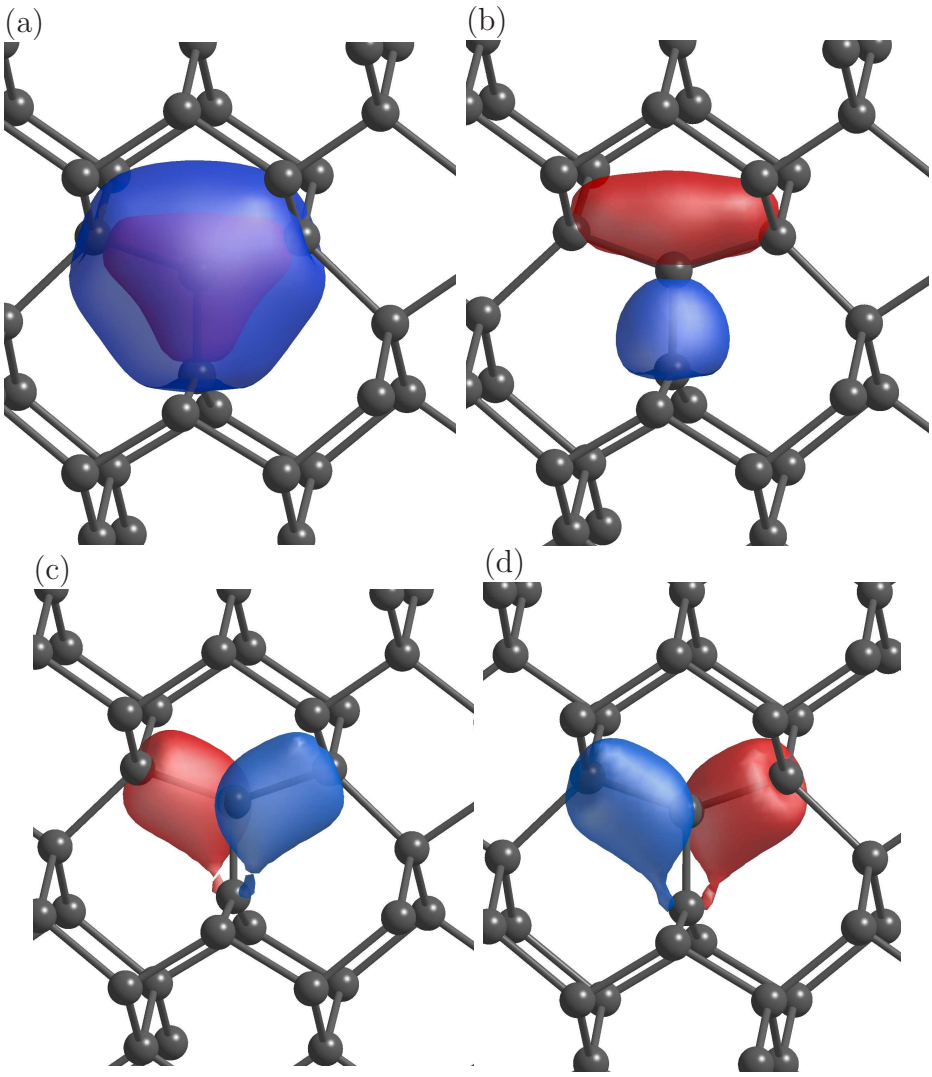

Figure 3.4: Filtered basis functions generated for a single atom in [100] interstitial in diamond. The four functions have been projected from (a) S, (b) P_x, (c)P_y, and (d)P_z. Cartesian Gaussian functions. The red and blue surface are iso-surfaces of the filtered functions.

provement. It is *assumed* that the contraction is transferable to other environments containing carbon (e.g. diamond, graphite, organic molecules) although this is less easily tested.

In contrast filtration is much more ambitious, it reduces the number of valence basis functions in the 6-311G* case from 26 to 4, does so in a controlled manner

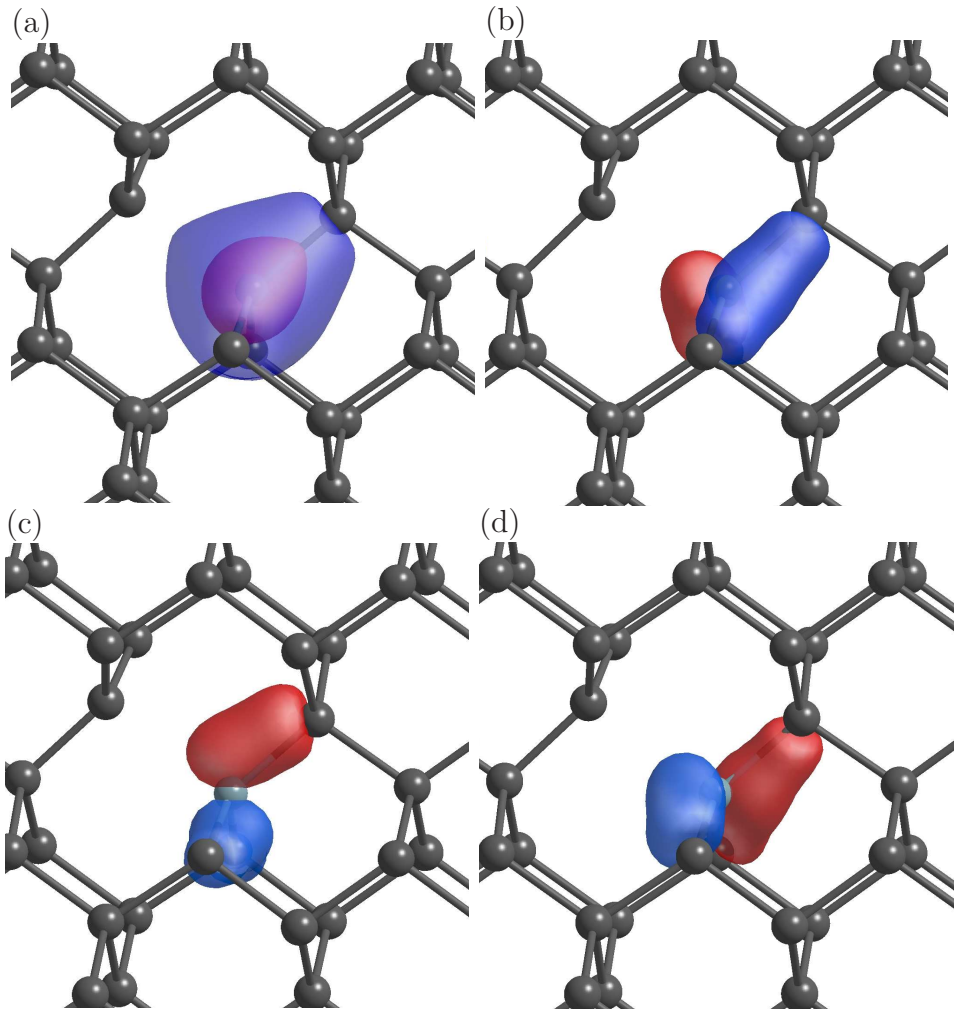

Figure 3.5: Filtered basis functions generated for a single atom in a P1 centre in diamond. The four functions have been projected from (a) S, (b) P_x (c)P_y, and (d)P_z. Cartesian Gaussian functions. The red and blue surface are iso-surfaces of the filtered functions.

and crucially does so for the system being modelled. This means that the reference system and the errors incurred through the transferability assumption are entirely absent from a filtration calculation. The filtered functions automatically adapt to the chemical environment and the electronic structure at that stage of the self consistency cycle.

As an illustration of this, Figure 3.2 shows the four filtered functions generated for

diamond - it is seen that these do have a symmetry resemblance to s and p functions (in so far as they respectively have no nodal plane and one nodal plane). More correctly they correspond to a_1 and t_2 symmetry adapted functions in the T_d point group. Figure 3.3 shows the corresponding filtered functions for an atom at the (111) surface of diamond. It is seen that this time there is a definite asymmetry between the functions projected from p-type Cartesian Gaussians, with the function aligned along [111] differing noticeably in shape from the other two functions in the plane. The a_1 symmetry function is also significantly distorted.

Figure 3.4 shows a similar result for the [100] split-interstitial defect structure in diamond (this will be considered at greater length in chapter 7). Here it is seen that there is a clear difference between the three functions projected from the p-type Cartesian Gaussians. The resulting function aligned along the [100] bond now has a clear asymmetry, unlike the other two. Figure 3.5 shows the four basis functions generated for the N atom in the P1 centre (to be considered in more detail in chapter 8). The functions again differ markedly from those in figure 3.2 again illustrating the fact that the functions adapt to the local environment.

3.7 Conclusion

This chapter has introduced the filtration technique with the idea that projected (Filtration) basis functions can be produced which accurately span the occupied subspace and which adapt to the chemical and structural environment automatically. The following chapter will explore the accuracy of this as applied to the semiconductors silicon and diamond.

Chapter 4

The calculation of observables in AIMPRO

Previous chapters have described the theory required to calculate the total energy of a system of atoms. In this chapter we will consider how additional properties may be calculated enabling further comparison with experimental measurements

4.1 Lattice constant and bulk modulus

The lattice constant for a cubic system or lattice parameters for other materials are fundamental properties, and were one of the very first properties to be calculated using density functional theory, more than 30 years ago [64]. The determination of lattice parameters for a lattice of general symmetry is somewhat complex, but is more straightforward for a cubic material. Theoretically, this parameter is found by optimising the positions of the atoms within the unit cell for a number of lattice constants a_0 and then attempting to find the a_0 value which produces the lowest energy. In practice, a set of 6-10 a_0 values are sampled which surround the approximate equilibrium value by $\pm 4\%$ and the resulting energies fitted to the Birch-Murnaghan equation [65]:

$$E(V) = E_0 + \frac{B_0 V}{B_0'}\left(\frac{(V_0/V)^{B_0'}}{B_0' - 1} + 1\right) - \frac{B_0 V_0}{B_0' - 1} \tag{4.1}$$

where E and V are the total energy and volume, E_0 is the equilibrium energy, V_0 is the equilibrium volume, B_0 is the bulk modulus, B_0' is the first derivative of the bulk

modulus (B) with respect the pressure, and is given by,

$$B_0' = \left.\frac{\partial B}{\partial P}\right|_T \tag{4.2}$$

These fitted parameters are then used as the determined values of a_0 and B_0. In local density functional calculations, a_0 is typically underestimated by about 1% with respect to experimental values, with a tendency to slightly over estimate bulk moduli. The GGA sometimes reverses this trend (slightly high lattice constants and low bulk moduli), although in both cases, agreement with experiment is generally quite acceptable. The purpose of the work in this thesis will be to assess the impact of filtration on these parameters.

4.2 The band structure

The band structure has a significant role in determining the electronic properties for any material. The band structures plotted in this work are the Kohn-Sham eigenvalues determined as a function of the wavevector k. The band gap may be estimated as the energy difference between the valance band maximum (VBM) and the conduction band minimum (CBM). This generally has a poor agreement with experiment, a well-known failing of DFT [66, 67]. The valence and some conduction bands of bulk diamond are shown in figure 4.1.

It is well-known that the band structures for diamond and silicon are indirect, where the VBM occurs at the Γ point and the CBM is near the X point. The experimental value for diamond is around 5.50 eV at room temperature [68]. The value of the direct band gap is around 7.1-7.3 eV at $(\Gamma - \Gamma)$ point [69–71]. The GGA and LDA calculated values for these are lower 5.59 eV and 5.64 eV respectively. This is a well known shortcoming of density functional theory, as mentioned above.

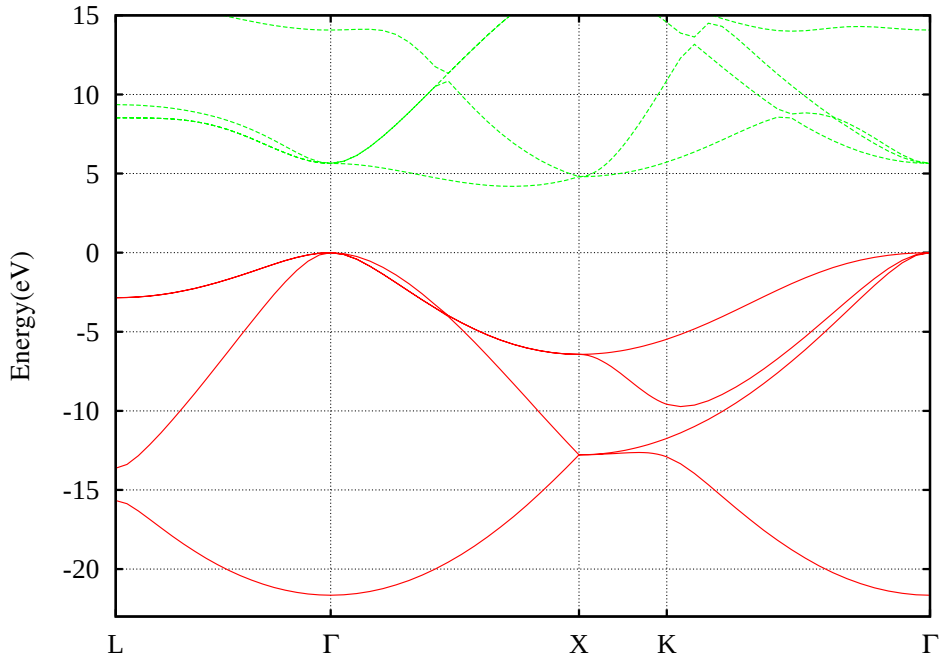

Figure 4.1: Calculated electronic band structure of bulk diamond, using a two atom unit cell. The red and green (Kohn-Sham) levels show the occupied and unoccupied bands, respectively.

4.3 The dynamical matrix and phonon frequencies

The local vibrational modes (LVM's) [72–79] associated with defects are one of the significant physical quantities observable experimentally. The vibrational frequencies are considerably affected by the atomic structure of the defect and hence are a sensitive tool to be used for characterisation.

For a molecule or cluster, if the displacement of atom i in direction α [α=1 means the x-direction; α=2 means the y-direction; etc] in mode λ is denoted by $u_{i\alpha}^{\lambda}$, and the frequency of vibration is ω_{λ}, then

$$\sum_{j\alpha} D_{i\alpha,j\alpha} u_{j\alpha}^{\lambda} = \omega_{\lambda}^{2} u_{i\alpha}^{\lambda} \tag{4.3}$$

where the dynamical matrix is,

$$D_{i\alpha,j\alpha} = \frac{1}{\sqrt{m_i m_j}} \frac{\partial^2 E}{\partial R_{i\alpha} \partial R_{j\beta}} \tag{4.4}$$

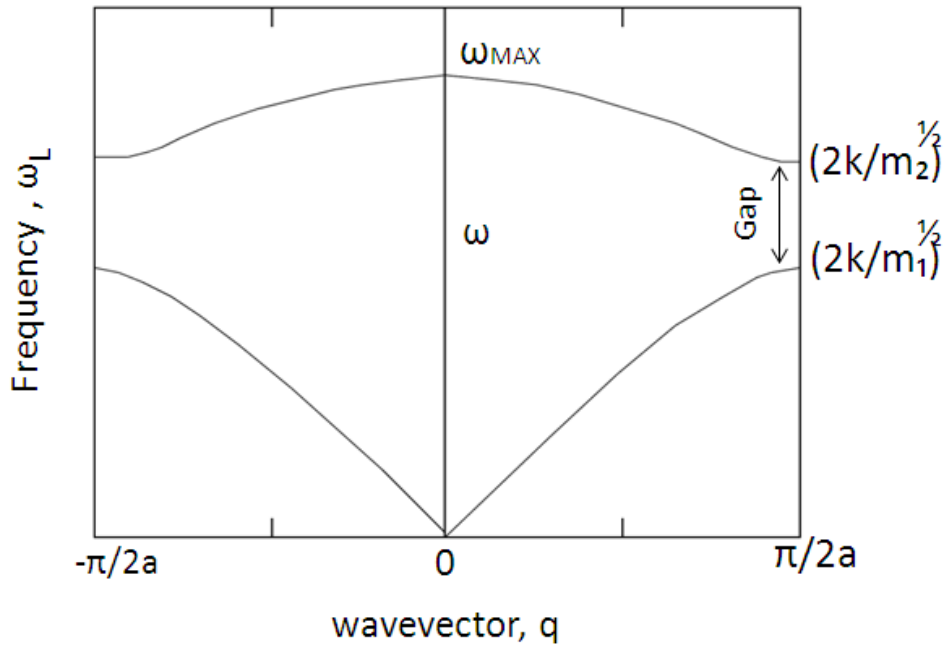

Figure 4.2: A schematic diagram showing the phonon dispersion for a diatomic linear chain of atoms of masses m_1 and m_2.

and $R_{i\alpha}$ and m_i are the position and mass of atom i. If this approach is used in a supercell the frequencies obtained are for the wave vectors q = 0 (i.e. the Γ point). Frequencies at other wave vectors can be obtained by using a larger unit cell (see discussion in chapter 5).

This technique enables us to predict peaks in infrared or Raman spectra in a defect due to the atomic vibrations. Simple models of a linear chain of atoms lead to spectra of the form shown in figure 4.2. It is clear that there is a maximum frequency at which the atoms can vibrate in a phonon mode. Above this, modes will be attenuated and this gives rise to the phenomena of localised vibrational modes: modes which are at a higher frequency that those in the host material but which are localised in the immediate vicinity of the defect. Localised modes can sometimes also occur in the gap between acoustic and optical modes.

In order to calculate the vibrational modes, the process begins from the self-consistent charge density, the atoms have to be relaxed until the forces on them are

converged. Then an atom i is displaced by an amount ε in the direction α and the self-consistent charge density and energy are recalculated. The forces on all atoms are then found. Suppose that the resulting force on atom j in direction β is then $f^+(i\alpha, j\beta)$. The process is repeated, this time moving atom i by $-\varepsilon$ in the α direction giving a force $f^-(i\alpha, j\beta)$. The dynamical matrix can then be calculated using the formula:

$$D_{i\alpha,j\beta} = \frac{f^+(i\alpha, j\beta) - f^-(i\alpha, j\beta)}{2\varepsilon} \tag{4.5}$$

The eigenvalues of the dynamic matrix are the squares of the vibration frequencies within the harmonic approximation [80] as shown in equation 4.3. Ideally the shift ε should be very small, but must be finite for numerical reasons. The implemented technique will therefore generate vibrational frequencies with some an harmonic terms, thus these modes are termed $quasi - harmonic$ [81].

4.4 The specific heat capacity

The specific heat capacity is one of the most significant experimental observable quantities in thermodynamics. The specific heat capacity is the amount of heat required to change the temperature of one kilogram of the substance one degree centigrade. Calculations of the specific heat of semiconductors depend essentially upon the phonons, not electrons. Indeed, the specific heat capacity and other thermodynamic properties can be easily determined if the $\Gamma -$ phonon vibrational frequencies for large supercell of perfect material are known. This is achieved by solving the dynamical matrix eigenvalue problem see equation 4.3 in section 4.3 from $ab - initio$ calculations using density functional theory (DFT).

According to statistical physics, the energy, U, of a harmonic oscillator of frequency ω in contact with a temperature reservoir (temperature T) is

$$U = \frac{1}{2}\hbar\omega + \frac{\hbar\omega}{\exp \hbar\omega/kT - 1}$$

The specific heat at constant volume may be derived as the temperature derivative of this. If instead of a single harmonic oscillator, we have a set of oscillators with frequencies ω_i, the formula is generalised to:

$$C_v = k_B \sum_i \left(\frac{\hbar\omega_i}{2k_BT}\right)^2 \left\{\frac{1}{\sinh^2(\frac{\hbar\omega_i}{2k_BT})}\right\} \tag{4.6}$$

Here k_B is the Boltzmann constant, ω_i is the phonon frequency, T is the temperature in the Kelvin scale, $\hbar$ is Planck's constant.

4.5 Electronic energy levels

The electrical level of a defect is represented by the electron chemical potential, when the relevant charged states have the same energy [82]. This can be found using the formation energy method, where the formation energies of neutral and charged defects are found. The supercell size for both states should be have the same size. The (0/+) and (-/0) levels represent the donor and acceptor levels relative to the valence band maximum (VBM) energy, respectively. The electrical level of a defect is represented by the electron chemical potential, when the relevant charged states have the same energy [52].

For a charged system, the formation energy will depend on the position of the electron chemical potential, for example,

$$E^f(X,q) = E(X,q) - \sum_i^{atoms} \mu_i + q(\mu + E_{VBM}) + \chi(X,q) \tag{4.7}$$

where μ_i is the chemical potential of atom i, μ is the electron chemical potential and $\chi(X,q)$ is a correction due to the approximate treatment of a charged defect in a finite sized unit cell. The formation energy is then plotted as a function of the electron chemical potential see fig 4.3. A plot allows estimating the electrical energy levels for the defect. The ionization energy for a couple of different charged states is the chemical potential at which the defect has the same formation energy in each charge state. The ionization energy has been computed relative to the valence band

maximum energy of the solid (VBM) which is given by this formulae, for example the donor level $\varepsilon(0/+)$ is the value of chemical potential, for which the neutral and positive charge states have the same formation energy,

$$\varepsilon(0/+) = E(X,0) - E(X,+) - E_{VBM} \tag{4.8}$$

where $E(X,q)$ are the total energies of the supercell with the defect in charge state q.

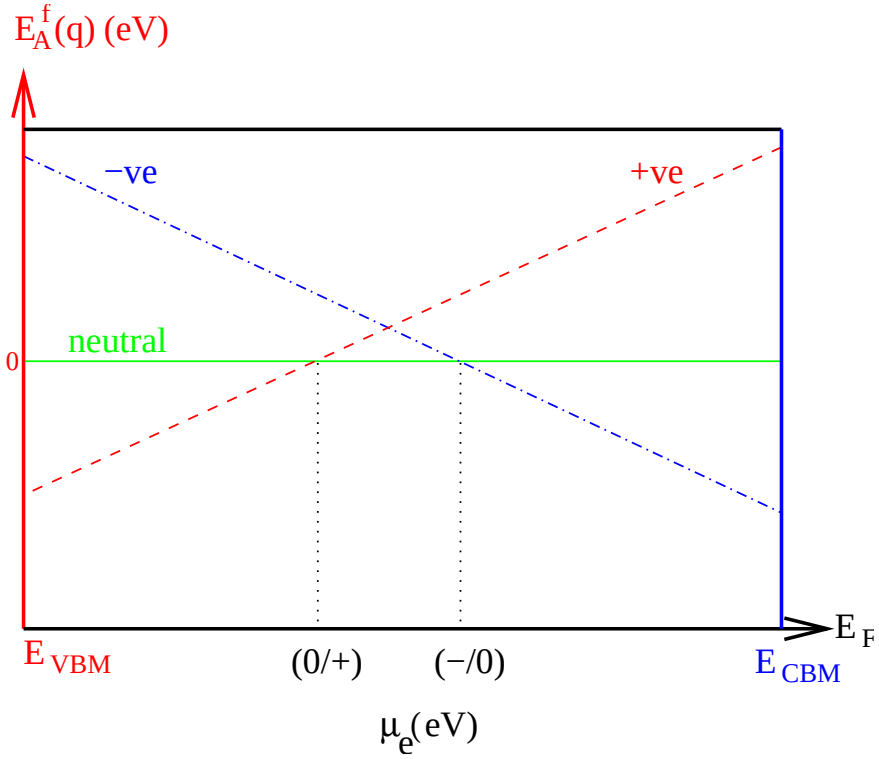

Figure 4.3: Schematic diagram showing the formation energy $E_A^f(q)$ for three charge states q of a structure A, as a function of the electron chemical potential μ_e. Rad and blue vertical lines represent the bulk valence and conduction boundaries, respectively. The donor level (0/+) is the Fermi energy above which the neutral charge state is lower in energy than the positive charge state, while the acceptor level (-/0) is the value of E_F above which the negative charge state is favoured over the neutral.

4.6 Marker method

The marker method [52] is a semi-empirical method to calculate the energy of an electronic level this method uses a well known experimental value of the acceptor or donor levels as a reference. A representation of the ionisation energy is found by estimating the difference between the energies of the neutral and charged structures, as shown in the following equation,

$$(0/+)_X = (0/+)_Y + \{[E(X^0) - E(X^+)] - [E(Y^0) - E(Y^+)]\} \tag{4.9}$$

where $(0/+)_X$ is the donor level of the system under study, $(0/+)_X$ is the donor level potential of the reference defect, $E(X^0)$ and $E(X^+)$ are the total energies of the system $X(0,+)$ in the neutral and charge states, $E(Y^0)$ and $E(Y^+)$ are the total energies of the reference system $Y(0,+)$ in the neutral and charge states. Cancellation of the errors in the two calculated values is the important feature of this method, and this enables more accurate defect levels to be found.

4.7 Binding energy

The binding energy is important in practice as it gives information about the temperature at which a defect complex will dissociate. The concept of the binding energy arises when a complex defect is formed, by the assembly of two or more primary defects α, β. A definition of the binding energy of the substance is the amount of the energy released when one defect complex is formed [83]. The binding energy can be computed as the difference in formation energies of the complex $\alpha\beta$ and the individual defects α, β is and given by

$$E^b(\alpha\beta) = \{E^f(\alpha) + E^f(\beta)\} - E^f(\alpha\beta) \tag{4.10}$$

From this equation, a positive value of the binding energy $E^b(\alpha, \beta)$ represents a bound complex.

4.8 Hyperfine parameters

Electron paramagnetic resonance (EPR) [84–87] is one of the major spectroscopes used to probe properties of defects in semiconductors. In its simplest form, a defect with an unpaired electron will have spin $S = \frac{1}{2}$ and there will be two quantum states (up and down) associated with this. These have different energies in a magnetic field and the energy difference can be determined by finding the frequency of electromagnetic radiation which is resonantly absorbed. A study of this frequency as a function of the direction of the magnetic field leads to information about the symmetry of a defect.

In practice the situation may be more complicated if nuclei which also have a magnetic moment are present. In this case more than one absorption peak may be seen (figure 4.4)

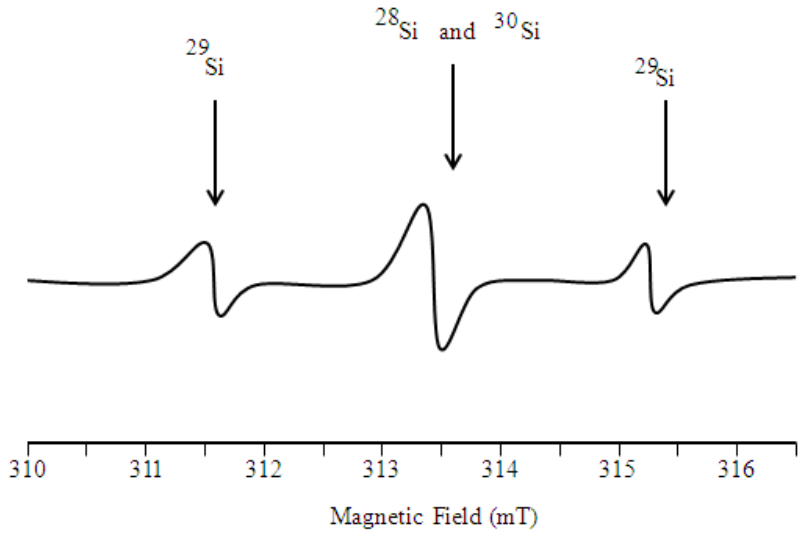

Figure 4.4: Schematic of EPR spectra for an unpaired electron $S = \frac{1}{2}$ interacting with nuclear spin $I = \frac{1}{2}$.

The hyperfine interaction arises from the interaction between a nuclear spin and an electron spin. It is therefore seen in defects which include an atom with a non-zero nuclear spin (for example, the ^{14}N nucleus has a spin $I = 1$; the ^{13}C nucleus has a spin $I = \frac{1}{2}$) and also which have a non-zero electron spin (for example, a defect with an

unpaired electron). It is important that the calculation of hyperfine interactions uses a true wavefunction, not a pseudopotential wavefunction, as the effect is dominated by the spin-density in the vicinity of the nucleus. This creates a problem for many *abinitio* calculations which are performed with a pseudopotential. However, a procedure exists to reconstruct an all-electron wavefunction from the pseudo-wavefunction [47, 88]. This is used in the work in this thesis.

The hyperfine structure is generally described by a 3×3 matrix, and usually the principal values (eigenvalues) of this are reported. In the special case of an axially symmetric defect (e.g. symmetry C_{3v}) two of these values are equal. One eigenvector of the tensor lies along the axis of the defect (the associated eigenvalue is $A_{\parallel}$) and two are perpendicular to this (with the two equal values $A_{\perp}$). These are sometimes also reported in terms of A_s which depends on the unpaired electron density at a nucleus (originating from s-states) and a term A_p which, in most defects in diamond, originates from p electrons. The parameters are related by,

$$A_s = \frac{(A_{\parallel} + 2A_{\perp})}{3} \tag{4.11}$$

$$A_p = \frac{(A_{\parallel} - A_{\perp})}{3} \tag{4.12}$$

A comparison between calculated and measured hyperfine spectra can be very powerful, as information obtained from the experiment is very detailed. It is chemically specific (i.e. an absorption will relate to an individual nucleus in a defect) and structurally sensitive (there is information about the symmetry of the defect as seen on each nuclear site that has a magnetic moment). It has been a key probe used to characterise defect centres in diamond, and will be further discussed in chapter 8.

4.9 Modelling surfaces

Studies of the surfaces of semiconductors such as diamond and silicon have attracted interest from many researchers [89–92], due to various reconstructions of the surfaces

which have interesting properties [93–97]. A surface is simulated within the supercell method by constructing a so-called slab system, by repeating the supercell in one of the lattice vectors, this will generate an extra supercell volume which is emptied of atoms, therefore this will create a vacuum region between the substance and their repeated images in one direction. The vacuum thickness between slabs has to be adequate to reduce the interaction between atoms which are on the lower and upper surface of slabs [98], but increasing the vacuum thickness will need a larger number of plane waves, which will be require a large memory in the computer and spending much time to model [2, 99].

4.9.1 Absolute surface energy

The absolute surface energy ($E_{surf}^{n\times m}$) of the $n \times m$ reconstructed surface of a substance is the difference between the total energy (E_{tot}) of the system and its energy, when in a reference state. The amount of energy required to create one unit cell of new surface of substance is called the surface energy [83], and is given by the expression,

$$E_{surf}^{n\times m} = \frac{1}{2}(E_{tot} - \sum_i \mu_i N) \tag{4.13}$$

Here the μ_i are the chemical potentials of the atoms present, and the pre-factor $\frac{1}{2}$ is present as centrosymmetric slabs have two equivalent surfaces, which are introduced into the calculations. The $(n \times m)$ reconstructions indicates to the number of 1×1 unit cells in the primitive $(n \times m)$ case, this number must be divided by a factor 2 in the centered structure case $(n \times m)$. A fuller discussion of the surfaces studied is given in chapter 6.

4.10 Electron affinity

The electron affinity (EA) is the difference between the energy of the vacuum level E_{VAC}, (the energy above which electrons do not need extra energy to leave the material

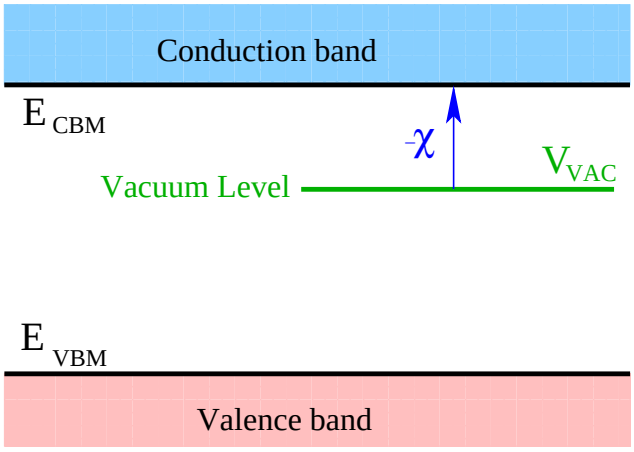

Figure 4.5: The scheme shows the energy level for semiconductor materials with negative electron affinity.

surface freely), and the conduction band minimum (E_{CBM}).

$$\chi = -(E_{CBM} - E_{VAC}) \tag{4.14}$$

The values of the electron affinity can be negative or positive [100]. A negative value comes when the vacuum level is lower in energy than the conduction band minimum, this makes the substance an efficient photo-emitter, as in hydrogenated C(100) and (111) surfaces [101, 102]. This means that the electrons in the conduction band close to the surface will move from the sample to the vacuum level, due to the vacuum level being lower than the conduction band minimum, as shown in figure 4.5. It is much more common for the EA to be positive in which case electrons in the conduction band can not readily escape from the material.

4.11 Conclusion

Many experimental quantities can be determined computationally, using the `AIMPRO` package, enabling many scientific analyses and predictions to be made. The application part of the thesis looks at a sequence of materials problems, and will calculate the observable quantities described in this chapter in order to assess the accuracy and reliability of the filtered basis set.

Part II

Application

Chapter 5

The Accuracy of Filtration applied to Diamond and Silicon

5.1 Introduction

The AIMPRO code has a long and successful track record in examining electronic systems [13, 18]. The method used to obtain the results presented in this thesis includes the recent development called the filtration method. The main goal achieved in the development of this method is a reduction of running time, while keeping the accuracy of calculations largely unaffected, and this work will check the effect of implementation of the filtration on the basic Figure 5.1 shows the conventional unit cell of diamond and silicon.

In order to test the accuracy of any set of basis functions, the first and most common physical quantities that must be investigated are the lattice parameter and bulk modulus. The accuracy of an improved modelling technique is first estimated by computing the values of these parameters. The electronic band structure is another fundamental physical quantity which underpins a study of the electronic and optical properties of solids. Therefore in this chapter it is calculated and compared with previous calculated and experimental values. As indicated in section 4.3, the vibrational modes are calculated by diagonalisation of the dynamic matrix, to test

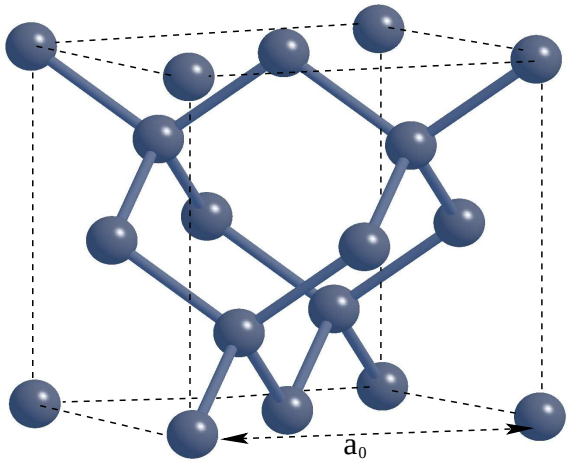

Figure 5.1: Conventional unit cell of diamond, where a_0 is the lattice constant.

the accuracy of the filtration method on some optical properties, such as Raman and Infrared spectra. The effect of the application of filtration upon these key physical parameters is presented for bulk diamond and silicon.

5.2 Computational method

Our calculations have been carried out using the density functional method, by using filtered and unfiltered techniques, which are implemented in the `AIMPRO` software [16, 33, 103, 104], as described in chapters 2 and 3. The calculations of the lattice parameter and bulk modulus for diamond and silicon were performed in a face centred cubic (fcc) unit cell containing 2-atoms. The charge density is expanded in plane waves with an energy cutoff of 350 Ry, yielding well-converged total energies. Optimization of the structure, using computed forces, was always included. LDA [45] and GGA [105] functionals have been used to address the exchange-correlation term. The lattice constant values which have been computed by the (*dddd*) basis set which provides 40 Gaussian functions for each carbon and silicon atom is compared with the calculations which have been achieved using the filtration technique, that uses only 4 combinations of Gaussian functions. The success of the filtration technique relies on there being only a small number of basis functions. Sampling of the Brillouin zone is achieved using a Monkhorst-Pack (MP) grid of $4 \times 4 \times 4$ [60] special k-points. The pseudopotentials of

Hartwigsen, Goedecker and Hutter [51] are used, for elimination of core electrons [51]. Most comparison of our results are made with a standard reference calculation, and have been achieved with the same primitive basis set. All results by the filtration method have been computed for different cutoff radii(R_c), (for more details see section 3.3 in chapter 3.1), which are between 6-10 a.u. in diamond and 8-12 a.u. in silicon, and is unlimited for the traditional `AIMPRO` method. The temperature (kT) associated with the solution of the KS states in all results of the filtration and conventional calculations was 0.01 eV, although this does not affect the results in any way. The electronic band structure has been calculated using a unit cell of two carbon atoms in diamond and silicon. The lattice constants obtained with LDA and GGA functionals are 6.68 a.u (3.53 Å) and 6.76 a.u (3.57 Å) in diamond, and in silicon are 10.17 a.u (5.38 Å) and 10.39 a.u (5.49 Å) respectively.

We calculated the phonon frequencies by diagonalizing the dynamical matrix, which basically depends upon the second derivatives of the energy and atomic masses. In section 5.5.1, we shall present more details of the modelling of the simulation technique. In this chapter all results obtained by the filtration method are compared to the standard results, which are in good agreement with the measured experimental values.

5.3 Computational results

5.3.1 Lattice parameter and bulk modulus

Diamond

In this section, calculations of lattice constants and bulk modulus are made using the filtration method and are compared with unfiltered (traditional) calculations and with experiment.

It should be noted (see table 5.1) that the lattice constants calculated using the LDA and GGA differ from the experimental value by 1.1% and 0.06% respectively in

Table 5.1: Optimised lattice constants a_0 (in Å) and bulk modulus B_0 (in GPa) calculated using the LDA and GGA in diamond, (R_c in a.u).

Parameters	R_c	LDA	GGA
a_0	6	3.53418	3.57581
	7	3.53386	3.57567
	8	3.53194	3.57338
	9	3.53162	3.57303
	10	3.53120	3.57256
	∞	3.53079	3.57215
Exp		3.57 [106]	
B_0	6	458.7	437.5
	7	463.2	436.8
	8	463.1	431.1
	9	463.5	431.2
	10	463.7	431.2
	∞	463.6	431.4
Exp		443 [106]	

diamond. The differences in bulk modulus are 4.6% and 2.62%. Any comparison of the accuracy achieved by filtration should be made in the light of this underpinning uncertainty related to the approximations that are made in the LDA and GGA; our use of pseudopotentials and the underlying basis set of 40 functions per atom. It is seen from table 5.1 that even with a cut-off radius (R_c) of 6 a.u the error in lattice constant is 0.09% in the LDA and 0.1% in the GGA, much smaller than the error of 1.1% mentioned above as intrinsic to a conventional DFT calculation. Use of larger cut-off radii give far more accurate results with the R_c=10 a.u having reduced the error to 0.01% in the LDA and 0.015% in the GGA.

A similar pattern emerges on studying the behaviour of bulk modulus. Table 5.1

shows that even with a cut-off radius (R_c) of 6 a.u the error in bulk modulus is 1% in the LDA and 1.4% in the GGA, much smaller than the error of 2.62% mentioned above as intrinsic to a conventional DFT calculation using these functionals. Use of larger cut-off radius (R_c) gives far more accurate results, with the R_c=10 a.u. having reduced the error to 0.02% in the LDA and 0.05% in the GGA.

In conclusion it may be seen that the errors associated with reducing the number of independent basis functions from 40 to 4 are much smaller than those which are intrinsic to a standard DFT calculation and with R_c=8 a.u. are appropriate for standard modelling as used later in this thesis.

Silicon

In this section, calculations of lattice constants and bulk modulus of silicon are made using the filtration method and are compared with unfiltered (traditional) calculations and to experiment. It should be noted (see table 5.2) that the lattice constants calculated using the LDA and GGA differ from the experimental value by 0.8% and 1.2% respectively in silicon. The differences in bulk modulii are 3% and 13.5%. Any comparison of the accuracy achieved by filtration should be made in the light of this underpinning uncertainty related to the approximations that are made in the LDA and GGA; our use of pseudopotentials and the underlying basis set of 40 functions per atom. It is seen from table that even with a cut-off radius(R_c) of 8 a.u the error in lattice constant is 0.34% in the LDA and 0.03% in the GGA, much smaller than the error of 0.8% mentioned above as intrinsic to a conventional DFT calculation. Use of larger cut-off radius (R_c) give far more accurate results with the R_c=12 a.u having reduced the error to 0.06% in the LDA and 0.12% in the GGA.

A similar pattern emerges on studying the behaviour of bulk modulus. Table 5.2 shows that even with a cut-off radius of 8 a.u the error in bulk modulus is 0.52% in the LDA and 0.23% in the GGA, much smaller than the error of 3% mentioned above as intrinsic to a conventional DFT calculation. Use of larger cut-off radius gives far more accurate results with the R_c=12 a.u having reduced the error to 0.21% in the

Table 5.2: Optimised lattice constants a_0 (in Å) and bulk modulus (B_0 in GPa) calculated using the LDA and GGA in silicon, (R_c in a.u.).

Parameters	R_c	LDA	GGA
a_0	8	5.40091	5.49996
	9	5.38711	5.49884
	10	5.38711	5.49884
	11	5.38693	5.49882
	12	5.38560	5.49898
	∞	5.38235	5.49834
Exp		5.43 [106]	
B_0	8	95.6	85.4
	9	96.1	84.6
	10	96.1	84.6
	11	94.9	84.6
	12	95.9	85.6
	∞	96.1	85.6
Exp		99 [106]	

LDA and 0.00% in the GGA.

We now make a brief study of the localisation of the filtration basis functions in silicon. From figure 5.2, we can see that the effect of the temperature on the basis set, where the filtered basis sets become more localised by increasing the temperature. The figure 5.3 shows that increasing the temperature gives a greater percentage of the filtered basis function inside a sphere of radius (r) within allowed cut-off radius R_c, for each type of the atomic structure. This gives a different validation for the use of a finite cut-off and illustrates the fact that $R_c = 10$ a.u. is sufficient.

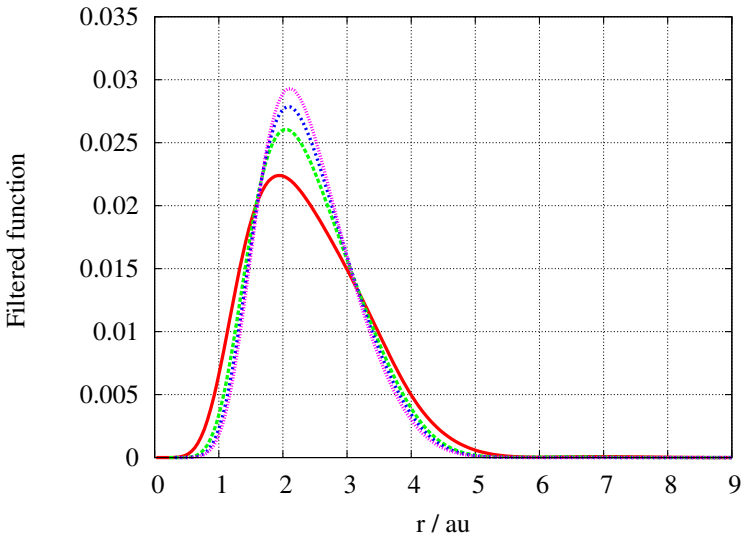

Figure 5.2: The figure shows the change in a shape of a spherically averaged filtered function as the filtration temperature is varied. The red, green, blue and pink colours have respectively, kT=0.1 Ha, 0.2 Ha, 0.3 Ha, and 0.4 Ha.

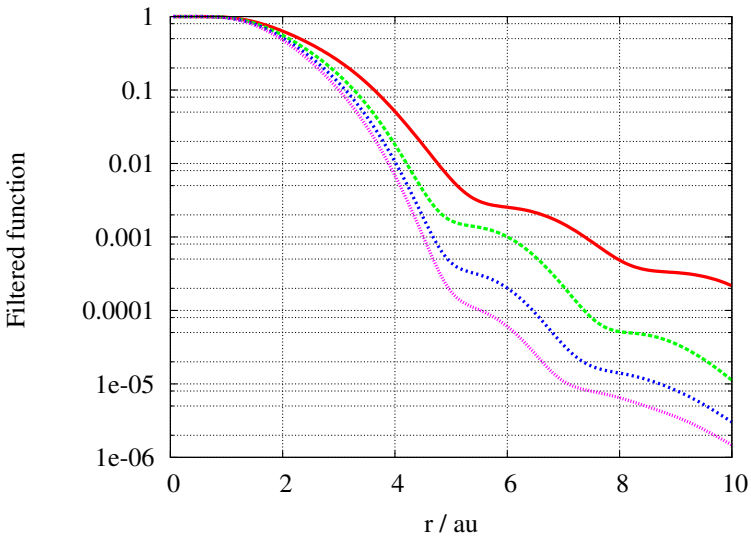

Figure 5.3: The fraction of the normalisation integral of a filtered function, $\psi_{filt}(r)$, lying outside a radius (r). This again illustrates the greater localisation obtained at higher filtration temperature. The curves are coloured as in figure 5.2.

5.3.2 Comparison with CASTEP/ONETEP

As explained in section 1.3.2, the ONETEP code also operates by producing four basis functions per atom, this time derived from an underlying PSINC basis [1]. In this brief section we compare our results obtained for 8 atoms of silicon modelled with the filtration method with published data from ONETEP calculations.

First we look at the change in total energy produced by the reduction from primitive to filtered basis. Figure 6 in Ref [1] shows that the total energy changes by 1–2 eV as a result of restriction to 4 basis functions per atom. In contrast, in our work table 5.3 shows that the corresponding variation is less that 0.1 eV, and is just 10 meV/atom for a cutoff of 8 au. This shows the accuracy of our filtration step.

Table 5.3: Difference between energies of eight silicon atoms for unfiltered and filtered calculations for LDA functional, and for three cut-of radii, R_c.

R_c (a.u)	8	10	12
Energy difference (eV)	0.088	0.086	0.044

Furthermore, Ref [1] contains data for the calculated lattice constant and bulk modulus for silicon. The data is reproduced in table 5.4 together with data from filtered runs. It is seen that in ONETEP, the lattice constant changes by 0.038Å and the bulk modulus by 3.9 GPa In comparison, changes in the filtration step are an order of magnitude smaller.

As a final point it is seen that unfiltered AIMPRO and CASTEP are in exceptionally close agreement, both with regard to lattice constant (the difference is only 0.001Å) and bulk modulus (the difference is only 0.2 GPa).

In conclusion it can be seen that the lattice constant and bulk modulus are reproduced accurately in the filtration calculation, and that the changes introduced are much smaller than is the case in alternative methodologies.

Table 5.4: Lattice constant and bulk modulus data for bulk silicon calculated by CASTEP/ONETEP (taken from [1]), filtered AIMPRO with three cut-off radii, (R_c in a.u) and finally unfiltered AIMPRO ($R_c = \infty$).

Calculation	CASTEP	ONETEP	$R_c = 8$	$R_c = 10$	$R_c = 12$	$R_c = \infty$
a_0 (Å)	5.383	5.421	5.400	5.387	5.385	5.382
B_0 (GPa)	95.9	99.5	95.6	96.1	95.9	96.1

5.4 Band structure

Turning now to a second test of the accuracy of filtration, we consider the band structures for bulk diamond and silicon using two-atom (fcc) unit cells. The accuracy of filtration on this quantity has not been evaluated previously with only properties dependent on total energy being presented. The band structures of bulk diamond and silicon are given along high-symmetry directions throughout these results. We can compare the width of the energy gap throughout the graphs in the figure 5.4, we note that there is no significant changing in the valence band levels positions, and in the conduction band level sites, the values of the band structures are calculated at three k-points (Γ, X and L) are shown in the tables 5.5, 5.6, another comparison for the band structures on the accuracy of the filtration technique are presented in figure 5.5.

Diamond

To assess the accuracy of the filtration method efficiency, we present in this section the calculations of the band structure in diamond using the LDA and GGA functionals. As shown in figure 5.4, there is a good visual agreement between the band structures calculated with and without filtration, especially in the valence band and at the bottom of the conduction band. Clearly, the fact that we only have four filtered

Table 5.5: Band structure energies in eV at three k-points L, Γ and X in diamond, using the LDA functional, as a function of R_c (in a.u.).

k-points	$R_c = 6$	$R_c = 7$	$R_c = 8$	$R_c = 9$	$R_c = 10$	$R_c = \infty$
$\Gamma_{25'}$	0.00	0.00	0.00	0.00	0.00	0.00
Γ_1	-21.63	-21.63	-21.64	-21.64	-21.65	-21.65
$L_{3'}$	-2.84	-2.84	-2.85	-2.85	-2.85	-2.85
L_1	-13.60	-13.60	-13.61	-13.61	-13.61	-13.62
$L_{2'}$	-15.65	-15.65	-15.66	-15.66	-15.66	-15.66
X_4	-6.41	-6.42	-6.42	-6.42	-6.42	-6.43
X_1	-12.76	-12.76	-12.77	-12.77	-12.77	-12.78

Table 5.6: Band structure energies in eV at three k-points L, Γ and X in diamond, using the GGA functional, as a function of R_c (in a.u).

k-points	$R_c = 6$	$R_c = 7$	$R_c = 8$	$R_c = 9$	$R_c = 10$	$R_c = \infty$
$\Gamma_{25'}$	0.00	0.00	0.00	0.00	0.00	0.00
Γ_1	-21.31	-21.32	-21.33	-21.33	-2133	-21.33
$L_{3'}$	-2.76	-2.77	-2.77	-2.77	-2.77	-2.77
L_1	-13.23	-13.24	-13.24	-13.24	-13.25	-13.25
$L_{2'}$	-15.60	-15.60	-15.60	-15.60	-15.61	-15.61
X_4	-6.21	-6.22	-6.22	-6.22	-6.22	-6.23
X_1	-12.66	-12.67	-12.67	-12.67	-12.67	-12.68

Table 5.7: Mean average differences between energies of band structure for unfiltered and filtered calculations the two atom (fcc) cell of diamond at three k-points L, Γ, and X for the LDA and GGA functionals, and for five choices of R_c.

R_c (a.u)	6	7	8	9	10
Mean differences (LDA)	0.013	0.013	0.005	0.005	0.002
Mean differences (GGA)	0.014	0.008	0.003	0.003	0.002

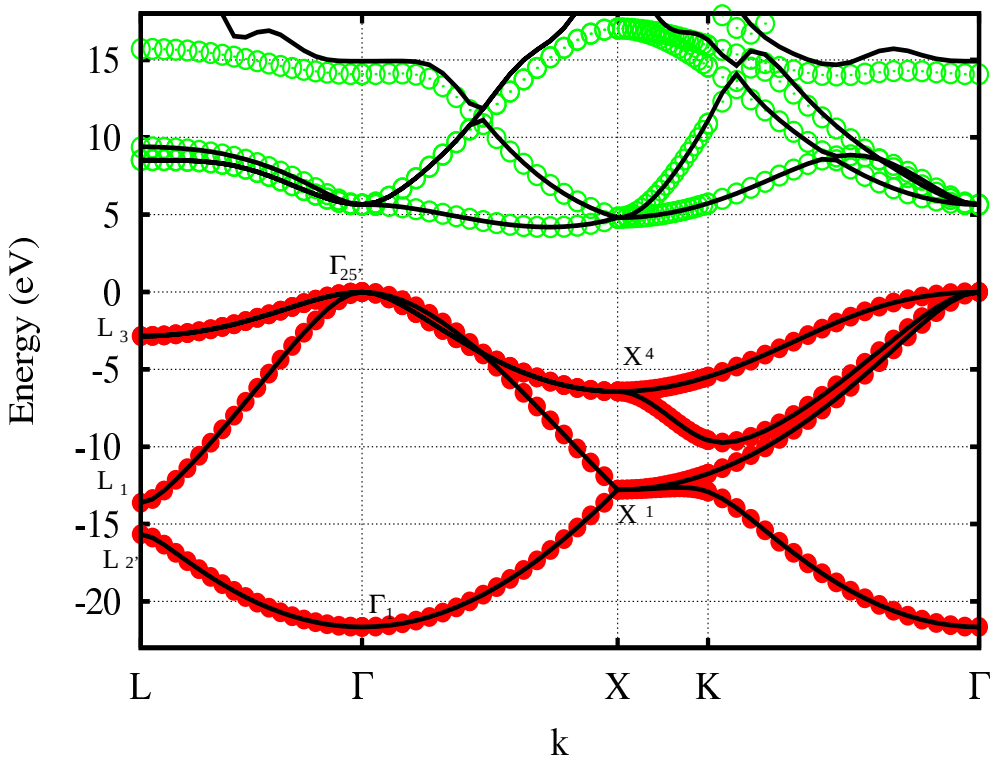

Figure 5.4: Schematic electronic band structure of bulk diamond, using a two atom unit cell, R_c=∞ and R_c=10 a.u, using the LDA functional. The red and green circles (Kohn-Sham) levels show the occupied and unoccupied unfiltered bands, and the black lines (Kohn-Sham) levels show the occupied and unoccupied filtered bands, respectively.

basis functions per atom (i.e. only 8 functions in total) will only enable 8 bands to be found and the higher bands will become unreliable - it is seen here at the conduction states agree reasonably well for several electron volts into the conduction band. A quantitative comparison is given in tables 5.5 and 5.6 and a summary in table 5.7. It is seen that mean differences are in the range 1–10 meV for cutoff radii which would be employed in practice (e.g. 8 a.u), and of the order 1 meV for a cutoff radius R_c of 10 a.u.

Silicon

In order to assess the accuracy of the filtered basis functions, the calculations of the band structure were performed for silicon using the LDA and GGA functionals. Figure 5.5 presents the results obtained by using filtered and unfiltered basis sets have shown that the edges of the valence and conduction bands at all k-points are extremely close together, and checking the higher levels in the conduction band, we can see that again the filtered and unfiltered energy levels begin to diverge, once again due to that the filtration technique does not taking those higher energies in its the construction of the filtered basis as we mentioned in the filtration methodology in chapter 3. The results for occupied bands and low-lying conduction states gives strong evidence that the improved simulation technique, which is suggested through this thesis gives good results. Quantitative comparisons are given in tables 5.8 and 5.9. The mean absolute differences between the energies of filtered and unfiltered band structures of silicon vary between around 0.001–0.013 eV and between around 0.0007–0.004 eV using the LDA and GGA functionals respectively, as R_c is varied (see table 5.10. For silicon, a typical calculation could use R_c= 10 a.u showing that the errors in the band structures are only $\sim$ 1 meV. Finally, our calculations indicate that the modified basis functions have given excellent findings, in comparison with the conventional Gaussian basis functions results, showing that the LDA and GGA results of the Kohn Sham levels are substantially the same. Although, the GGA values are slightly better than the LDA, both calculations give the same positive findings. These findings enhance our

Table 5.8: Band structure energies in eV at three k-points L ,Γ, and X in silicon, LDA functional as a function of R_c (in a.u).

k-points	$R_c = 9$	$R_c = 10$	$R_c = 11$	$R_c = 12$	$R_c = \infty$
$\Gamma_{25'}$	0.00	0.00	0.00	0.00	0.00
Γ_1	-12.14	-12.14	-12.13	-12.13	-12.13
$L_{3'}$	-1.20	-1.20	-1.21	-1.20	-1.21
L_1	-7.10	-7.10	-7.10	-7.10	-7.10
$L_{2'}$	-9.73	-9.73	-9.73	-9.73	-9.73
X_4	-2.90	-2.90	-2.90	-2.90	-2.90
X_1	-7.90	-7.90	-7.90	-7.90	-7.90

confidence in the application of the filtration technique.

Table 5.9: Band structure energies in eV at three k-points L ,Γ, and X in silicon, GGA functional as a function of R_c (in a.u).

k-points	$R_c = 9$	$R_c = 10$	$R_c = 11$	$R_c = 12$	$R_c = \infty$
$\Gamma_{25'}$	0.00	0.00	0.00	0.00	0.00
Γ_1	-11.82	-11.84	-11.84	-11.84	-11.84
$L_{3'}$	-1.22	-1.22	-1.22	-1.22	-1.22
L_1	-6.95	-6.95	-6.95	-6.95	-6.95
$L_{2'}$	-9.57	-9.57	-9.57	-9.57	-9.57
X_4	-2.85	-2.85	-2.85	-2.86	-2.86
X_1	-7.80	-7.80	-7.80	-7.80	-7.80

Table 5.10: Mean differences between energies of band structure for unfiltered and filtered calculations the two atoms at three k-points L,Γ, and X in silicon for LDA and GGA functionals, and for five values of R_c .

R_c (a.u)	6	7	8	9	10
Mean differences (LDA)	0.013	0.003	0.003	0.001	0.003
Mean differences (GGA)	0.004	0.003	0.003	0.0007	0.0007

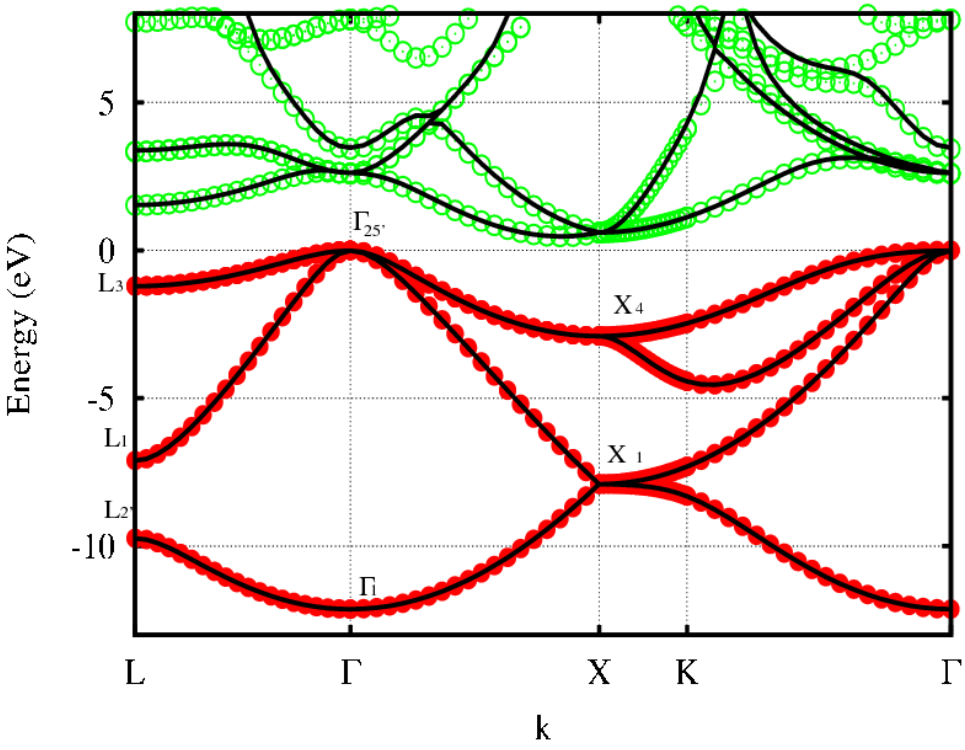

Figure 5.5: Schematic electronic band structure of bulk silicon, using a two atom unit cell, R_c=∞ and R_c=10 a.u, LDA functional. The red and green circles (Kohn-Sham) levels show the occupied and unoccupied unfiltered bands, and the black lines (Kohn-Sham) levels show the occupied and unoccupied filtered bands, respectively.

5.5 Phonon frequencies

Raman and infrared [107–111] spectroscopes are experimental probes of the phonon frequencies of a molecule or solid. In this section, the impact of filtered basis sets on the calculation of bulk phonon modes associated with pure diamond and silicon will be considered. Modes may be classified as acoustic (lower three branches) or optical (higher three branches) [112]. Modes can further be classified as transverse or longitudinal and in diamond or silicon the transverse modes are degenerate at high symmetry points (such as X or L). A schematic diagram of a phonon spectrum is given in figure 5.6. Computationally, the phonon frequencies are obtained by finding the double-derivatives of the energy with respect to atomic displacements, which are computed numerically using a difference of forces. Diagonalizing the resulting dynamical matrices yields the frequencies. Previously, no results examining this quantity with the filtration method have been published.

5.5.1 Simulation details

The calculations will address phonon frequencies at the Γ, X and L points, and will compare frequencies obtained in filtered basis calculations with experiment and non-filtered `AIMPRO` findings. The nature of a phonon mode with a non-zero wave-vector is that atoms in different unit cells have different phases of oscillation. As such it is not possible to obtain these from a primitive two atom unit cell, just by calculating energies or forces corresponding to different displacements. However, such a phonon mode can be modelled using a unit cell of twice the size. Hence, in this work the Γ-point phonon modes are calculated in a 16 atom (fcc) cell. The frequencies and displacement patterns of these will incorporate those of the primitive cell at Γ and the zone boundary X and L points. Our calculations are performed using supercells containing 16-host carbon or silicon atoms. All quantities have been calculated using LDA and GGA functional. In order to give strong evidence on the accuracy of the filtration method, we used many values of filtration radius (R_c) from 6 to 10 (a.u.) in

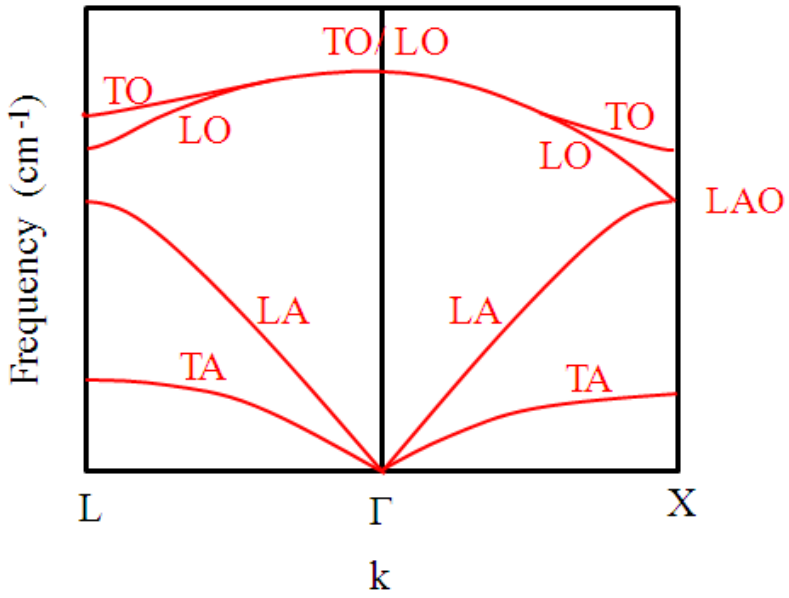

Figure 5.6: Schematic dispersion curves for acoustic and optical phonons in silicon. The special points are $\Gamma = (000)$, L=$\frac{\pi}{a}(111)$ and X=$(\frac{2\pi}{a})(100)$. The (TA), (LA), (LO) and (TO) phonon branches are at the zone boundary position, $K = (\frac{\pi}{a})(111)$, the (TA), (LAO) and (TO) phonon branches are at zone boundary position $K(\frac{2\pi}{a})(100)$, and the (TO/LO) phonon branch is at $K = 000(\Gamma\text{-point})$.

diamond, and from 8 to 12 (a.u.) in silicon, for more detailed information see section 3.3 in chapter 3. In all cases, we employ the Monkhorst-Pack [60] scheme for sampling the Brillouin zone, with a mesh of 2^3 special k points. The phonon frequencies of bulk diamond in various non-primitive supercells (only 16-host atom) are calculated using finite difference approximations for the derivatives of the forces with respect to the displacement of the atoms from the equilibrium sites, followed by the construction of the dynamical matrix from which the phonon frequencies are found in the usual way. The force constants were obtained by shifting atoms in three directions (x, y and z) by 0.1 a.u), with a cutoff of 175 Ry to expand the charge density using plane waves, to yield well-converged values of the vibrational modes. The calculations have been

repeated by using three different values of the shifts, with cutoff 400 Ry.

Diamond

The resulting phonon frequencies are shown in table 5.11, along with the mean error associated with the filtration method. In addition, by comparing our results with the experimental values, we find that the mean differences with conventional calculations is typically 5.4% with the LDA, and with the GGA is typically 5.7% (see table 5.13) and the mean difference between the LDA and GGA is 0.33%. Overall, we can conclude that the effect of the filtration approximation is small on either of these scales and is also smaller than other internal convergence parameters. As final test, table 5.12 shows that the maximum differences associated with convergence in the plane wave cut-off (R_c) are typically 0.55 cm^{-1} and 4.8 cm^{-1} with the LDA and GGA respectively, and the maximum differences associated with choice of shifting employed in numerical differencing are 1.35 cm^{-1} and 10 cm^{-1} with the LDA and GGA respectively. Finally, our results are in reasonably good agreement with other reported computational values. These simulation findings appear to give good support for the filtration method.

Silicon

For more evidence on the accuracy of the filtration technique, we shall now use silicon as a material for testing. The resulting phonon frequencies are shown in table 5.14, which also presents the mean error associated with the filtration method. In addition, by comparing our results with the experimental values, we find that the mean differences with a conventional calculation is typically 6.29% with the LDA, and with the GGA is typically 5.78%, see table 5.16 and the mean difference between the LDA and GGA is 0.76%. In comparison, the shift associated with filtration is 0.6 %. Overall, we can conclude that the effect of the filtration approximation is negligible when compared with experiment and is also smaller than other internal convergence parameters. As a final test, table 5.15 shows that differences associated with convergence

Table 5.11: Optical and acoustical phonon frequencies (in cm^{-1}), showing the values at three points $K = 0, K = (\frac{2\pi}{a_0})(100)$, and $K = (\frac{\pi}{a_0})(111)$ in diamond using the LDA and GGA. R_c is in a.u. The errors are given with respect to unfiltered calculations. Frequencies are given as a function of cut-off (R_c).

Symmetry	Phonon	LDA					
point	branch	$R_c = 6$	$R_c = 7$	$R_c = 8$	$R_c = 10$	$R_c = \infty$	Exp [113]
L	(TA)	546.10	547.70	549.69	549.52	549.70	563
X	(TA)	777.65	778.30	785.88	785.67	785.35	807
L	(LA)	1064.09	1063.45	1067.84	1066.60	1065.27	1006
X	(LAO)	1088.59	1087.80	1088.50	1088.19	1085.90	1185
L	(TO)	1204.94	1202.19	1210.68	1211.02	1211.22	999
X	(TO)	1224.33	1223.26	1223.22	1222.48	1220.59	1206
L	(LO)	1252.017	1249.75	1257.67	1258.21	1258.59	1252
Γ	(TO/LO)	1319.88	1318.25	1317.306	1316.61	1314.43	1332
M.abs.error		4.65	4.64	1.58	1.10	0.00	—
M.per.error		0.45	0.45	0.14	0.10	0.00	—
		GGA					
L	(TA)	532.10	536.04	537.83	544.11	544.99	563
X	(TA)	768.65	768.36	778.06	777.03	776.33	807
L	(LA)	1033.24	1033.47	1039.21	1032.49	1029.91	1006
X	(LAO)	1051.60	1050.18	1051.64	1050.39	1047.79	1185
L	(TO)	1182.72	1178.89	1185.09	1183.74	1183.14	999
X	(TO)	1185.54	1185.77	1186.01	1188.03	1185.71	1206
L	(LO)	1234.01	1232.96	1242.52	1238.34	1237.77	1252
Γ	(TO/LO)	1286.05	1283.15	1281.05	1287.51	1283.86	1332
M.abs.errors		4.28	4.09	3.98	1.74	0.00	—
M.per.errors		0.57	0.51	0.45	0.17	0.00	—

Table 5.12: Optical and acoustical phonon frequencies (in cm^{-1}), showing the values at three points $K = 0, K = (\frac{2\pi}{a_0})(100)$, and $K = (\frac{\pi}{a_0})(111)$, by shifting the values of phonon frequencies (in a.u) for different locations in diamond using the LDA and GGA.

LDA					
Symmetry point	Phonon branch	e-cut=400 a.u			e-cut=175 a.u
		Shift=0.1	Shift=0.01	Shift=0.05	Shift=0.1
L	(TA)	548.51	549.86	549.15	549.70
X	(TA)	784.52	785.70	785.14	785.35
L	(LA)	1064.66	1065.18	1064.79	1065.27
X	(LAO)	1085.30	1085.92	1085.58	1085.90
L	(TO)	1210.39	1211.21	1211.04	1211.22
X	(TO)	1220.06	1220.86	1220.49	1220.60
L	(LO)	1258.08	1258.93	1258.57	1258.59
Γ	(TO/LO)	1313.94	1314.85	1314.46	1314.43
GGA					
Symmetry point	Phonon branch	e-cut=400 a.u			e-cut=175 a.u
		Shift=0.1	Shift=0.01	Shift=0.05	Shift=0.1
L	(TA)	543.33	536.22	541.62	544.99
X	(TA)	778.78	777.58	781.14	776.33
L	(LA)	1030.76	1040.81	1032.06	1029.91
X	(LAO)	1049.50	1048.55	1051.01	1047.79
L	(TO)	1182.76	1182.11	1184.38	1183.14
X	(TO)	1184.96	1192.69	1184.69	1185.71
L	(LO)	1238.47	1247.38	1239.93	1237.77
Γ	(TO/LO)	1281.20	1276.71	1280.20	1283.86

Table 5.13: Mean percentage error between AIMPRO unfiltered and filtered calculations with experiment values for phonon frequencies. R_c is in au.

Errors	$R_c = 6$	$R_c = 7$	$R_c = 8$	$R_c = 9$	$R_c = 10$	$R_c = \infty$
M.per.errors (LDA)	5.45%	5.40%	5.43%	5.48%	5.43%	5.45%
M.per.errors (GGA)	6.15%	6.07%	5.93%	5.82%	5.68%	5.73%

in the plane wave cut-off is typically 0.5cm^{-1} (0.05%) and the difference associated with choice of shifting employed in numerical differencing is 0.12 cm^{-1} (0.012%) — smaller than all other errors encountered in this section. Finally, our LDA and GGA calculations for both basis functions are in good agreement with the experimental values.

5.6 Specific heat capacity

Phonon frequencies are one of the important physical properties which depend sensitivity on the material being concerned. They also influence many properties of the system especially thermodynamic quantities, such as specific heat capacity C_v [116]. The heat capacity property at constant volume can be calculated by several methods from equation 4.6, as we stated in section 5.5.1.

5.6.1 Simulation details

The gamma–point phonon frequencies computed using 216 atom carbon and silicon atoms unit cells. Before the heat capacity calculation, the geometry is optimized fully with the standard and filtered basis set functions. All other simulation details are as described in section 5.5.1.

Table 5.14: Optical and acoustical phonon frequencies (in cm^{-1}),showing the values at three points $K = 0, K = (\frac{2\pi}{a_0})(100)$, and $K = (\frac{\pi}{a_0})(111)$ in silicon using the LDA and GGA. R_c is in au.

Symmetry	Phonon	LDA					
point	branch	$R_c = 9$	$R_c = 10$	$R_c = 11$	$R_c = 12$	$R_c = \infty$	Exp [114, 115]
L	(TA)	104.21	104.21	104.31	108.17	105.79	114
X	(TA)	132.07	132.07	131.36	135.59	134.58	149
L	(LA)	372.20	372.20	371.16	372.52	371.70	374
X	(LAO)	407.96	407.96	407.52	409.87	408.80	412
L	(TO)	412.30	412.30	412.33	413.04	412.35	491
X	(TO)	462.11	462.11	462.38	462.15	460.64	463
L	(LO)	490.97	490.97	490.79	491.32	489.45	426
Γ	(TO/LO)	514.58	514.58	515.04	516.62	513.86	517
M.abs.errors		1.15	1.15	1.35	1.51	0.00	—
M.per.errors		0.56	0.56	0.64	0.61	0.00	–
		GGA					
L	(TA)	114.57	114.57	114.90	112.80	112.47	114
X	(TA)	150.52	150.52	150.84	147.39	147.10	149
L	(LA)	368.43	368.43	368.36	367.79	368.06	374
X	(LAO)	397.76	397.76	397.59	396.15	395.50	412
L	(TO)	398.18	398.18	397.70	397.61	397.19	491
X	(TO)	444.54	444.54	444.63	443.35	442.02	463
L	(LO)	474.52	474.52	474.68	473.93	472.49	426
Γ	(TO/LO)	500.16	500.16	499.83	500.80	498.71	517
M.abs.errors		1.89	1.89	1.87	0.85	0.00	—
M.per.errors		0.80	0.80	0.84	0.23	0.00	–

Table 5.15: Unfiltered optical and acoustical phonon frequencies, showing the values at three points $K = 0, K = (\frac{2\pi}{a_0})(100)$, and $K = (\frac{\pi}{a_0})(111)$, by shifting the values of phonon frequencies (in au) for different locations in silicon using LDA and GGA.

		LDA			
Symmetry	Phonon	e-cut=400 a.u			e-cut=175 a.u
point	branch	Shift=0.1	Shift=0.01	Shift=0.05	Shift=0.1
L	(TA)	105.83	105.99	105.96	105.79
X	(TA)	134.61	134.88	134.81	134.58
L	(LA)	371.71	371.85	371.82	371.70
X	(LAO)	408.81	408.89	408.87	408.80
L	(TO)	412.36	412.41	412.38	412.35
X	(TO)	460.65	460.69	460.68	460.64
L	(LO)	489.46	489.54	489.52	489.45
Γ	(TO/LO)	513.87	513.99	513.96	513.86
		GGA			
Symmetry	Phonon	e-cut=400 a.u			e-cut=175 a.u
point	branch	Shift=0.1	Shift=0.01	Shift=0.05	Shift=0.1
L	(TA)	112.61	112.96	112.75	112.47
X	(TA)	147.24	147.70	147.46	147.10
L	(LA)	368.09	368.26	368.20	368.06
X	(LAO)	395.53	395.55	395.55	395.50
L	(TO)	397.22	397.27	397.28	397.19
X	(TO)	442.05	442.05	442.07	442.02
L	(LO)	472.52	472.54	472.56	472.49
Γ	(TO/LO)	498.73	498.78	498.81	498.71

Table 5.16: Mean percentage errors between AIMPRO (unfiltered and filtered) calculations with experiment values for phonon frequencies, R_c is in a.u.

Errors	$R_c = 9$	$R_c = 10$	$R_c = 11$	$R_c = 12$	$R_c = \infty$
M.per.errors (LDA)	6.67%	6.67%	6.74%	5.81%	6.29%
M.per.errors (GGA)	5.50%	5.50%	5.60%	5.66%	5.78%

Diamond

From table 5.17, we compare the values of the heat capacities obtained by using filtered and unfiltered techniques, where the specific heat capacities have been calculated at 300 K and 800 K, together with the zero point energy.

From the table we can see that the absolute errors between filtered and unfiltered calculations at T=300 K is smaller than the error between unfiltered and experimental results with both functionals. In addition, the percentage errors in the simulation methods are much smaller than the percentage errors between the unfiltered AIMPRO findings and the experimental value. Furthermore both calculations the experimental value, and computationally are substantially close. By checking the calculated values of C_v computed by unfiltered and filtered basis functions, we found that there is no important impact from filtration on our findings. This emphasises the fact that the filtration technique works well and is without significant impact upon the accuracy of the calculations.

Silicon

From table 5.18, comparing values of the filtered and unfiltered C_v with each other and with the experimental values, we note that these values are very close to each other, for both functionals. Also, the absolute errors and the percentage errors are largely small, in all cases. The LDA results are slightly lower than GGA values, and

Table 5.17: Thermodynamic parameters of cubic diamond using the LDA and GGA functionals: specific heat at constant volume C_v (J/mol K) at T=300 K and 800 K and zero-point energy (ZPE) (kJ/mol) are shown. R_c is in (a.u).

	LDA			GGA		
R_c	ZPE	C_v(300 K)	C_v(800 K)	ZPE	C_v(300 K)	C_v(800 K)
8	17.996	6.375	19.575	17.524	6.725	19.906
9	17.989	6.382	19.578	17.517	6.732	19.831
10	17.986	6.384	19.581	17.500	6.746	19.830
∞(unfilt)	17.980	6.388	19.584	17.508	6.738	19.836
Exp [117]	-	6.19	-	-	6.19	-
Abs-errors						
unfilt *vs* filt (Mean)	0.010	0.007	0.006	0.011	0.009	0.027
Exp *vs* unfilt	-	0.190	-	-	0.545	-
Per-errors						
unfilt *vs* filt (Mean)	0.057%	0.119%	0.030%	0.062%	0.133%	0.031%
Exp *vs* unfilt	-	3.074%	-	-	8.808%	-

also underestimate the experimental values, in contrast for the GGA calculations. Furthermore, both calculations give acceptable values. However, these findings show that the LDA results are slightly lower than GGA values, and also underestimate the experimental values, in contrast for the GGA calculations. These comparisons indicate that the filtration technique works accurately.

Table 5.18: Thermodynamic parameters of cubic silicon using the LDA and GGA functionals: specific heat at constant volume C_v (J/mol K) at T=300 K and 800 K, and zero-point energy (ZPE) (kJ/mol) are shown. R_c is in (a.u).

	LDA			GGA		
R_c	ZPE	C_v(300 K)	C_v(800 K)	ZPE	C_v(300 K)	C_v(800 K)
10	6.024	20.336	24.597	5.932	20.524	24.638
11	6.117	20.257	24.584	5.928	20.530	24.639
12	6.126	20.249	24.583	5.928	20.530	24.639
∞(unfilt)	6.098	20.279	24.588	5.920	20.540	24.641
Exp [117]	6.00	20.05	-	6.00	20.05	-
Abs-errors						
unfilt *vs* filt (Mean)	0.040	0.036	0.006	0.009	0.012	0.002
Exp *vs* unfilt	0.091	0.248	-	0.073	0.481	-
Per-errors						
unfilt *vs* filt (Mean)	0.661%	0.179%	0.024%	0.157%	0.057%	0.009%
Exp *vs* unfilt	1.521%	1.148%	-	1.216%	2.399%	-

5.7 Conclusion

Density functional simulations of bulk diamond and silicon have largely confirmed that the use of filtered basis functions to calculate the lattice constant and bulk modulus as a function of total energy in diamond and silicon have given good agreement with the standard `AIMPRO` calculations and with the experiments findings. Further, band structures produced in filtered basis calculations differ from standard calculations by only 1–10 meV in the valence band. Finally, it is also noted that the phonon

frequencies and the heat capacities also demonstrate the accuracy and utility of the filtration results. Our tests therefore show that many physical properties can be addressed accurately using a filtered basis set.

Chapter 6

Semiconductor Surfaces

6.1 Introduction

Surfaces of semiconductors are extremely important for many reasons. They are important technologically [118–122], an understanding of them can be an ingredient of modelling growth and there have been many previous attempts to model them using DFT [123, 124]. They are also in one sense the most fundamental "defect" of a solid.

In this chapter clean surfaces will be modelled first, that is surfaces which are not terminated by an impurity layer (such as CH bonds for diamond). An ideal surface can be imagined to be created by cleaving a crystal across a crystallographic plane, with the (100), (110) and (111) planes being most important for diamond and silicon. The resulting structure will have dangling bonds at the surface (two per atom for (100), one per atom for (110) or (111) surfaces). These surfaces are unstable against reconstruction. For example, a simple chemical rebonding of the atoms in pairs on the (100) face will reduce the number of dangling bonds to one per atom, making the surface more stable. The resulting surface is known as a 1×2 reconstructed surface. Reconstructions are possible on (100) [125] (110) surface [126] and the (111) surface [127].

The purpose of the modelling performed here is to compare filtered with non-

filtered calculations. This is in some respects an important test, as it could (erroneously) be suggested that the concept of a spherical cut-off region in filtration may be less accurate in an extremely inhomogeneous system and a surface is an extreme case of inhomogeneity. The results presented here will show that this is not so, and filtration performs well. The tests that will be applied to filtration will be to reproduce the modelled surface reconstructions and also the resulting surface energy per 1×1 surface unit cell and the resulting band structures. Calculated values can also be compared with previous published values using other codes.

A second property that can be considered here is the electron affinity. The hydrogenated [128] C(111)-1×1:H surface of diamond has been found to have a negative electron affinity (NEA) [2, 129–131], which gives diamond a valuable technological property, important in applications such as efficient photoemitters or electron multipliers. The key feature for this is that the vacuum level should be lie below the conduction band minimum (CBM). In all these calculations Gaussian functions are used as a starting basis for the filtered and unfiltered basis functions for the expansion of the one-electron wave functions. A study of these will give a good test of the filtration process and how accurately it treats the extreme inhomogeneity of a surface.

6.2 Computational method

Our calculations have been carried out using the density functional technique, implemented in the `AIMPRO` *ab initio* simulation package [16, 33, 103, 104]. To model the various surfaces, 14, 28, 30, 40, and 44 atom supercells have been used and details of these with be given the calculations later in this chapter. The total energies are calculated using density functional theory (DFT) and in the local-density and general gradient approximations (LDA and GGA) developed by Perdew-Wang [45] and Perdew, Burke and Ernzerhof [105] respectively. The pseudo-potentials of Hartwigsen, Goedecker and Hutter [51] are used to treat the electron-ion interaction. The Kohn-Sham eigenfunctions are expanded using atom-centered Gaussian basis sets, which

consist of independent s, p and d type Gaussian functions of differing widths for each carbon and silicon atom. In this (unfiltered) case this gives a total of 40 functions per atom. Filtration was performed starting from this same primitive basis reducing the number of functions from 40 to 4. A minimization of the total energy of the system with respect to the atomic coordinates was performed using the conjugate-gradient scheme [56, 57], with the structure optimization continuing until the forces on atoms are less than 10^{-4} a.u., and the total energy of the final optimal structure changing by much less than 10^{-5} Ha. A plane wave expansion of the density and Kohn-Sham potential is used to determine the Hamiltonian matrix elements with a cutoff of 175 Ha. for diamond and 40 Ha. for silicon. For all surfaces, Monkhorst-Pack sampling grids [60] were used to sample the Brillouin zone, also in all surface calculations the Brillouin zone was two dimensional. Figure 6.1, 6.2 show cross-sections through different diamond and silicon structures.

As described in chapter 4, the electron affinity (EA) of a diamond surface is defined as the energy difference between the vacuum level and the conduction band minimum in perfect diamond. In order to calculate the EA, we have adopted the standard practice [102, 129, 132–134] of calculating the electrostatic potential for a slab of diamond, averaging this across the plane of the slab, and examining the result as a function of distance above and below the surface. This establishes the position of the vacuum level relative to the potential in the diamond. A second calculation, this time of the electrostatic potential in bulk diamond then positions the valence band maximum relative to this vacuum level. The conduction band minimum is then established by adding the experimental value of the band gap (5.47 eV) to the valence band maxima (VBM). The LDA band gap is underestimated, and so is not used for this purpose.

6.3 Simulation details

This study focuses mainly on the (111)-2×1, (111)-1×1, (110)-1×1 and (100)-2×1 surfaces in diamond and silicon. Computationally, the surfaces have been geometrically

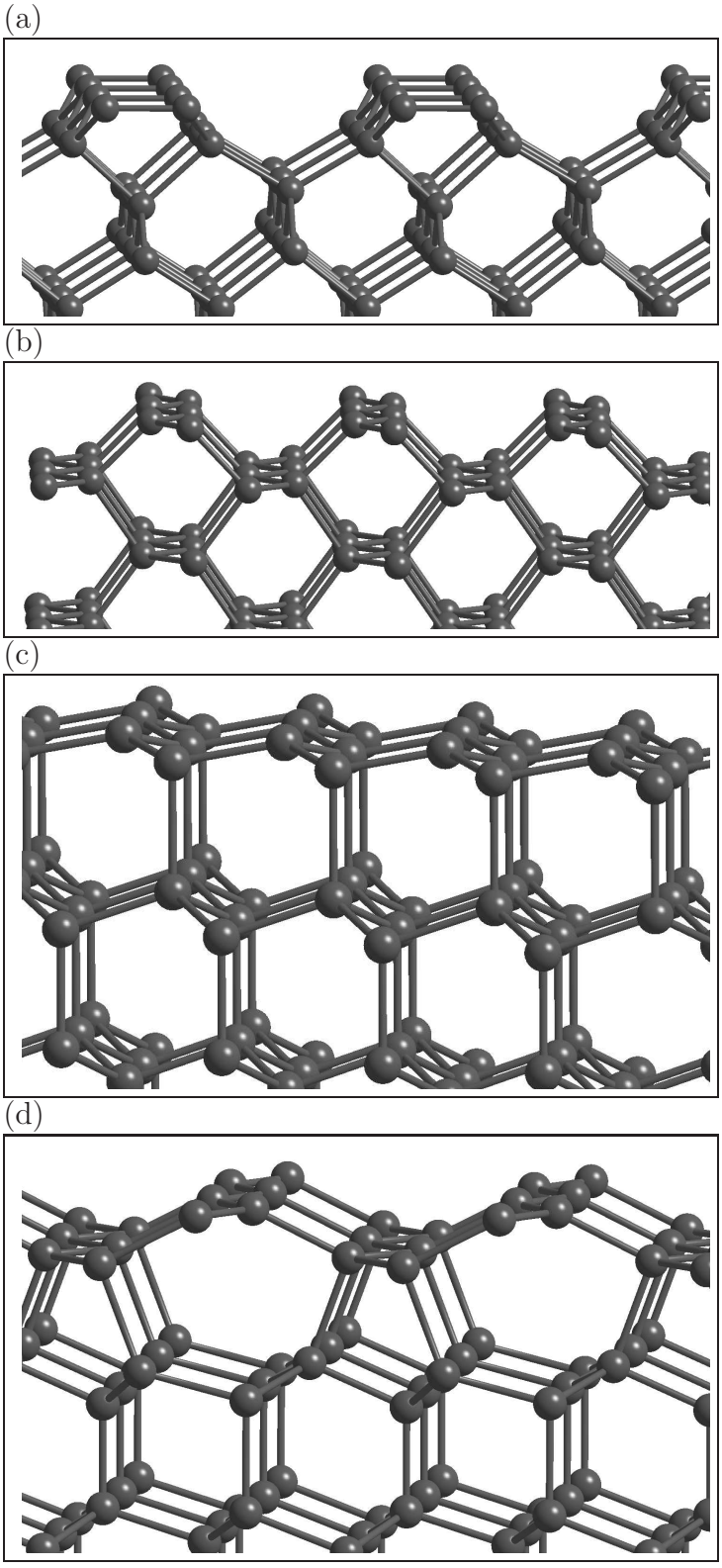

Figure 6.1: Perspective view of the stable atomic geometries for (a) the clean (100)-2×1, (b)(110)-1×1, (c) (111)-1×1, and (d) (111)-2×1 diamond surfaces.

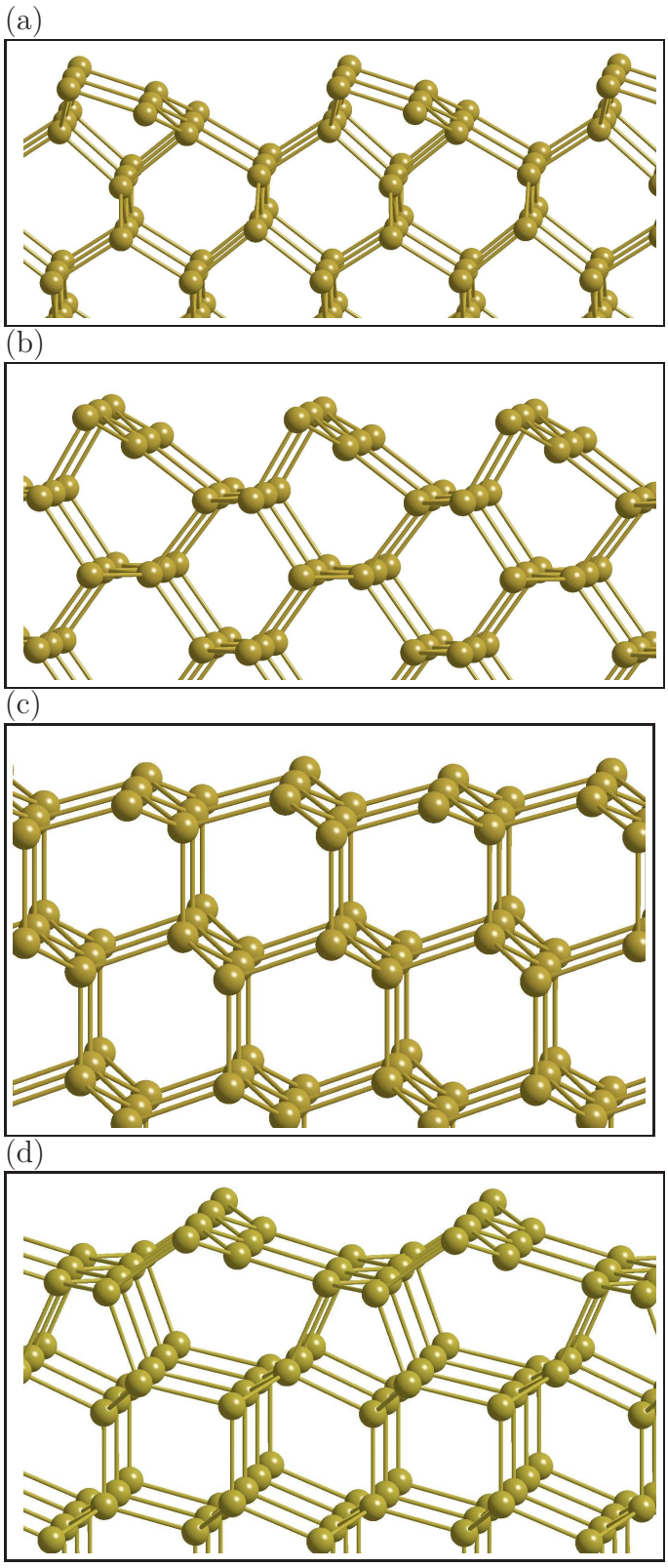

Figure 6.2: Perspective view of the stable atomic geometries for (a) the clean (100)-2×1, (b) (110)-1×1, (c) (111)-1×1, and (d) (111)-2×1 silicon surfaces.

formed by reconstructing the atoms at the surface of the structures. The modelling details are described previously in section 5.1. For the bulk materials (diamond and silicon), the lattice constants (a_0) were determined to be 3.530 Å and 5.382 Å respectively in the DFT-LDA calculations (carried out in two atom, face-centred cubic unit cells, with BZ sampling of a 8×8×8 mesh of grid points, leading to a total of 60 non-equivalent k-points generated by the Monkhorst-Pack scheme [60]). To simulate various surface orientations, we need to model a periodic arrangement of slabs, where each slab possesses a specific number of atomic layers which are restricted to the surface unit cell. To avoid the interaction which would occur between the slabs, the layers have been separated by a sufficiently wide region of vacuum. A calculation of the absolute surfaces energies as described in the section 4.9.1 requires the calculation of the values of the chemical potentials for the atoms present. This has been done separately for each filtration cutoff and the results are presented in table 6.1. The absolute surface energy (per 1×1 surface cell) and electron affinity have been calculated as stated in equation 4.13 respectively in the chapter 4.

Table 6.1: The table shows the values of chemical potentials (μ in Ha) of carbon and silicon atoms as a function of filtration cut-off, (R_c in a.u).

R_c	6	7	8	10	12	∞
μ(C)	5.7133	5.7134	5.7138	5.7139	–	5.7140
μ(Si)	3.9600	–	3.9655	3.9662	3.9664	3.9666

Four types (orientation / reconstruction) of the surface were considered. In calculations of the clean surface energies [99, 135], the size and the shape of the BZ and its irreducible part, will vary with the orientation of the surface. To model clean carbon and silicon surfaces with (111)-2×1, (110)-1×1 and (100)-2×1 orientations, simple-orthorhombic (ort-p) supercells were used. The (111)-1×1 surface is simulated

using a hexagonal cell as shown in figure 6.3, the Brillouin zone integration was carried out using a 8×4×1 grid for the 2×1 reconstruction and an 8×8×1 grid for the 1×1 reconstruction. These grid meshes in the irreducible part of the BZ correspond to 8(2×1) and 20 (1×1) k-points, respectively.

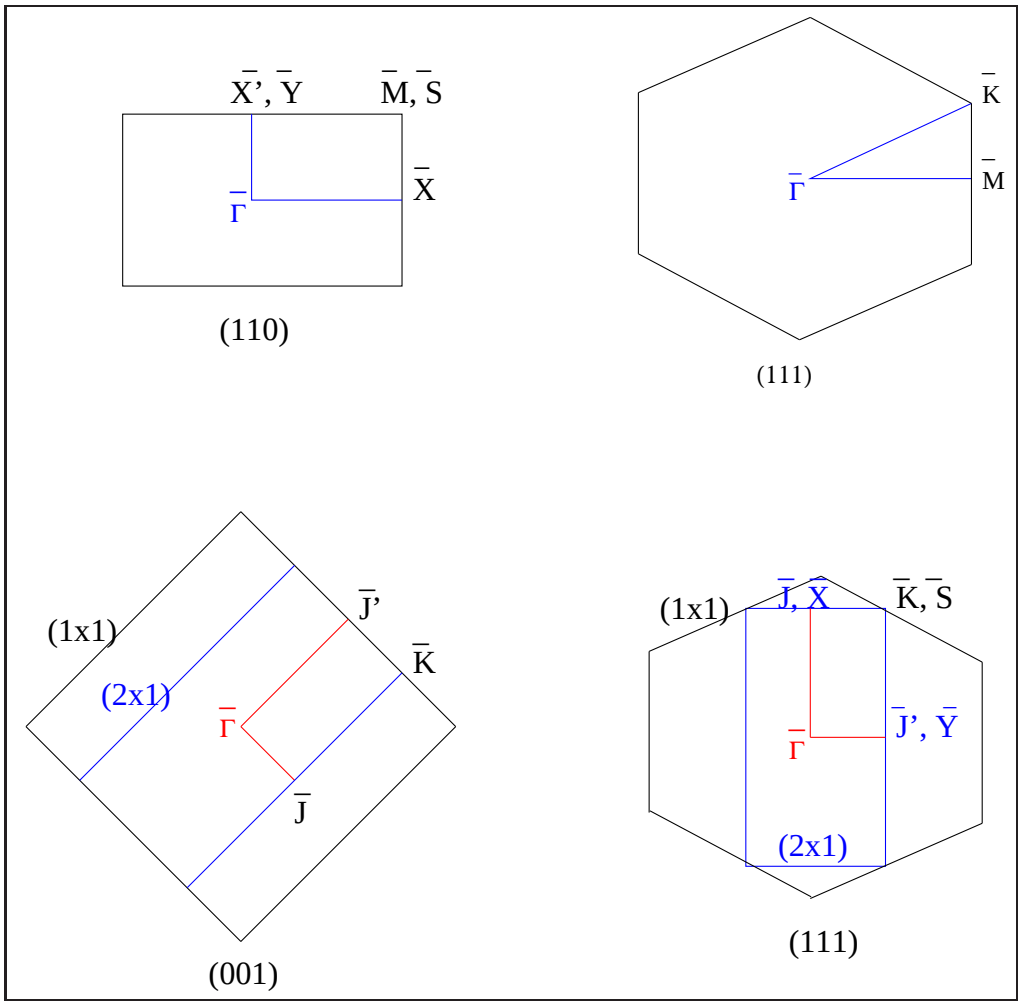

Figure 6.3: Surface Brillouin zones for the (110), (111), and (001) surfaces of zincblende-compound semiconductors. The lower part shows the Brillouin zones of (1×1) and (2×1) surfaces geometries.

Table 6.2: Details of the orientations and reconstructions, symmetries and lattice parameters of four surfaces investigated in diamond.

Surface	Lattice type	Sym	N of atom	Parameter/a.u a	b	c	Sampling
(100)-(2×1)	ort-p	C_2	44	4.719	9.439	60.000	8×4×1
(110)-(1×1)	ort-p	D_{2h}	28	4.719	65.000	6.674	8×1×6
(111)-(1×1)	hex-p	D_{3d}	14	4.719	-	50.509	8×8×1
(111)-(2×1)	ort-p	C_{2h}	40	4.719	8.174	60.000	8×5×1

Table 6.3: Details of the orientations and reconstructions, symmetries and lattice parameters of four surfaces investigated in silicon.

Surface	Lattice type	Sym	N of atom	Parameter/a.u a	b	c	Sampling
(100)-(2×1)	ort-p	C_2	44	7.195	14.390	80.000	8×4×1
(110)-(1×1)	ort-p	D_{2h}	30	7.195	90.000	10.175	8×1×6
(111)-(1×1)	hex-p	D_{3d}	14	7.195	-	77.002	8×8×1
(111)-(2×1)	ort-p	C_{2h}	40	7.195	12.462	90.000	8×5×1

6.4 Simulation of Diamond Surfaces

6.4.1 Surface energies

The computational method is as described in section 6.2. Specific details of the parameters of the unit cells used are shown in table 6.2. All parameters have estimated

Table 6.4: Absolute surface energies $E_{surf}^{n\times m}$ (eV/1×1 cell) for various orientations and reconstructions in diamond, (R_c in a.u). The previous theory calculations used the LDA.

Orientation	No atom	R_c	E_{surf}^{LDA}	E_{surf}^{GGA}	Previous theory
		7	2.215	1.976	
(100)-(2×1)	44	8	2.209	1.972	2.222 [99]
		10	2.204	1.966	2.12 [134]
		∞	2.202	1.964	
		7	3.373	3.043	
(110)-(1×1)	28	8	3.372	3.027	3.264 [99]
		10	3.362	3.018	
		∞	3.359	3.015	
		7	2.217	2.009	
(111)-(1×1)	14	8	2.210	2.005	2.165 [99]
		10	2.205	2.002	2.18 [134]
		∞	2.206	2.001	2.151 [136]
		7	1.425	1.243	
(111)-(2×1)	40	8	1.426	1.240	1.369 [99]
		10	1.418	1.234	1.35 [134]
		∞	1.416	1.232	1.356 [136]

by filtered and unfiltered basis functions. To estimate the computational errors, we computed the clean surface energies of the diamond surfaces using several filtration cut-off radii as shown in the table 6.4. In this section, calculations of the surface energies are performed using filtered and unfiltered basis sets, and the results are compared with the previous theory in table 6.4. It is seen from table 6.4 that the values of all surface energies, with the LDA functional, filtered with R_c=10 a.u. are in agreement with unfiltered data to within 1-3 meV, while the GGA functional is similar, apart from a small 3 meV error per 1×1 cell for the (110) orientation. A cut-off of 10 a.u. gave an error of order 1 meV. However, compared with previous theory, the differences are 10-40 meV per 1×1 cell. This is due to differences of pseudopotential and basis set. In conclusion, the effect of basis set filtration has been to introduce a very much smaller error to the calculations compared to the uncertainly which is present in all calculation due to more fundamental approximations (i.e. pseudopotential). Also the differences between the LDA and PBE-GGA is much larger (up to 200 meV) again emphasising that the 1 meV filtration error is insignificant. Our results confirm that the filtration modelling technique has substantially maintained the accuracy of the calculations and indicate its applicability for extremely inhomogeneous systems such as surfaces or interfaces.

6.4.2 Band structure

The band structures for the clean surfaces in diamond were found using the unit cells shown in table 6.2. The band structures of all structures in diamond in the vicinity of the band gap along high-symmetry directions are shown in figure 6.4. The mean differences in the energies of occupied states with $R_c = 8$ a.u. at Γ-point are 0.006 eV for (100)-2×1, 0.014 eV for (110)-1×1, 0.016 eV for for (111)-1×1 and 0.014 eV for (111)-2×1 with the LDA functional. In particular, the positions of the surface related states throughout the graphs in the figures 6.4 are very well reproduced by filtered calculations. Through these results, we find that the filtration modelling technique has kept he accuracy of the calculation of the band structure largely unaffected.

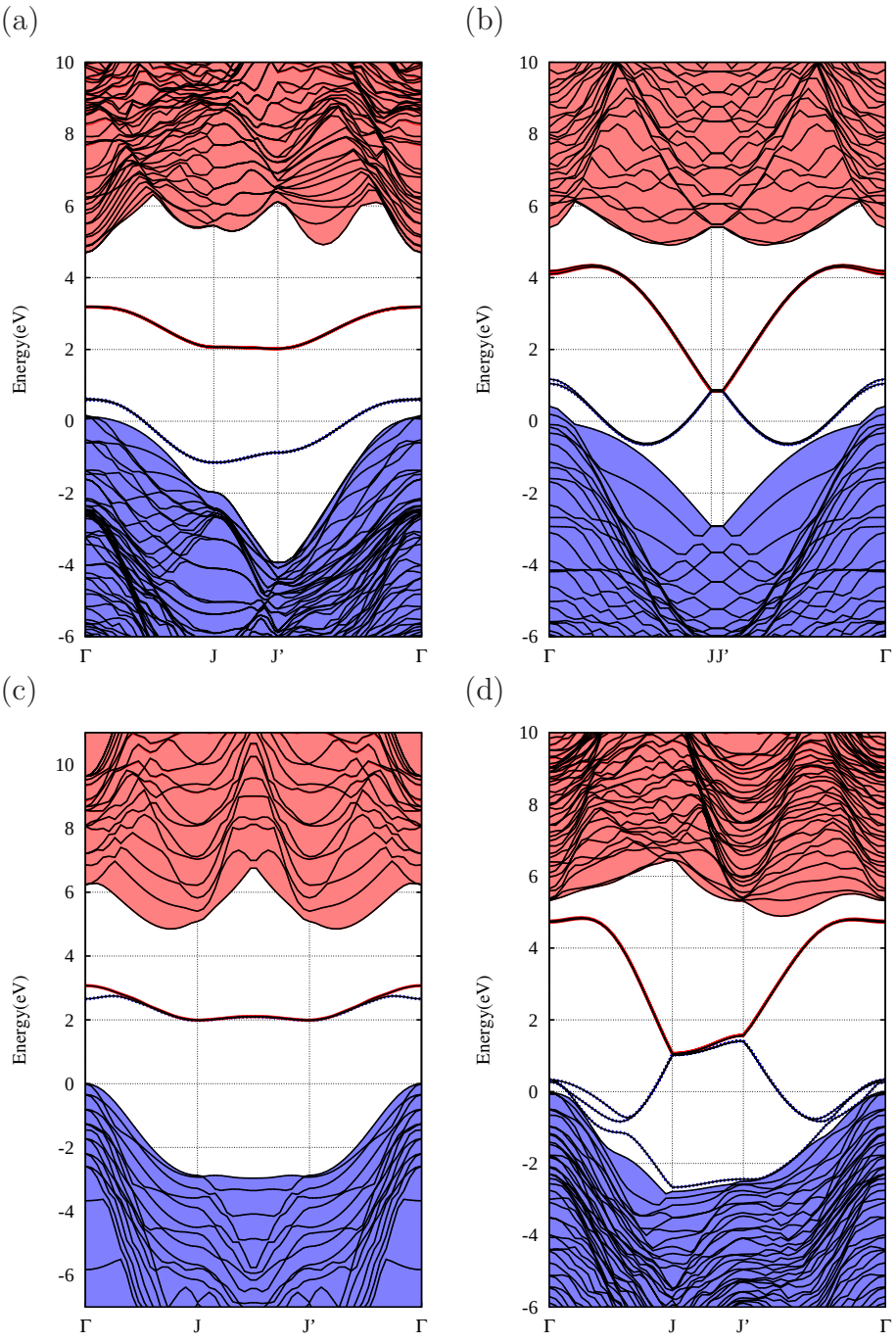

Figure 6.4: Schematic pictures of the clean diamond surface of band structures for (a) (100)-2×1, (b) (110)-1×1, (c) (111)-1×1, and (d) (111)-2×1 directions. Blue and red shading crosses indicate filled and empty bands, which are calculated by standard method, respectively, while black lines indicate the comparable bands of clean surfaces, which are computed by the filtration method.

The present study confirms the previous findings for bulk materials are also valid in surface calculations, and contributes additional evidence that the filtration modelling method works with high accuracy.

6.5 Simulation of Silicon Surfaces

6.5.1 Surface energies

We now turn to a study of the four corresponding surfaces of silicon. The simulation details of the surfaces are shown in table 6.3. In this section, calculations of the surface energies are performed using filtered and unfiltered basis sets, and the results are compared with previous theory. During simulation, we noted that the values of GGA surface energies for all surfaces, filtered with R_c=10 a.u. in very close (1 meV) agreement with unfiltered calculations, while the LDA results are very similar. However, differences with previous theory are 10-30 meV per 1×1 cell. This is due to a different pseudopotential and basis set. Also the difference between LDA and PBE values is up to 150 meV per 1×1 cell. In conclusion, energies are in good agreement with a maximum difference of only 7 meV per 1×1 cell.

6.5.2 Band structure

The band structures for the clean surfaces in silicon were found using the unit cells as shown in the table 6.3. The band structures of all structures in silicon in the vicinity of the band gap along high-symmetry directions are shown in figure 6.5. The mean differences in the energies of occupied states with R_c = 10 a.u. at Γ-point are 0.05 eV for (100)-2×1, 0.06 eV for (110)-1×1, 0.09 eV for (111)-1×1 and 0.07 eV for (111)-2×1 with the LDA functional. In particular, the positions of the surface related states throughout the graphs in the figures 6.5 are very well reproduced by filtered calculations. Through these results, we found that the filtration modelling technique has kept the accuracy of the calculation of the band structure largely unaffected. The

Table 6.5: Absolute surface energies $E_{surf}^{n\times m}$ (eV/1×1 cell) for various orientations and reconstructions in silicon, R_c in a.u.

Orientation	No atom	R_c	E_{surf}^{LDA}	E_{surf}^{GGA}	Published [99]
(100)-(2×1)	44	6	1.388	1.216	1.321
		8	1.334	1.329	
		10	1.344	1.341	
		∞	1.345	1.344	
(110)-(1×1)	30	6	2.520	1.907	2.190
		8	2.195	2.046	
		10	2.209	2.053	
		∞	2.211	2.059	
(111)-(1×1)	14	6	1.468	1.179	1.372
		8	1.389	1.293	
		10	1.386	1.299	
		∞	1.385	1.301	
(111)-(2×1)	40	6	1.241	0.954	1.141
		8	1.136	1.085	
		10	1.144	1.084	
		∞	1.145	1.091	

present study confirms the previous findings for bulk materials also applying in surface calculations and contributes additional evidence that the filtration modelling method works with high accuracy.

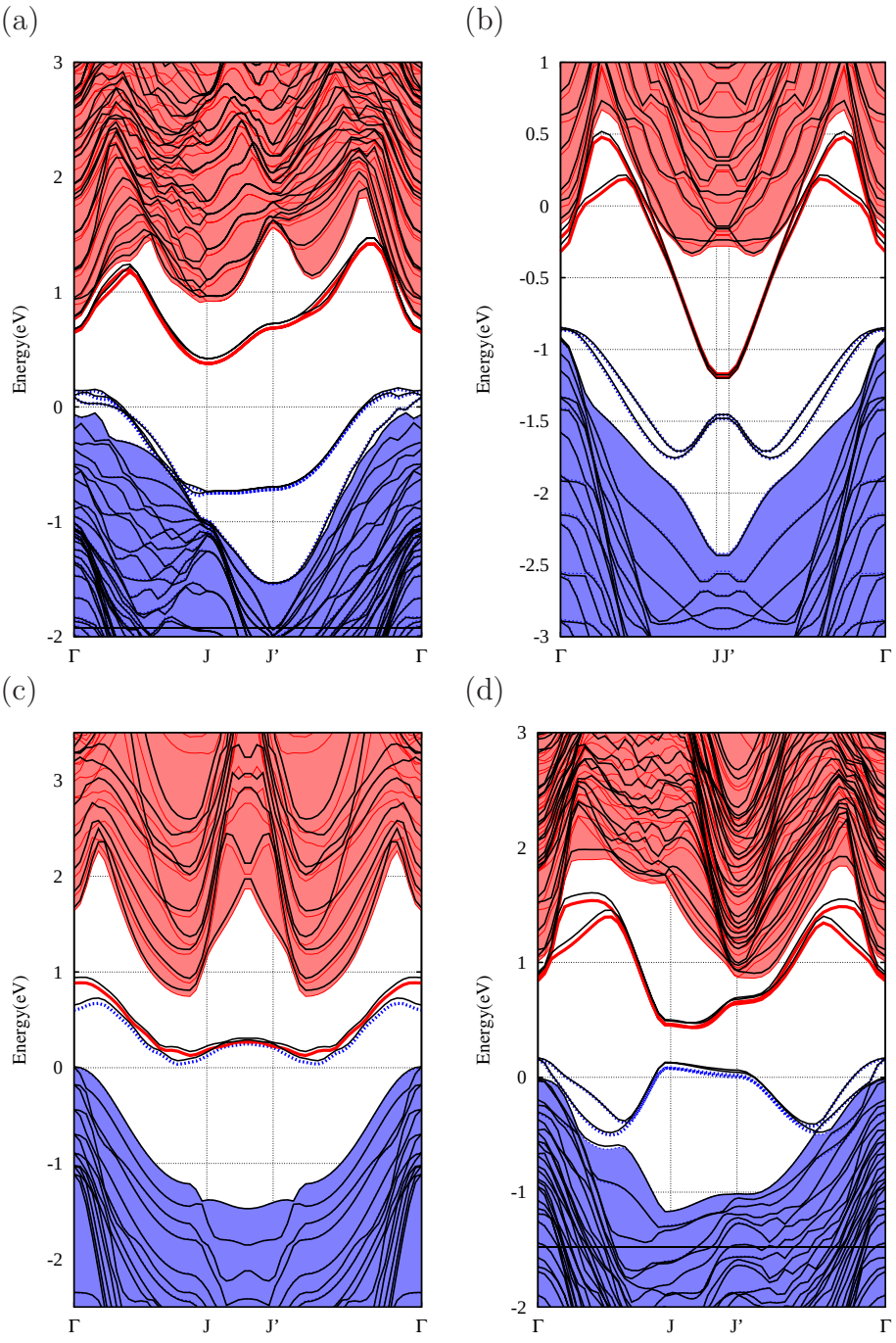

Figure 6.5: Schematic pictures of the clean silicon surface of band structures for (a) (100)-2×1, (b) (110)-1×1, (c) (111)-1×1 ,and (d) (111)-2×1 directions. Blue and red shading crosses indicate filled and empty bands, which calculated by standard method, respectively, while black lines indicate the comparable bands of clean surfaces, which computed by filtration method.

6.6 Electron affinity of diamond

We turn now to a calculation of the electron affinity (EA) of the hydrogenated (111) diamond surface. The MP sampling used was 8×8 for a 1×1 surface cross section of the (111) surface. The surface was modelled using 14 layers of diamond and a 22 Å vacuum region. A H atom is attached to every atom on the diamond surface as shown in figure 6.7. The lattice is a simple-hexagonal(hex-p) supercell.

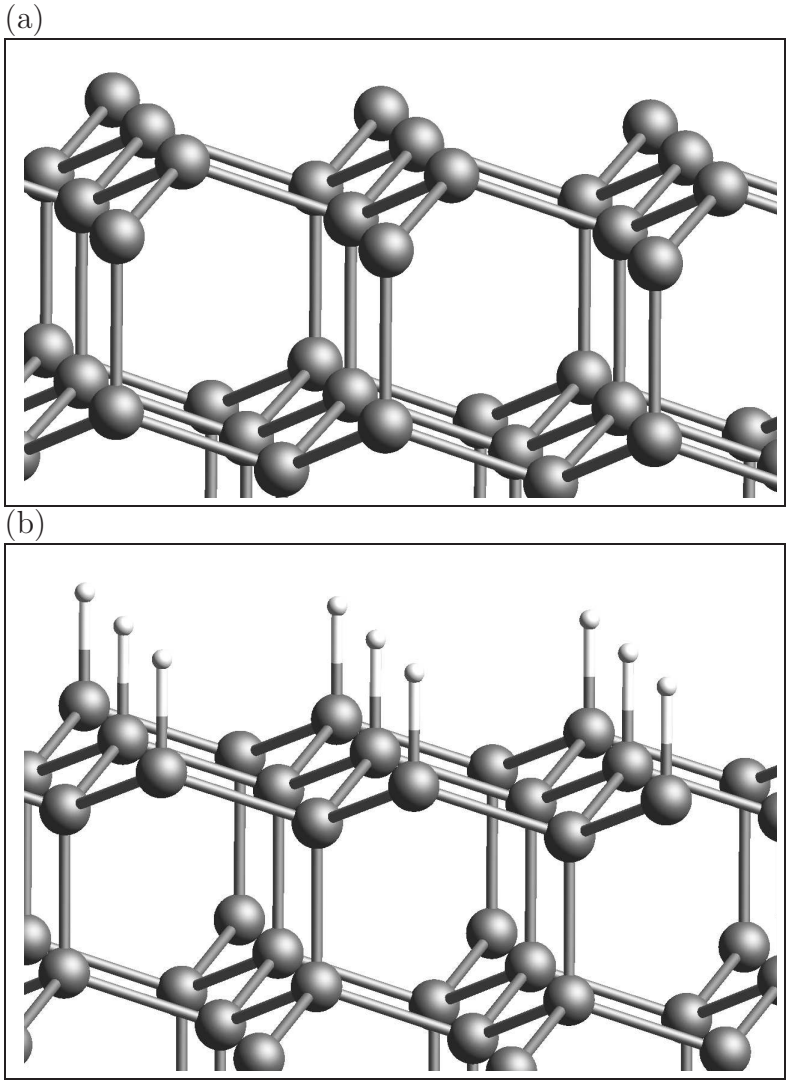

Figure 6.6: Structure of (a) the clean diamond surface, and (b) the 100% H-terminated (111)-1×1 diamond surface.

Table 6.6: Values of electron affinity (eV) of the hydrogenated diamond surface. Experimentally measured values of electron affinity [2–5] are given for comparison with calculated filtered and unfiltered EA values (R_c in a.u.).

Orientation surface	Termination surface	EAs				
		R_c=6	R_c=8	R_c=10	R_c=∞	Exp
(111)-(1×1)GGA	H	-2.30	-2.26	-2.27	-2.28	-1.65
(111)-(1×1)LDA	H	-1.95	-1.94	-1.98	-1.99	
		Absolute error				
Filt *vs* Unfilt	GGA	0.02	0.02	0.01	-	-
Theory *vs* Exp	GGA	0.65	0.61	0.62	0.63	-
Filt *vs* Unfilt	LDA	0.04	0.05	0.01	-	-
Theory *vs* Exp	LDA	0.30	0.29	0.33	0.34	-

The electron affinities were calculated as detailed in section 6.2. Figure 6.7 shows the alignment of the electrostatic potential. The results are listed in table 6.6. During our test, we found that the absolute errors in the EA at R_c=10 a.u. is 0.01 eV in both cases with the GGA and LDA. By comparing our results with the experimental value, we show that these errors are very small in comparison with the error in standard LDA and GGA calculations. The experimental value was taken as an average over many experimental values [2–5]. In addition, figure 6.7 shows the corresponding values of the electrostatic potentials for the (111)-1×1:H diamond surface and bulk diamond, which calculated by filtered and unfiltered basis functions, from the table we can notice the differences in the filtered and unfiltered values of the electrostatic potential of bulk diamond and H-terminated are less than 10 meV in both cases with the LDA functional. Generally, we conclude that the filtration method is suitable for the simulation of electron affinity.

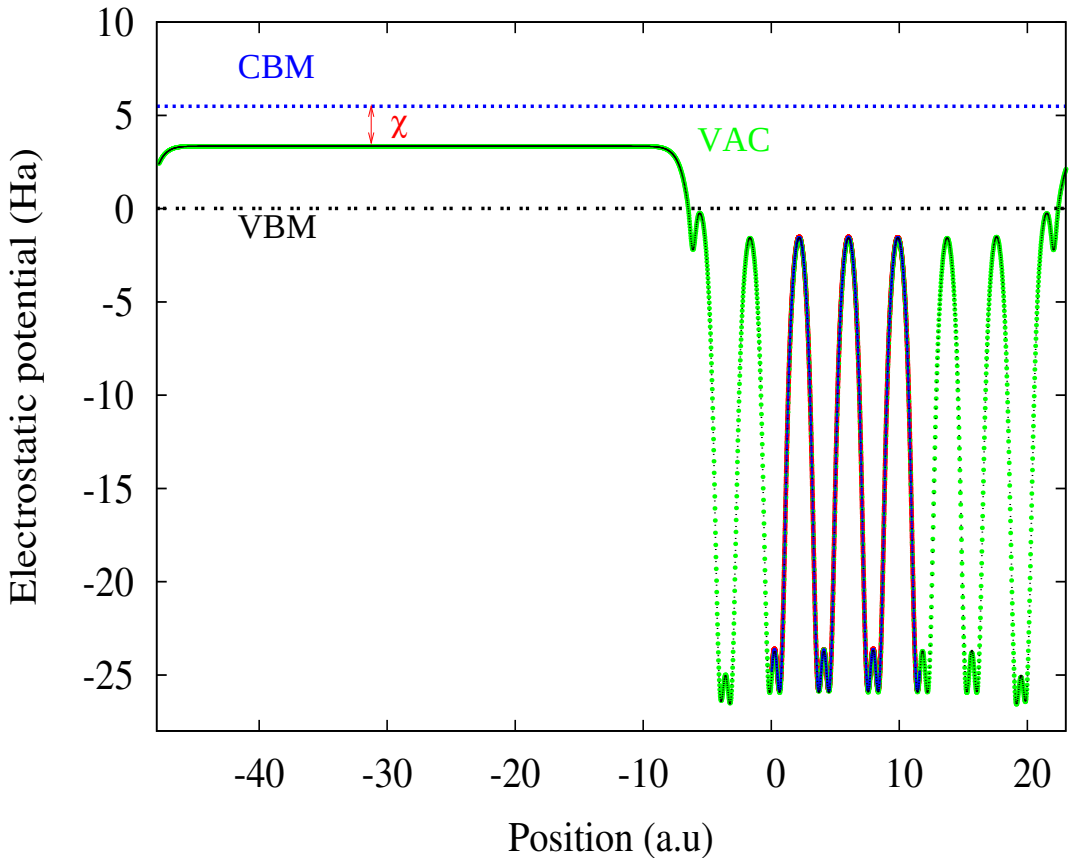

Figure 6.7: Plane-averaged electrostatic potentials for the (111)-1×1:H diamond surface and bulk diamond. The potential of bulk diamond has been aligned with that found in the middle of the slab. The green and black lines are the H-diamond surfaces and the red and blue lines are the bulk diamond for filtered and unfiltered techniques, respectively.

6.7 Conclusions

In summary, we have used a filtration method to calculate the clean surface energies in diamond and silicon and the electron affinity in diamond. The technique is computationally simple and can be used for larger systems. Our method serves as a viable technique for the reliable calculation of clean surface energies and electron affinity the identification of orientation surfaces and hydrogen terminated in bulk and polycrystalline semiconductors.

Chapter 7

Native defects in diamond

7.1 Introduction

This chapter presents a study of the properties of native defects in diamond. Understanding the behaviour of native defects is critical to the successful application of any semiconductor material, especially in compound materials. After testing the filtration technique in the last two chapters on the bulk and on clean diamond and silicon surfaces, leading to a good results, this chapter will provide more evidence of the accuracy of the filtration technique. The properties of crystalline solids and defects therein have great technological importance. The next two chapters will be consider the application to defects in bulk diamond. Native defects can be considered to be defects which contain only the same chemical species as the host material, and form the subject of this chapter. More general defects will be considered in chapter 8.

A study of defects in semiconductors is valuable as many different types of chemical bonding can be present in a defect, and a comparison of the energies of different defects often involves a balance between strain energy (small changes in length for large numbers of bonds) and the energies of broken bonds. As such this could be considered as a quite demanding test of the filtration method, to investigate the accuracy to which such changes can be replicated using 4 functions per atom. The main

goal of the modelling performed here is to compare filtered with unfiltered calculations, to estimate the impact of the filtered basis sets on the accuracy of calculation to calculate the formation, binding and relative energies for the native defects, for example, the single self-interstitial (I_1), di-interstitial(I_2^{NN}), tri-interstitial (O_3) and the tetra-interstitial (I_4). A examining of these structures will give a good test of the filtration method.

7.2 Self-interstitial defects and their aggregates in diamond

As an example testing the accuracy of the filtration method when applied to a real materials problem, a number of native defects composed of aggregates of self-interstitials in diamond will be considered. These calculations have previously been performed using conventional `AIMPRO` calculations [137], and here the results produced using filtered basis sets will be compared to this previous work.

7.2.1 The single interstitial in diamond $I_1^{\langle 001\rangle}$

This defect is the lowest energy structure for a single carbon interstitial atom in diamond [137]. The structure of this can be visualised by removing a host atom and replacing it with two atoms, displaced in [100] and [$\bar{1}$00] directions form the centre of the vacancy created. As described, this defect has D_{2d} symmetry, although subsequent structural relaxations, with reduce this. All runs performed here keep this symmetry and are performed with spin S=0 [137, 138].

7.2.2 Di-interstitial in diamond I_2^{NN}

Three defects will be considered, each of which contains two interstitial C atoms. All three have lower energies than two isolated $\langle 100\rangle$ interstitial defects and this binding energy will be calculated in this work and used to assess the accuracy of the filtration

method as compared with a standard AIMPRO calculation. The binding energy can be found in the following way:

$$E^b = E(I_2) + E[pure] - 2E(I_1) \tag{7.1}$$

where $E[I_2]$ is the energy of a unit cell (say 216 atoms) into which one of the I_2 defects have been placed; $E[I_1]$ is the energy of a unit cell (say 216 atoms) into which the S=0 I_1 (100) defect has been placed and $E[pure]$ is the energy of a 216 atom unit cell containing carbon atoms in the perfect diamond structure. The three energies differ greatly as they correspond to different numbers of atoms, however the difference given in equation 7.1 only describes the binding energy of the complex, associated with the chemical bonding changes as the defect is formed. The effect of moving from a conventional calculation to a filtered calculation may result in the energies $E[I_2]$,$E[I_1]$ and $E[pure]$ changing significantly (by many eV). However, it is important that the binding energy E^b should be well converged (to less than 0.1 eV) if the filtration method is considered to be successful.

The R_1 defect

This defect can be constructed by inserting two $\langle 100 \rangle$ interstitials on neighbouring atom sites in diamond. Two bonds form between these as seen in figure 7.1 in which there are only two three-fold co-ordinated atoms. This results in the combined defect having two dangling bonds, as compared with four for two isolated $\langle 100 \rangle$ defects. As such this defect has a lower energy than two isolated $\langle 100 \rangle$ centres.

The Humble defect

This defect can be constructed by inserting two $\langle 100 \rangle$ interstitials on second neighbour atom sites in diamond. One bond forms between these as seen in figure 7.1 it is seen from this that there are again only two three-fold co-ordinated atoms. This defect again has a lower energy than two isolated $\langle 100 \rangle$ centres.

The π-bonded defect

The π-bonded structure is formed by inserting two C atoms near the centres of two C-C bonds which are on opposite sides of a hexagon in the diamond structure as shown in figure 7.1. It has previously been reported that this has a lower energy than either the R1 or Humble structures [137,138], because a double (π) bond forms between the interstitial atoms with the result that there are no dangling bonds at all.

7.2.3 Large-interstitial defects in diamond I_3 and I_4

The binding and formation energies will be calculated in this work and used to assess the accuracy of the filtration method as compared with a standard `AIMPRO` calculation. The binding energy can be found from the formation energy as the difference in the formation energy of an aggregate I_n of n interstitials and $nE_f(I_1)$, as shown in the following equation:

$$E^b = nE^f(I_1) - E^f(I_n) \tag{7.2}$$

the formation energy can be calculated as in equation 4.7 in chapter 4.

The I_3 defect

The I_3 defect can be constructed by inserting three $\langle 100 \rangle$ interstitials on second and third neighbour atom sites in diamond. One bond forms between these, it is seen from this that there are again only two three-fold co-ordinated atoms. The structure is in Ref. [137].

The I_4 defect

The structure of the I_4 defect has suggested from the I_3 tri-interstitial structure. One further [001] split interstitial has been added to I_3 structure, by inserting a further C atom.

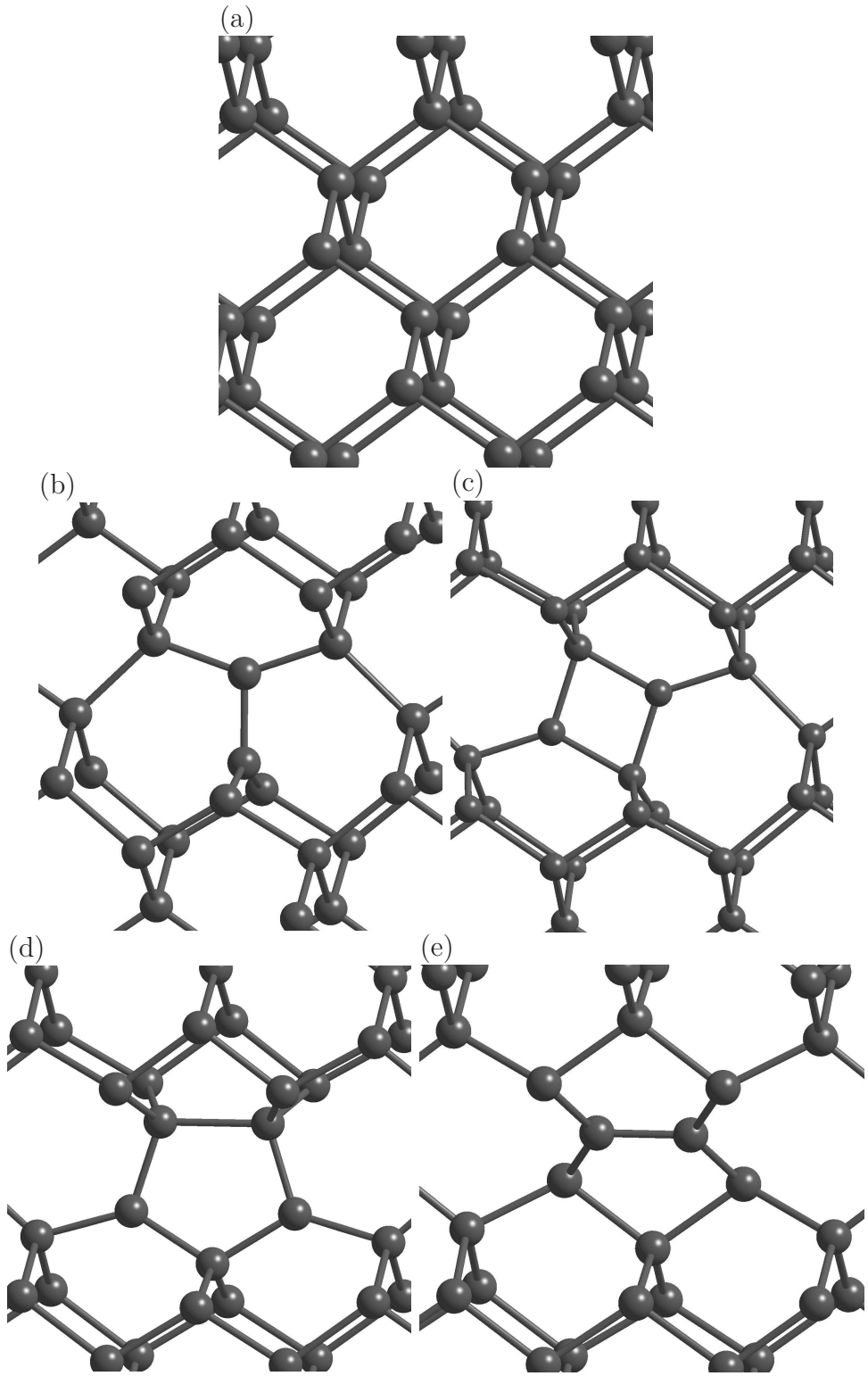

Figure 7.1: Schematic pictures of models of diamond interstitial models viewed along a direction close to [110] for (b) R2,(c) R1,(d) Humble, and (e) $\pi - bonded$ models. A section of pure diamond is shown for comparison in (a).

7.2.4 Method of calculation

Our calculations have been performed in the local density approximation (LDA) using the `AIMPRO` code. The pseudopotentials are Hartwigsen, Goedecker, and Hutter [51]. The modelling of the interstitial defects is done by inserting the suitable number of additional carbon atoms in the supercell. By using the conjugate gradient algorithm, the atoms are moved to their optimal positions. The sampling used in our results was carried out using a MP(2 2 2) [60] set of k-points in the Brillouin zone. The standard basis set (*ddpp*) containing 28 function per atom will be reduced to 4 functions per atom in the filtered basis set. Each supercell included $(216+n)$ atoms of carbon. The next section discusses six relevant defects, the (100) interstitial and three complexes in which two of these defects have aggregated.

7.3 Relative energy

The relative total energies of the interstitial pairs relative to the lowest energy π-bonded structure have been determined as a function of the basis and functional, with the results listed in Table 7.1, R_c=∞ is used as shorthand for an unfiltered calculation.

Table 7.1: Total energies (eV) of Humble and R1 structures relative to the most stable, π-bonded structure (eV) as defined in the text for the neutral charge state. The energies are quoted to three decimal places to allow for comparison.

Defect	R_c			
	6	7	8	∞
Humble	1.053	1.122	1.103	1.125
R1	2.011	2.101	2.088	2.090

There is clearly no significant impact upon the relative energies due to the filtration, with differences typically of the order of 10 meV, and less than 1% of the relative energy values. Indeed the impact of filtration is smaller than that arising from other factors in the calculation. Our filtered results therefore show the reliability of the filtration method in this calculation.

7.4 Binding energy

The relative energies found in the previous section can be presented in terms of binding energies found using equation 7.2. The resulting values are given in table 7.2. It is seen that the differences between binding energies evaluated with cut-off R_c=8 a.u.

Table 7.2: Binding energies relative to single interstitials (eV) as defined in the text for the neutral charge state, R_c in a.u.

Defect	E^b	R_c			
		6	7	8	∞
R1(I_2)	per defect	6.28	6.30	6.28	6.28
	per interstitial	3.14	3.15	3.14	3.14
π-bonded	per defect	8.30	8.40	8.36	8.36
	per interstitial	4.15	4.20	4.18	4.18
Humble(I_2)	pre defect	7.24	7.28	7.28	7.26
	per interstitial	3.62	3.64	3.64	3.63
(I_3)	per defect	10.10	10.22	10.16	10.16
	per interstitial	5.05	5.11	5.08	5.08
(I_4)	per defect	13.62	13.70	13.66	13.64
	per interstitial	6.81	6.85	6.83	6.82

and unfiltered calculations is less than 10 meV and that even a very small cutoff radius of R_c=6 a.u. introduces errors of only 30 meV per interstitial. Clearly the

filtered calculations are entirely reliable for this type of calculation. It should be noted that the unfiltered results in table 7.2 differs very slightly from previous published work [137]. This is a consequence of smaller cells used in the earlier calculations.

7.5 Formation energy

Finally, we present the energies of the different defects as formation energies relative to the energy of atoms in bulk diamond. The formation energy of course is a factor controlling the concentration of the defect in thermal equilibrium and is a slightly different test of the calculation as the energy of a unit cell containing a defect is being compared with a bulk unit cell (there is less cancellation of energies between defects

Table 7.3: Formation energies relative to bulk diamond (eV) as defined in the text for interstitial defects in the neutral charge state, R_c in a.u.

Defect	E^f	R_c			
		6	7	8	∞
R2(I_1)	per interstitial	12.23	12.17	12.16	12.15
R1(I_2)	per defect	18.18	18.04	18.04	18.01
	per interstitial	9.09	9.02	9.02	9.00
π-bonded	per defect	16.17	15.94	15.95	15.92
	per interstitial	8.08	7.97	7.97	7.96
Humble (I_2)	per defect	17.22	17.06	17.05	17.03
	per interstitial	8.61	8.53	8.52	8.51
(I_3)	per defect	21.53	21.17	21.22	21.18
	per interstitial	7.17	7.06	7.07	7.06
(I_4)	per defect	21.65	21.28	21.30	21.26
	per interstitial	5.41	5.32	5.32	5.31

containing dangling bonds as there is in binding energies). The resulting formation energies are given in table 7.3. It is seen that the maximum difference in formation energy calculated with cut-off radius R_c=8 a.u. is 20 meV per interstitial (in values which are typically 7 eV), an error which is very small on the scale of charges that may be expected to occur if other ingredients of the calculations were changed (for example, the difference between the LDA formation energy and diffusion Monte-Carlo calculated value for a vacancy in diamond is 1 eV). There is again an insensitivity to the variation of cut-off radius - the results with R_c=6 a.u. are noticeably inferior, with errors being of order 100 meV per interstitial, but this is still small in comparison to the quantity being considered. In conclusion, these results suggest that total energies of defects obtained using the filtration approach are of sufficient quality to replace standard calculations containing nearly 10 times as many basis functions.

7.6 Band structure

We now turn our calculation to the band structure of the supercells containing the interstitial defects discussed above. The band structure was calculated in the vicinity of the band gap along high-symmetry directions. The values of the valence band maximum (VBM), the defect band (DB) and the conduction band minimum (CBM) are given in tables 7.4, 7.5 and 7.6 for the six defects considered previously.

Figures 7.2 and 7.3 give a graphical representation of a large energy range of the band structures. These figures show that the KS energies are visually unchanged by filtration, from the tables, we can see that the maximum difference in all band cases between R_c=10 a.u and R_c= ∞ is around 0.03 eV. Throughout these results, we found that the positions of the Kohn-Sham levels was only very slightly changed in all defect cases, and both techniques, filtered and unfiltered have given very similar results, this seems clear through the matching of the bands lines, as shown in the figures 7.2 and 7.3. The computational findings in this study have provided a new confirmation on the accuracy of the filtration method.

Table 7.4: Band structure energies in eV at four high symmetry k-points Γ, X, M, and R for the R2 and R1 centres in diamond, LDA functional as a function of (R_c in a.u). The energies are given for the highest valence band state (VB), the defect bands (DB) and the lowest an occupied state (CB).

Structure	K-points	level	R_c			
			6	8	10	∞
R2	Γ	VB	0.000	0.000	0.000	0.000
		DB	1.972	1.972	1.955	1.942
		DB	1.972	1.972	1.955	1.942
		CB	4.172	4.173	4.149	4.133
	X	VB	-0.512	-0.514	-0.512	-0.515
		DB	2.065	2.064	2.048	2.036
		DB	2.065	2.064	2.058	2.036
		CB	4.210	4.213	4.196	4.182
	M	VB	-0.276	-0.279	-0.287	-0.279
		DB	2.014	2.014	1.997	1.985
		DB	2.068	2.068	2.053	2.040
		CB	5.168	5.168	5.156	5.136
	R	VB	-0.949	-0.953	-0.955	-0.956
		DB	2.021	2.020	2.005	1.992
		DB	2.021	2.020	2.005	1.992
		CB	5.136	5.128	5.115	5.096
R1	Γ	VB	0.000	0.000	0.000	0.000
		DB	1.505	1.509	1.492	1.480
		DB	1.969	1.973	1.954	1.940
		CB	4.122	4.122	4.100	4.083
	X	VB	-0.419	-0.419	-0.419	-0.421
		DB	1.622	1.627	1.611	1.600
		DB	2.022	2.025	2.007	1.993
		CB	4.154	4.156	4.140	4.126
	M	VB	-0.246	-0.248	-0.248	-0.249
		DB	1.602	1.607	1.591	1.581
		DB	1.996	1.999	1.979	1.966
		CB	5.086	5.086	5.072	5.055
	R	VB	-0.774	-0.772	-0.776	-0.786
		DB	1.585	1.589	1.574	1.563
		DB	1.970	1.973	1.954	1.940
		CB	5.065	5.087	5.045	5.026

Table 7.5: Band structure energies in eV at four high symmetry k-points Γ, X, M, and R for the π-bonded and Humble centres in diamond, LDA functional as a function of (R_c in a.u). The energies are given for the highest valence band state (VB), the defect bands (DB) and the lowest an occupied state (CB).

Structure	K-points	level	R_c			
			6	8	10	∞
π-bonded	Γ	VB	0.000	0.000	0.000	0.000
		DB	.0394	0.411	0.399	0.392
		CB	4.163	4.163	4.140	4.124
	X	VB	-0.506	-0.508	-0.5081	-0.509
		DB	0.451	0.468	0.456	0.449
		CB	4.261	4.262	4.246	4.232
	M	VB	-0.238	-0.242	-0.242	-0.242
		DB	0.463	0.479	0.468	0.462
		CB	4.479	4.476	4.464	4.443
	R	VB	-0.837	-0.838	-0.841	-0.842
		DB	0.424	0.440	0.429	0.422
		CB	4.353	4.348	4.336	4.315
Humble	Γ	VB	0.000	0.000	0.000	0.000
		DB	1.554	1.558	1.543	1.531
		DB	2.499	2.492	2.474	2.461
		CB	4.014	4.016	3.994	3.977
	X	VB	-0.535	-0.534	-0.536	-0.538
		DB	1.596	1.601	1.586	1.574
		DB	2.547	2.538	2.522	2.508
		CB	4.342	4.344	4.323	4.307
	M	VB	-0.261	-0.263	-0.264	-0.264
		DB	1.616	1.620	1.605	1.594
		DB	2.584	2.575	2.561	2.548
		CB	4.886	4.887	4.869	4.852
	R	VB	-0.848	-0.843	-0.849	-0.851
		DB	1.596	1.600	1.585	1.574
		DB	2.565	2.555	2.541	2.528
		CB	4.789	4.785	4.777	4.748

Table 7.6: Band structure energies in eV at four high symmetry k-points Γ, X, M, and R for the I_3 and I_4 defects in diamond, LDA functional as a function of (R_c in a.u). The energies are given for the highest valence band state (VB), the defect bands (DB) and the lowest an occupied state (CB).

Structure	K-points	level	R_c			
			6	8	10	∞
I_3	Γ	VB	0.000	0.000	0.000	0.000
		DB	0.266	0.266	0.266	0.266
		CB	4.137	4.139	4.107	4.099
	X	VB	-0.442	-0.443	-0.445	-0.447
		DB	-0.143	-0.145	-0.144	-0.147
		CB	4.133	4.133	4.117	4.101
	M	VB	-0.127	-0.130	-0.131	-0.132
		DB	-0.002	-0.004	-0.005	-0.006
		CB	4.770	4.766	4.751	4.732
	R	VB	-0.730	-0.733	-0.736	-0.738
		DB	-0.609	-0.611	-0.608	-0.616
		CB	4.662	4.655	4.644	4.620
I_4	Γ	VB	0.000	0.000	0.000	0.000
		DB	0.344	0.344	0.344	0.343
		CB	4.088	4.091	4.070	4.052
	X	VB	-0.447	-0.448	-0.450	-0.452
		DB	0.006	0.014	0.007	0.006
		CB	4.601	4.601	4.582	4.566
	M	VB	-0.255	-0.258	-0.258	-0.258
		DB	-0.058	-0.048	-0.056	-0.057
		CB	4.675	4.678	4.663	4.642
	R	VB	-0.584	-0.583	-0.587	-0.589
		DB	-0.354	-0.340	-0.351	-0.352
		CB	4.641	4.638	4.622	4.604

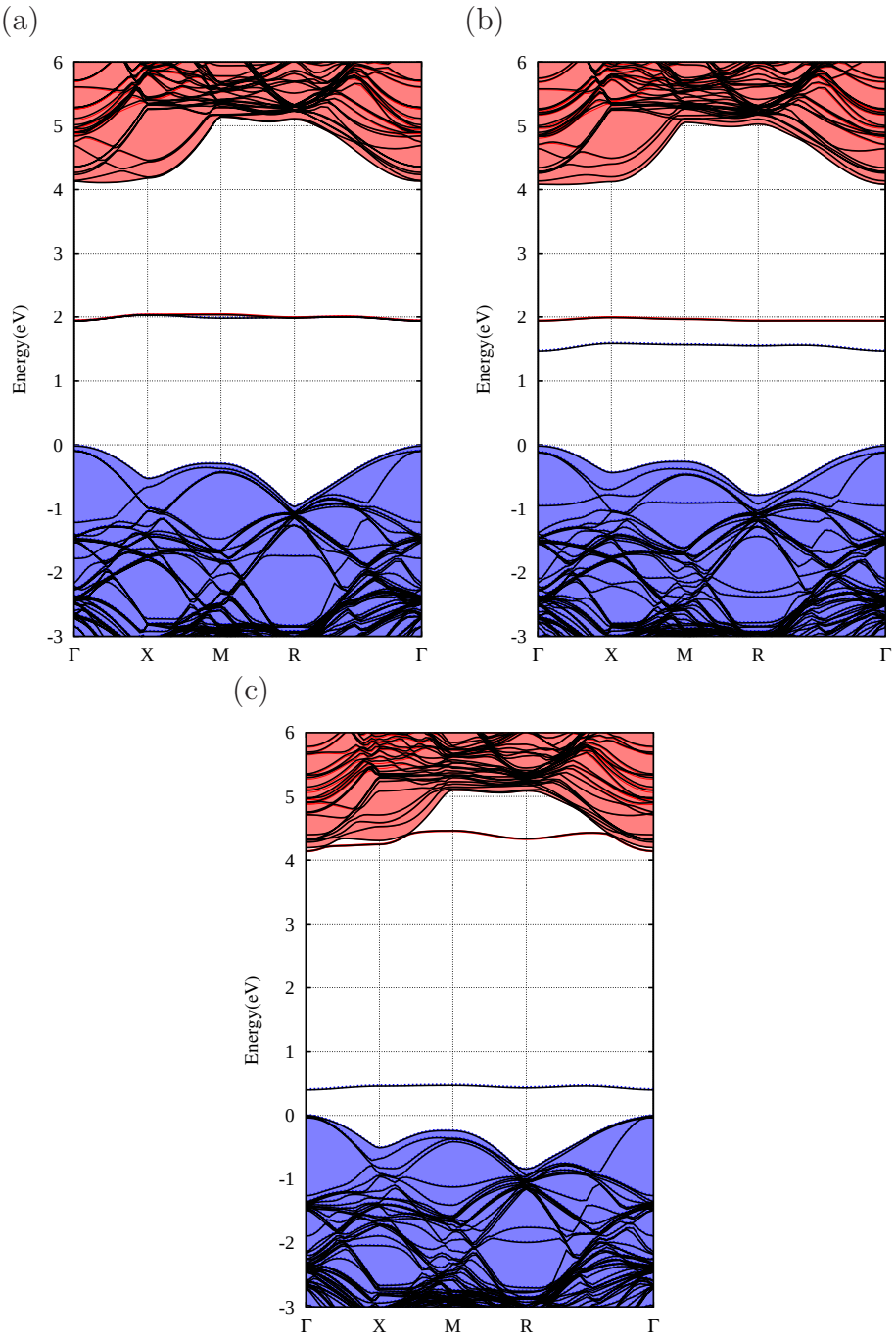

Figure 7.2: Band structures for 216 atom supercells containing the (a) R2, (b)R1, (c) π-bonded. Blue and red crosses indicate filled and empty bands respectively calculated by standard `Aimpro` method, while black lines indicate the comparable bands computed by the filtration method (R_c=8 a.u). Quantitative values are given in tables 7.4 and 7.5 for R1, R2, and π-bonded centres.

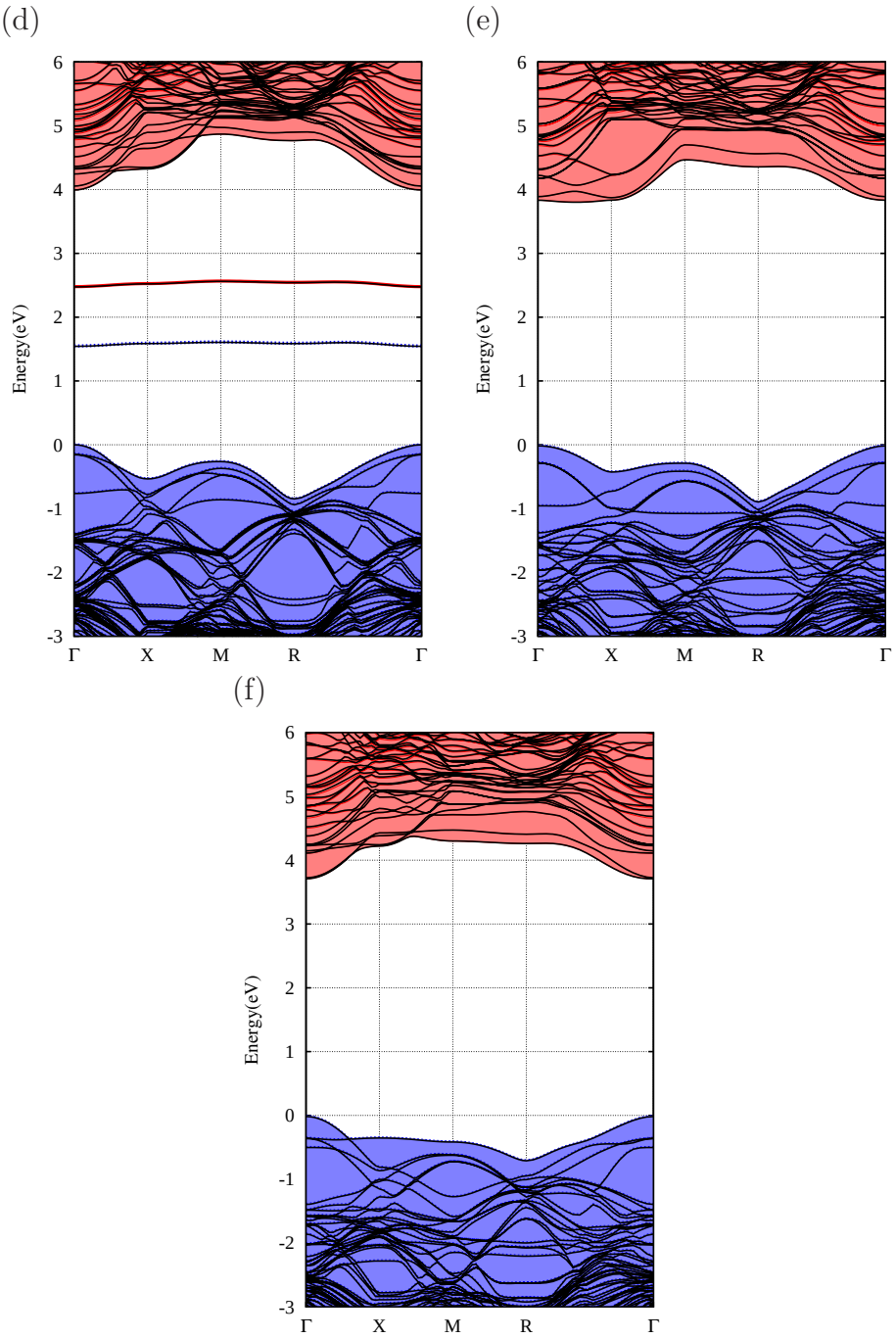

Figure 7.3: Band structures for 216 atom supercells containing the (d) Humble, (e) I_3 defect, and (f) I_4 defect. Blue and red crosses indicate filled and empty bands respectively calculated by standard `Aimpro` method, while black lines indicate the comparable bands computed by the filtration method (R_c=8 a.u). Quantitative values are given in tables 7.5 and 7.6 for Humble, I_3, and I_4 defects.

7.7 Conclusion

The results presented in this chapter show that filtered basis calculation employing just 4 basis functions per atom are able to reproduce the conventional calculations of the relative energies between a number of interstitial defect complexes to within 10 meV or so. This is true for binding energies and formation energies. This shows that the previously reported conclusions given for defects in silicon [33] are also valid in diamond. The ability to calculate accurate formation energies is clearly vital for filtration to be used as a mainstream technique, and these results show that the delicate balances between the strain energy and the energy of dangling bonds that gives rise to the varying stabilities of these defect centres is reproduced to a very good degree in these calculations. Results given in this chapter also show for the first time that the band structures are reproduced to within 10-30 meV for appropriate and convenient choices of cut-off radius, at least for the important states in the valence band and near the band gap.

Chapter 8

Impurities in diamond

8.1 Introduction

A common type of defect in solids is the point defect. These defects can be native defects as considered in the previous chapter or extrinsic defects which involve atoms of another chemical species. An understanding of these is important technologically as they can be introduced deliberately (for example as dopants) or unintentionally during growth or processing. They are also present naturally, for example nitrogen in diamond. In this chapter, we will look at a number of these defects in diamond using them as a basis for assessing the accuracy of the basis set filtration approach. Many theoretical, computational modelling and experimental researches have focused on the common impurities in diamond such as nitrogen, boron and hydrogen [139]. However, the classification of diamonds is based on to the number and structure of the nitrogen impurities in diamond. This classification will be presented in the next section.

8.2 Classification of diamond

The impurities in natural diamond play a significant role in the classification of diamond as they play the main role in determining the colour of diamond. Nitrogen is

by far the most common impurity in diamond, therefore, the primary classification of diamond is relative to its nitrogen contact.

■Type I diamond contains significant quantities of nitrogen. Type I diamond has been further divided into two types “Ia and Ib ”, which depends on the nature of the nitrogen atoms in the material whether are isolated or combined.

□Type (Ia)

Most natural diamonds are of type Ia and can contain up to 3000 ppm of nitrogen [140]. Type Ia diamond is further divided into type IaA in which the N atoms are predominantly incorporated as defects known as A centres which contain two substitutional N atoms on adjacent suites and type IaB diamonds in which 4 N atoms occupy substitutional sites which surround a vacancy, a defect known as the B centre.

□Type (Ib)

This type of diamond contains isolated nitrogen atoms which are known as C centres or in EPR experiments these are known as P1 centres, the appearance of this type in natural diamond is less than 0.1%, but is more common in a synthetic diamond. Diamonds in this class possess a slight yellow colour. The material of the type Ib can be changed to type Ia, if subjected to a high temperature and pressure.

■The second type of diamond (II) has been labelled into two types “IIa and IIb”,

□Type (IIa)

The percentage of concentration nitrogen in natural type (IIa) diamonds is less than 1-2 ppm [141] and is undetectable by optical spectroscopy, particularly in the single phonon region. These diamonds are therefore colourless.

□Type (IIb)

This type of diamond contains B atoms, which give it a blue colour. This type of impurity could produce p-type semiconductors, and appears rarely in natural diamond.

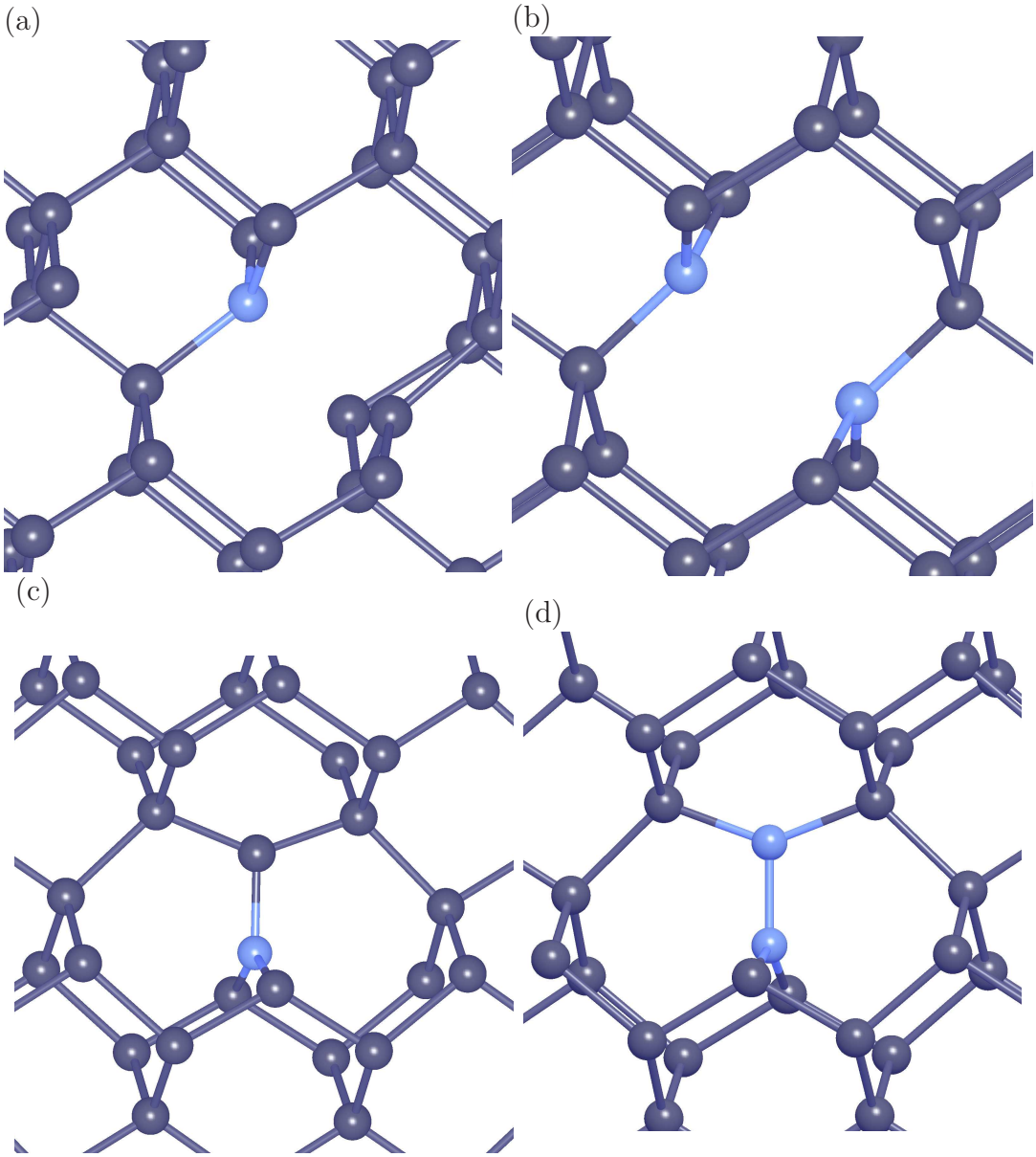

Figure 8.1: Schematic diagram showing the geometry of (a) the Ns (P1), (b) the N_{2s} (c) the N_i and (d) the N_{2i} ($H1$a) centres. Substitutional and interstitial nitrogen atoms are showing a blue colour, with the three-and four-fold coordinated carbon atoms being gray, respectively. Horizontal and vertical directions are approximately [110] and [001], respectively.

8.3 Computational Method

All the calculations are performed using the local-spin-density functional theory implemented in the `AIMPRO` [12, 16] *ab initio* modelling package, using two modelling techniques. Exchange-correlation is addressed using the generalized gradient approximation (GGA) [105] as developed by Perdew, Burke and Ernzehof. We use a k-point sampling grid $2 \times 2 \times 2$ [60]. With a cutoff of 350 Ry, the charge density is Fourier transformed and plane waves used to determine the Hartree potential. Two types of pseudo-wave-functions basis have been used to address the system, the first type is a filtered basis function which consists of an admixture of sets of Gaussian orbitals centered at each atomic site, with total of 4 filtered functions on each atom [33, 104]. The second type is an unfiltered independent basis set which contains s, p and d Gaussian orbitals [52], with a total of 28 functions centred on each atom, with two sets of d functions added to allow for polarization. The elimination of the core electrons is achieved using norm-conserving pseudopotentials [51]. Unless otherwise stated structures have been optimised by relaxing all atoms in supercells comprised from 64 or 216 host sites (simple-cubic lattice with lattice vectors of length $2a_0$ or $3a_0$). By using the conjugate gradient algorithm, the atoms are moved to their optimal positions until the total energy changes by less than 10^{-4} a.u, and the atoms must be relaxed until the forces between them have converged. The lattice constant and bulk modulus of bulk diamond are as shown in chapter 5. The calculations of the direct and indirect band gaps are in agreement with the previous calculated plane-wave values [142]. The local vibration modes [143] have been computed by finding the second derivatives of the total energy with regard to the atoms position from the equilibrium sites, followed by the construction of the dynamical matrix which is then diagonalised. The electrical levels [144] for the P1 centre have been examined using the formation energy method (FEM), and is discussed fully in Ref [145] and chapter 4, (0/+) and (-/0) levels represent the donor and acceptor levels, respectively. The electrical level of the defect is represented by the electron chemical potential, at which the two charged states concerned have the same formation energy. The following definition has been

used to address the formation energy of the neutral system (X),

$$E^f(X) = E(X) - \sum_i^{atom} \mu_i \tag{8.1}$$

where $E(X)$ is the total energy of a unit cell containing the defect (X) and μ_i are the chemical potentials of the atomic species present. The energy of a state (0/+) or (-/0) is the Fermi energy at which the two charge states have the same total energy. The ionisation energy has been calculated relative to the valence band maximum energy of the diamond (VBM) is given by,

$$\varepsilon = E^0_{tot} - E^+_{tot} - E_{VBM} \tag{8.2}$$

where $E^{0,+}_{tot}(X)$ is the total energy.

To confirm the accuracy of the computational technique (filtration method) the optical properties, such as the hyperfine interaction of some impurities in diamond configurations have been tested. Hyperfine-interactions are modelled as outlined previously [48]. The wave functions are expanded in atom centred Gaussian unfiltered basis functions with 28 functions for C, 40 functions for each N, Si, and S, and 16 functions for H atoms respectively. They are also are expanded by using filtered basis functions with 4 functions for each atom.

8.4 Nitrogen containing defects

As previously explained, there are a number of well-known nitrogen-containing defects in diamond, and in this section we first assess the filtration algorithm in relation to these. A selection of these is illustrated in figure 8.1. First the isolated substitutional nitrogen atom N_s, referred to as the P1 centre or C centre is modelled by replacing a single C atom by a N atom. In this case, it is well known that one of the four NC bonds breaks, giving a defect of C_{3v} symmetry. The A centre consists of two adjacent substitutional N atoms (referred to as N_{2s} in this section). In this case the NN distance lengthens as shown in figure 8.1, this time giving a defect of symmetry

D_{3d}. A possible structure of interstitial nitrogen denoted N_i is created in a unit cell by replacing one of the 2 C atoms in an R2 centre (previous chapter) with a N atom (symmetry C_{2v}). Finally, the H1a centre contains two N atoms, and is created by replacing both C atoms in an R2 centre with N. Here this defect is referred to as N_{2i} (symmetry D_{2d}).

8.4.1 The local vibrational modes

To test the accuracy of our calculations, which have been carried out using the filtration algorithm technique within the `AIMPRO` code, we first calculated the frequency of atomic vibrations ω (cm^{-1}) of the substitutional P1 and H1a centres in the neutral charge state [72, 73]. The models for the neutral state of these defects have C_{3v} and D_{2d} symmetry, respectively. Our results have been obtained performed by using supercells containing 63-host carbon atoms, the resulting highest frequency modes are shown in table 8.1. The structures have been relaxed twice, once with the full unfiltered basis (28 functions per atom) and once with the filtered basis (4 functions per atom). It is seen that the percentage change in result incurred by filtration, even with a filtration radius of 6 a.u are just 0.26%, reducing to 0.049% with a cutoff radius of 10 a.u. This is much smaller than the percentage difference between theory and experiment (typically about 1%) showing that the filtration process has not had a significant impact upon the accuracy of calculations. All phonon frequencies for all supercells are underestimated compared with the measured value by 1-3%, a consequence of the GGA being used.

8.4.2 Binding energy

We have checked the accuracy of the binding energies of defects using the two different basis sets described 8.3. First, the binding energy of N_{2i} was found relative to the isolated N atom, N_s, and a nitrogen interstitial, N_i:

$$N_s + N_i \rightarrow N_{2i} \tag{8.3}$$

Table 8.1: A comparison between the high frequency vibrational modes ω in cm^{-1} calculated in filtered and unfiltered basis set calculations, (R_c is in a.u).

Defect	R_c				
	6	8	10	∞	Exp
P1	1319.97	1320.13	1318.25	1317.60	1344
H1a	1830.96	1822.27	1818.40	1811.05	-
	1438.39	1440.32	1436.20	1433.24	1450
	1438.39	1440.32	1436.20	1433.24	1450
Abs-errors (cm^{-1})					
P1(Filt *vs* Unfilt)	2.37	2.53	0.65	-	-
P1(Theory *vs* Exp)	24.03	23.87	25.75	26.4	-
H1a(Filt *vs* Unfilt)	5.15	7.08	2.96	-	-
H1a(Theory *vs* Exp)	11.61	9.68	13.80	16.76	-
Per-errors					
P1(Filt *vs* Unfilt)	0.26%	0.19%	0.049%	-	-
P1(Theory *vs* Exp)	1.78%	1.77%	1.91%	1.96%	-
H1a(Filt *vs* Unfilt)	0.36%	0.49%	0.21%	-	-
H1a(Theory *vs* Exp)	0.80%	0.66%	1.13%	1.15%	-

which is found using according to the equation

$$E^b = E[\mathrm{N}_{2i}] + E[\mathrm{pure}] - E[\mathrm{N}_s] - E[\mathrm{N}_i] \tag{8.4}$$

where $E[X]$ is the total energy of a unit cell containing defect X, and E[pure] is the energy of a unit cell without a defect present. A second reaction was also considered:

$$\mathrm{C}_i + \mathrm{N}_{2s} \rightarrow \mathrm{N}_{2i} \tag{8.5}$$

Table 8.2: The table compares the binding energies of N_{2i} found according to equations 8.4 and 8.6 in the text. They have been calculated using two techniques, using a filtered basis (R_c=6, 8, and 10 a.u), and an unfiltered basis (R_c=∞).

Defect	R_c			
	6	8	10	∞
Equation 8.4	5.096	5.116	5.113	5.105
Equation 8.6	7.105	7.167	7.118	7.100

in which the binding energy of N_{2i} is found relative to an A center, N_{2s}, and an R2 centre according to

$$E^b = E[\mathrm{N}_{2i}] + E[\mathrm{pure}] - E[\mathrm{R2}] - E[\mathrm{N}_{2s}] \tag{8.6}$$

These binding energies are shown in table 8.2. The results show that there is no significant impact on the values caused by filtration, the differences between the binding energies shift by only 0.01 eV or so relative to R_c=∞ indicating a satisfactory performance of the filtration algorithm.

8.4.3 Electronic structure

As a different test of the filtration method, we calculated the ionisation energies of the single substitutional N_s donor. It is known experimentally that the donor level of this defect is at E_c-1.7 eV [146]. Table 8.3 shows both filtered (R_c=6, 8, and 10 a.u) and unfiltered (R_c=∞) results, which are very close to each other. Figure 8.2 presents the variation of the formation energy as a function of the electron chemical potential. This plot allows estimation of the energy levels given in table 8.3. The difference between filtered and unfiltered calculations at R_c=6 a.u and R_c=∞ is 0.07 eV and

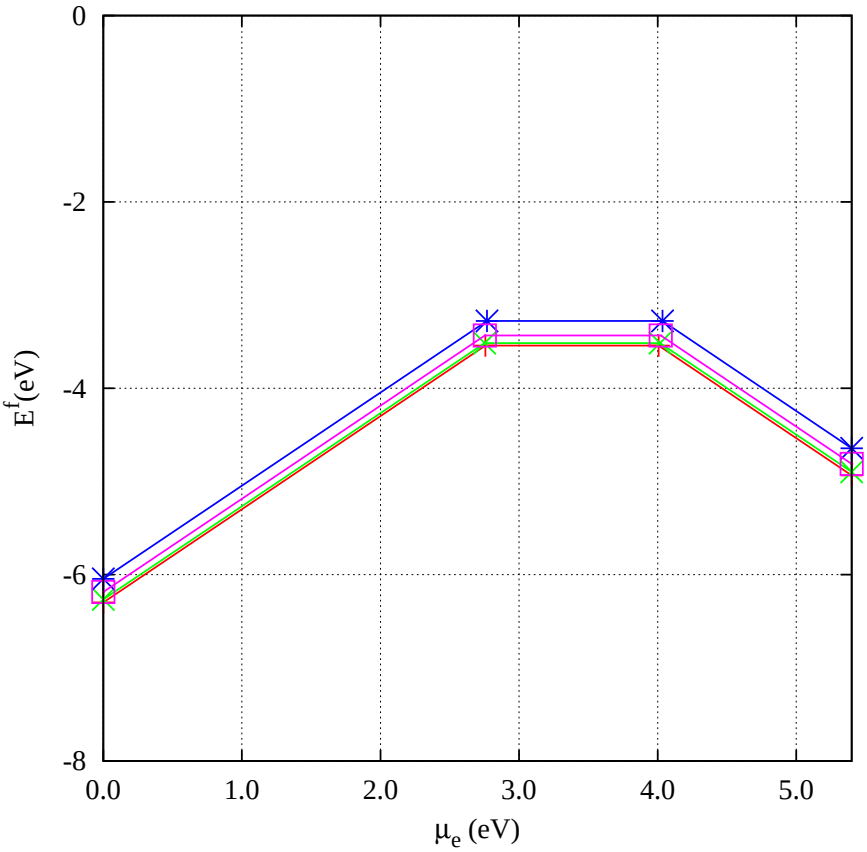

Figure 8.2: Plot of formation energy E^f *vs.* electron chemical potential μ_e for the N defect in diamond. The energy is calculated using the 64 atom supercell: R_c=6 (∗), R_c=8(□),R_c=10(x), R_c=∞ (+).

between R_c=10 a.u and R_c= ∞ less than 0.01 eV. For comparison, the difference with the experimental result is 0.27 eV for the (0/+) level. The results in table 8.3 therefore show that, the computational filtered basis set has given a good agreement with the standard and the experimental calculations.

8.4.4 Band structure

Turning now to the Kohn-Sham band structure, we present results for the P1 and $H1a$ centres in diamond in the vicinity of the band gap along high-symmetry directions

Table 8.3: The table compares the ionization energies of the substitutional nitrogen donor, which have been found using two techniques, (R_c in a.u).

Defect	R_c			
	6	8	10	∞
$E_{(0/+)}(eV)$	E_v+2.78	E_v+2.76	E_v+2.75	E_v+2.76
$E_{(-/0)}(eV)$	E_v+4.08	E_v+4.05	E_v+4.04	E_v+4.01
		Abs-errors		
Filt *vs* Unfilt($E_{(0/+)}$)	0.02	0.00	0.01	-
Filt *vs* Unfilt($E_{(-/0)}$)	0.07	0.04	0.03	-
		Per-errors		
Filt *vs* Unfilt($E_{(0/+)}$)	0.72%	0.00%	0.36%	-
Filt *vs* Unfilt($E_{(-/0)}$)	1.74%	0.99%	0.74%	-

in figure 8.3. These are obtained from cells of 215 carbon atoms. Throughout these results, we found that, the filtration modelling technique has kept the accuracy of the calculation of the band structure largely unaffected over the valence band and for some way into the CB. The maximum errors in Kohn-Sham band structure energies for the P1 centre are 0.052 eV (R_c=6 a.u), 0.021 eV (R_c=8 a.u) and 0.011 eV (R_c=10 a.u). For the $H1$a centre the values show a similar pattern: R_c=6 a.u is 0.099 eV, R_c=8 a.u is 0.038 eV and R_c=10 a.u is 0.016 eV. We can compare the positions of the defect-related levels throughout the graphs in the figures above, we can note that there is no significant change in the defect level positions. Tables 8.4 and 8.5 confirm the principle of the filtration idea and this stresses that the performance of the filtration method is good and works well and is again reliable for the calculation of electronic structure.

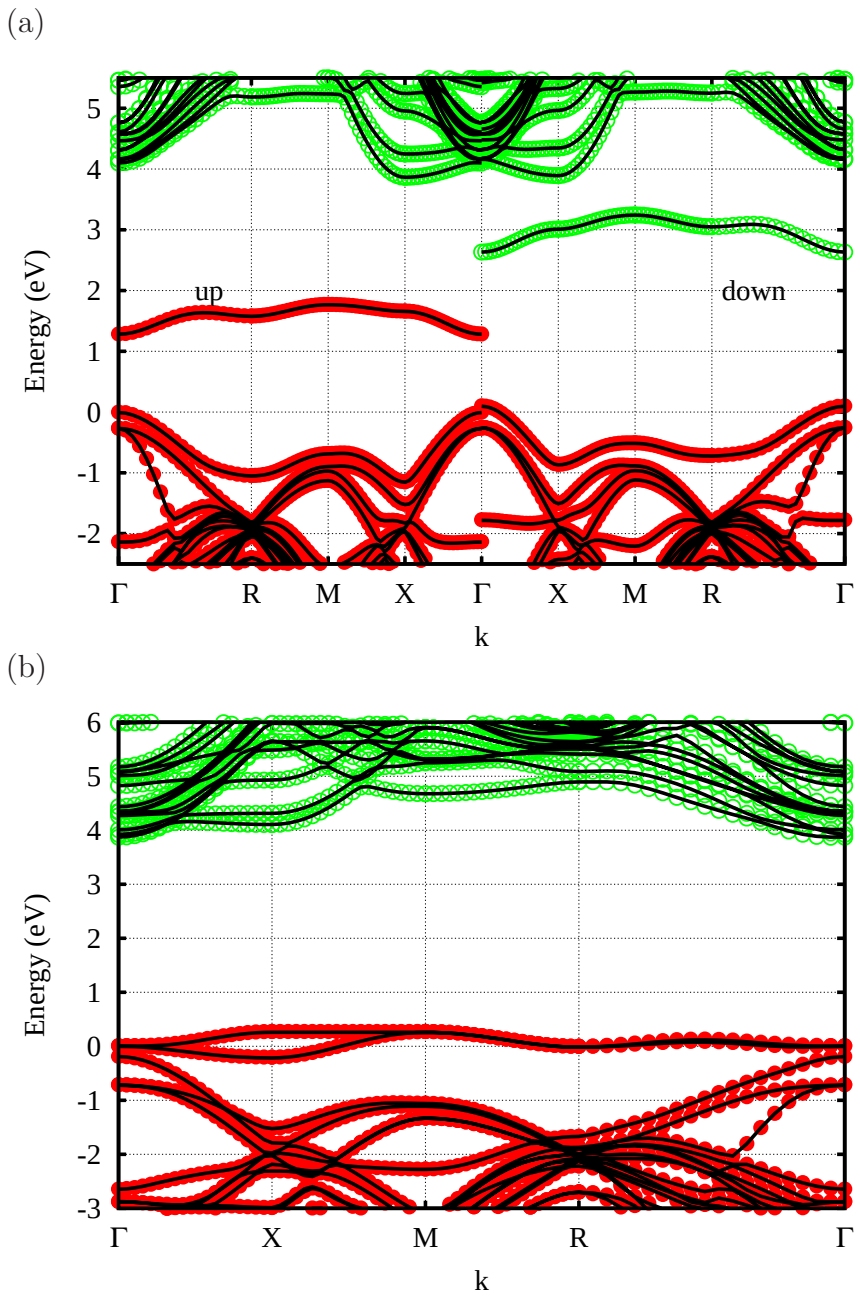

Figure 8.3: Calculated electronic band structure of (a) P1 and (b) $H1$a centres in diamond, using (R_c=∞ and R_c=8 a.u). The red and green circles show the occupied and unoccupied unfiltered bands (KS levels), and the black lines show the occupied and unoccupied filtered bands (Kohn-Sham levels), respectively.

Table 8.4: Band structure energies in eV at four k-points Γ, X, M, and R for the P1 centre in diamond, the GGA functional as a function of (R_c in a.u). VB is the valence band, DB is the defect band, and CB is the conduction band.

K-points	level	R_c			
		6	8	10	∞
Γ	VB	0.000	0.000	0.000	0.000
	DB	1.296	1.290	1.287	1.286
	DB	2.675	2.650	2.641	2.634
	CB	4.150	4.119	4.106	4.098
X	VB	-1.149	-1.148	-1.147	-1.147
	DB	1.670	1.666	1.664	1.663
	DB	3.048	3.027	3.020	3.013
	CB	3.893	3.880	3.876	3.865
M	VB	-0.683	-0.683	-0.682	-0.682
	DB	1.777	1.774	1.773	1.773
	DB	3.278	3.257	3.251	3.244
	CB	5.266	5.258	5.246	5.237
R	VB	-1.049	-1.048	-1.044	-1.043
	DB	1.589	1.582	1.583	1.582
	DB	3.087	3.062	3.057	3.051
	CB	5.224	5.199	5.194	5.189

8.5 Donor Levels for Substitutional Pnictogen Impurities

Experimental studies have found that phosphorus in diamond has donor level at E_c-0.6 eV. This is deep in comparison with similar defects in silicon and there has been

Table 8.5: Band structure energies in eV at four k-points Γ, X, M, and R for the $H1$a centre in diamond, the GGA functional as a function of (R_c in a.u). VB is the valence band, DB is the defect band, and CB is the conduction band

K-points	level	R_c			
		6	8	10	∞
Γ	VB	0.000	0.000	0.000	0.000
	DB	0.139	0.173	0.187	0.197
	CB	4.093	4.071	4.062	4.056
X	VB	-1.333	-1.333	-1.335	-1.334
	DB	-0.109	-0.053	-0.031	-0.016
	DB	0.360	0.421	0.444	0.460
	CB	4.313	4.301	4.300	4.290
M	VB	-0.869	-0.869	-0.869	-0.869
	DB	0.361	0.421	0.443	0.459
	CB	4.872	4.871	4.867	4.862
R	VB	-1.475	-1.479	-1.480	-1.481
	DB	0.087	0.146	0.169	0.184
	CB	5.099	5.085	5.086	5.083

interested in attempting to discover a shallower impurity. Computational studies [52,147–150] suggest that other group-5 impurities show as Arsenic (As) or Antimony (Sb), should give rise to shallower dopant levels. These atoms have a large volume relative to a carbon atom and this creates a compression of the surrounding diamond, giving an elastic strain energy. Previously published work has typically used 216 atom cells [148], although some larger simulations were reported in [151]. There is therefore

Table 8.6: The table compares the electrical levels (eV) for various centers in diamond from unfiltered, compared to those calculated using the formation-energy (FEM) and first principal marker methods (FPMM) of the substitutional phosphor E_c-0.6 eV [6], arsenic and antimony donor levels, which have been found using two techniques, (R_c in a.u).

Energy	Defect	R_c			
State		6	8	10	∞
		FEM			
$E_{(0/+)}$	P_s	E_v+4.249	E_v+4.218	E_v+4.173	E_v+4.132
$E_{(0/+)}$	As_s	E_v+4.378	E_v+4.351	E_v+4.350	E_v+4.320
$E_{(0/+)}$	Sb_s	E_v+4.404	E_v+4.443	E_v+4.415	E_v+4.382
		FPMM			
$E_{(0/+)}$	As_s	E_c-0.469	E_c-0.467	E_c-0.422	E_c-0.410
$E_{(0/+)}$	Sb_s	E_c-0.386	E_c-0.325	E_c-0.358	E_c-0.349
		Abs-errors			
Filt *vs* Unfilt($E_{(0/+)}$)	P_s	0.117	0.086	0.041	–
Filt *vs* Unfilt($E_{(0/+)}$)	As_s	0.058	0.031	0.030	–
Filt *vs* Unfilt($E_{(0/+)}$)	Sb_s	0.022	0.061	0.033	–
		Abs-errors			
Filt *vs* Unfilt($E_{(0/+)}$)	As_s	0.059	0.057	0.012	–
Filt *vs* Unfilt($E_{(0/+)}$)	Sb_s	0.037	0.024	0.009	–

a question as to whether larger unit cells could render the donor level shallower or deeper. This is a suitable problem for the filtration technique. Our results have studied substitutional defects P_S, As_S and Sb_S in the tetrahedral (T_d) structure in the neutral (S=$\frac{1}{2}$) and positive (S=0) charge states. The total energies have been

Table 8.7: The table compares the electrical levels (eV) for various centers in diamond from unfiltered, compared to those calculated using the formation-energy and principal marker methods of the substitutional arsenic and antimony donor levels, which have been found using two techniques, (R_c in a.u).

Energy	Defect	Cell size		
State		512	1000	1728
$E_{(0/+)}$	As_s	E_c-0.495	E_c-0.507	E_c-0.511
$E_{(0/+)}$	Sb_s	E_c-0.439	E_c-0.465	E_c- 0.478

optimised with MP 2^3 sampling. The LDA approximation has been used to treat the exchange correlation interactions. Filtration enables the supercell cell type size to be significantly increased (i.e, 216, 512, 1000, and 1728 atoms). First, however, 216 atom cells were used to validate the filtration technique.

We calculated the donor levels of the single substitutional for As and Sb in 216-atom supercells, by using the formation energy method (FEM) as indicated in section 4.5, which naturally calculates levels relative to the valence band maximum(E_v+ donor level), and the first principles marker method (FRMM) as indicated in section 4.6, which calculates levels relative to another similar impurity using experimental values for this *Marker* defect naturally leads to an answer given relative to the conduction band minimum(E_c-donor level). The phosphorus donor level which has a well known value (E_c-0.6 eV was used as the marker. From table 8.6 and by comparing the filtration results for R_c= 6, 8 and 10 a.u with the standard results for $R_c = \infty$, we can note that the mean differences for the As and Sb impurities inserted in to a 216 diamond atom are 0.040 eV and 0.042 eV, and for Sb are 0.038 eV and 0.023 eV, for the FEM and FPMM methods, respectively. The differences have been estimated by

taking the difference between filtered and unfiltered calculations, as shown in table 8.6.

Table 8.8: The table compares filtered and unfiltered timing required to calculate the total energy of three defects when using the LDA functional. $T_{filt.}$ / $T_{unfilt.}$ represents the percentage of the running time per an iteration.

Defect	Charge State	$T_{filt.}$ / $T_{unfilt.}$		
		216	512	1000
P_s	Neutral	56.33%	26.15%	9.24%
	Positive	50.49%	30.76%	8.75%
As_s	Neutral	58.77%	26.72%	8.29%
	Positive	52.57%	26.14%	9.54%
Sb_s	Neutral	53.17%	32.10%	6.95%
	Positive	52.88%	27.35%	8.58%

Our aim in this section is to examine the effect of the cell size on dopant level. It is seen from table 8.7 that, as cell size increases, levels become slightly deeper, but that the ordering P:As:Sb is unchanged.

Table 8.8 lists timings for the calculations, which show the results may be obtained significantly more efficiently using the filtration approach, with a typical speed up of a factor of four for 512 atoms and 10 from 1000 atoms. It should be remembered that this is seen in what is a very small run (with 216, 512, and 1000 atoms) and it is encouraging that even for these small systems some speed improvement is seen. For larger systems a much bigger speed up would be expected.

8.6 Decorated Ni:vacancy centers

As another test of filtration, we turn to a more complex defect, the nickel split vacancy decorated by two nitrogen atoms. This is of interest as this defect includes a transition metal atom, possibly a more challenging test of filtration. All runs in this section were performed by creating the defect in a 216 atom cubic cell of diamond, using a 2^3 Monkhorst-Pack sampling grid and with all other parameters being unaltered from the above runs.

Table 8.9: Spin polarisation energy (in eV) of Ni:V structure and energy differences (in eV) between three N-decorated structures (energies given relative to that of the C_{1h} structure which has the lowest energy). The energies are quoted to three decimal places to allow for comparison.

Defect	symmetry	R_c			
	point	6	8	10	∞
Ni-V	D_{3d}	0.187	0.174	0.184	0.176
Ni-V-2N	C_2	0.134	0.176	0.167	0.174
	C_{2h}	0.310	0.600	0.613	0.623
		Abs-errors			
Filt *vs* Unfilt	D_{3d}	0.011	0.002	0.008	-
Filt *vs* Unfilt	C_2	0.040	0.002	0.007	-
	C_{2h}	0.313	0.023	0.010	-

In these tests, C and N atoms were treated using 4 filtered functions; Ni was treated using 9 filtered functions. The GGA approximation was used to treat the exchange correlation interactions.

Initially a nickel-vacancy defect was considered in a split-vacancy structure, which can be created by placing the Ni atom at the centre of a bond between two C atoms

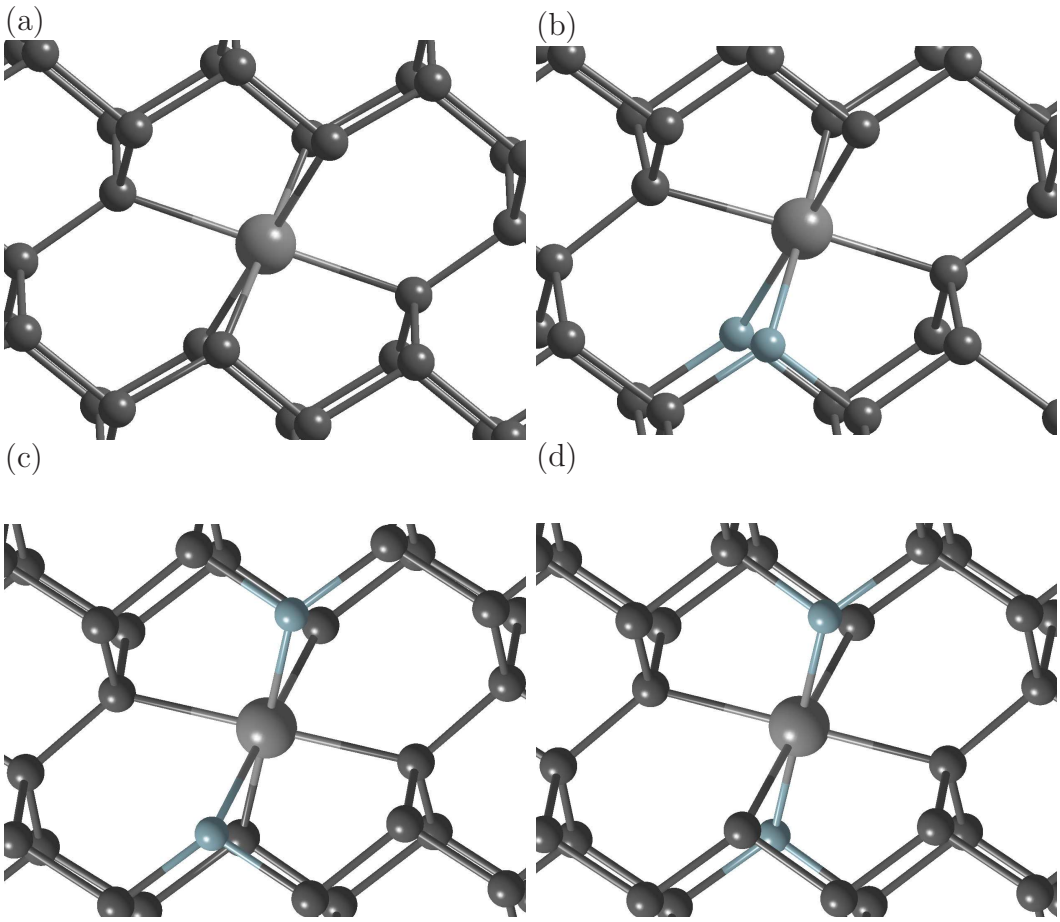

Figure 8.4: Schematic diagram showing the geometry of (a) the (Ni-V) , (b, c, and d) the (Ni-V-2N) three different sites for two nitrogen atoms. Substitutional one nickel atom and two nitrogen atoms are showing a light grey and blue colours, respectively. Horizontal and vertical directions are approximately [110] and [001], respectively.

which are then removed leaving a defect of D_{3d} symmetry. The electronic structure for this defect has a partially occupied one-electron state of e_u symmetry containing two electrons. It may be expected to have a spin S=1 ground state. In order to look at the accuracy of the filtration energy, the energy difference between the S=0 (spin averaged) and S=1 (spin polarised) fillings was considered.

This defect is often seen decorated by nitrogen atoms. Three structures containing

two N atoms were considered, as shown in figures 8.4. These have C_{1h}, C_2 and C_{2h} symmetry. The energy differences between these are not too great, and the calculation of these differences was chosen to be used as a further test for the accuracy of filtration. It is seen that the calculated energy differences are affected by filtration by a small amount of order 10 meV, comparable to findings in Table 8.9 with R_c=10 a.u and R_c=∞, quite comparable to similar calculations elsewhere in this thesis.

8.7 Calculation of Hyperfine Tensors

8.7.1 Impurity details

In this section, we present a test of the accuracy of the filtration method when calculating hyperfine tensors. For a defect to show a hyperfine coupling it must clearly have an unpaired electron and must involve a nucleus with a net spin. Defects involving N or C are therefore suitable choice in diamond. The following defects were therefore chosen to test the accuracy of filtered hyperfine calculations:

1. The P1(N_s^0) centre is a substitutional nitrogen atom in diamond, has C_{3v} symmetry in the neutral configuration, and has a single unpaired electron. This thus a good choice as a test as much experimental data is available.

2. The W24 $(N1N)^+$ [152], EPR centre in diamond has been shown to have a positive charge state, and is a trigonal defect which D_{3d} symmetry, and spin $S = \frac{1}{2}$.

3. The N1 centre $(N2N)^+$ relaxes to a trigonal structure with C_{1h} symmetry [153, 154]. It has a positive charge state, and $S = \frac{1}{2}$ configuration.

4. The most stable structure found for N4 $(N5N)^+$ has C_{2h} symmetry [155, 156], the structure has $S = \frac{1}{2}$ and positive charge.

5. The KUL1 $(Si - V)^0$ ($S = 1$) complex is transforming under the D_{3d} point group, and in the neutral charge state possesses two unpaired electrons, and the

KUL3 EPR centre has been assigned to $(\mathrm{Si}-\mathrm{H}-\mathrm{V})^0$, due to the overall C_{1h} symmetry of the defect [157].

6. The W31 EPR $(\mathrm{S_s}-\mathrm{V})^-$ centre in diamond has been relaxed to negative charge state, and to a trigonal defect (D_{3d}) symmetry, with $S=\frac{1}{2}$, which makes six bonds with six neighbours carbon atoms.

7. The substitutional site for sulphur S atom has trigonal C_{3v} symmetry, we have tested the hyperfine tensors, with positive charge state, and with $S=\frac{1}{2}$ configuration [158].

8. Bond-centre H [159–161] relaxes to a trigonal D_{3d} symmetry, the hyperfine tensors examined, with neutral charge state, and with $S=\frac{1}{2}$ configuration.

The defects all have well characterised hyperfine spectra and have previously been studied with the `AIMPRO` code.

8.7.2 Results

First-principle density functional calculations of the hyperfine interaction were made using the filtration method and compared with unfiltered (traditional) calculations and with experiment. The filtered calculations have been done in two ways, the first keeping 4 filtered functions per atom (table 8.10) and the second keeping 9 filtered functions per atom (table 8.11). These tables show the principle values of the hyperfine tensor and also the experimentally measured values. A summary showing the mean and maximum errors is given in table 8.12.

It should first be noted that the hyperfine interactions calculated using the GGA functional differ from the experimental value by an average of 9% (a typical expectation). Any comparison of the accuracy achieved by filtration should be made in the light of this underpinning uncertainty related to the approximations that are made in the GGA. It is seen in table 8.12 that with a cut-off radius of R_c= 8 a.u the mean error in the value of hyperfine tensor calculated with 4 filtered basis functions is less than

1% with this being smaller again if either R_c is increased or more filtered functions are retained. These results also show the improvement obtained by keeping 9 functions per atom, a noticeable improvement, but not dramatically so. Clearly, for large unit cells, it would be better to increase R_c to aim for better accuracy, thereby enabling a lower filtration temperature and hence ensuring 4 functions are sufficient. This is to ensure that the time–dominant step for large runs (the $O(N^3)$ diagonalisation) is being optimised. For smaller cells, it may be more efficient to keep 9 functions, running with lower R_c and higher temperature, although this approach has not been used elsewhere in this thesis.

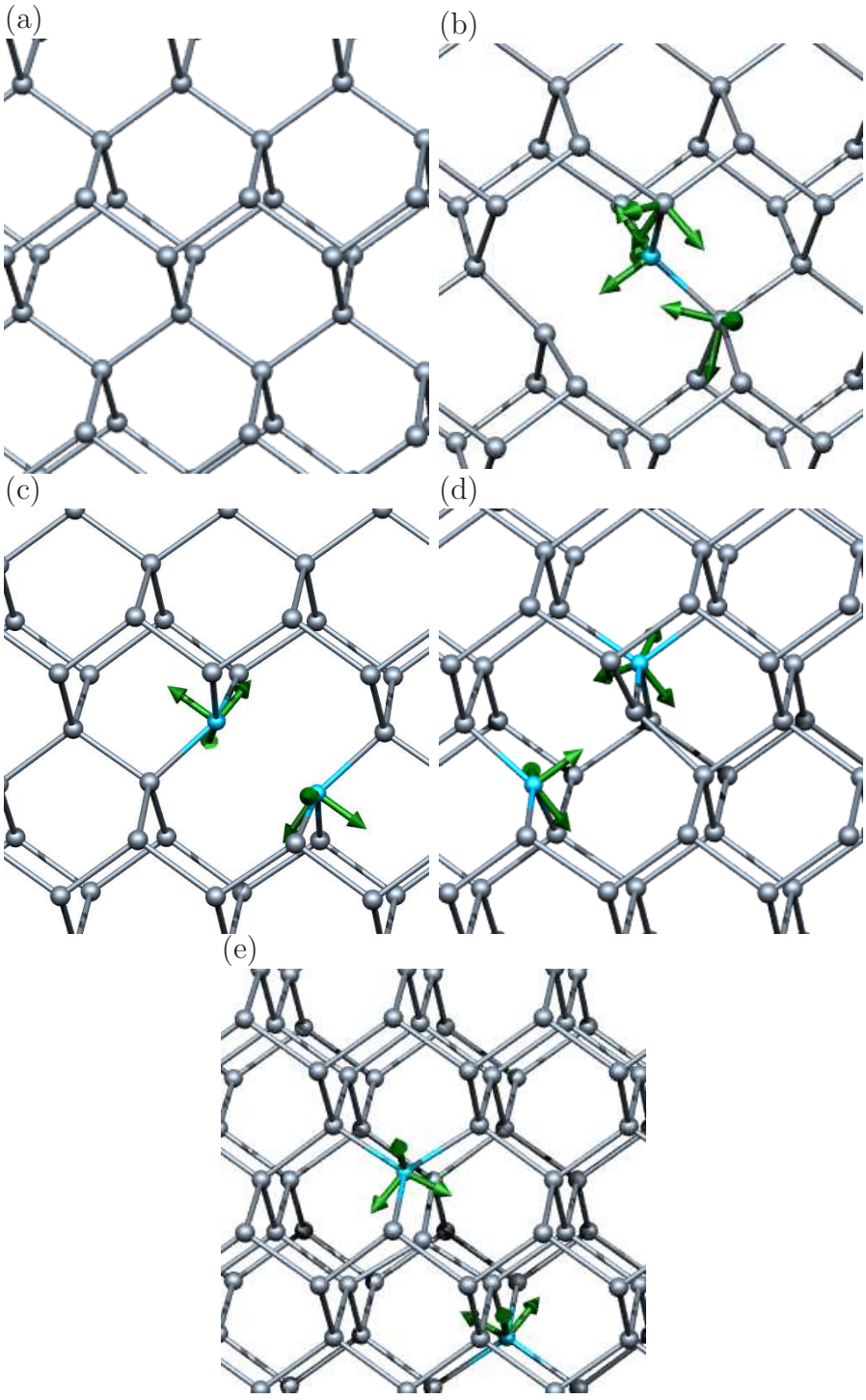

Figure 8.5: Schematic showing (a) Pure, (b) the P1, (c) N1N, (d) N2N, and (e) N5N structures and the directions of the three components of the hyperfine interactions at N atoms and a neighbouring C sites.

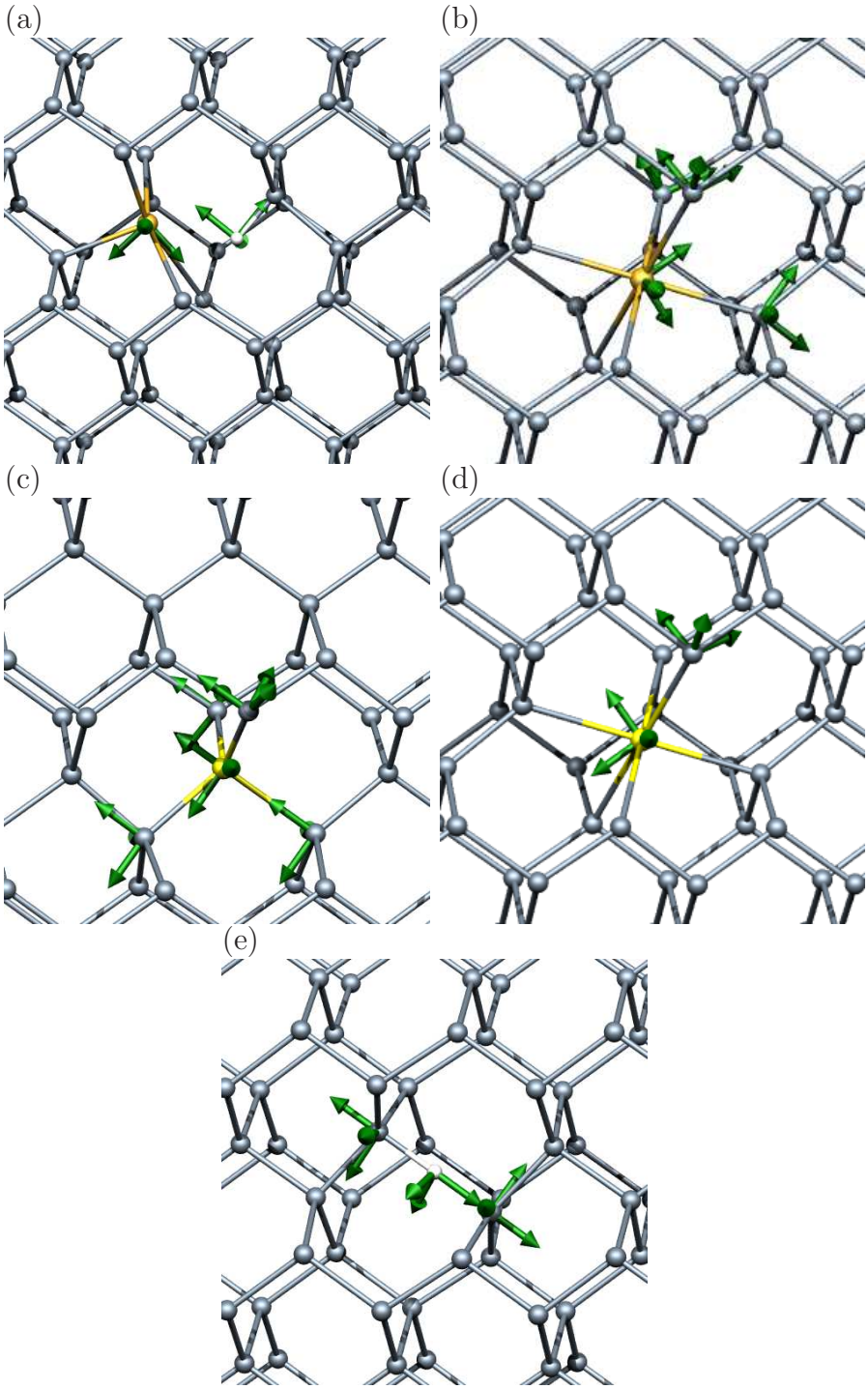

Figure 8.6: Schematic showing (a) the Si-H-V, (b) Si-V, (c) S_s, (d) W31, and (e) Bond-centre H structures and the directions of the three components of the hyperfine interactions at N atoms and a neighbouring C sites.

Table 8.10: Calculated hyperfine tensors (MHz) for N_s^0, N1N, N2N, N5N, Si-V, Si-H-V, S_s, S-V, and Bond-centre H, for the sites identified in figures 8.5 and 8.6. The defect crystallographic orientation has been chosen to facilitate comparison with experimental values [7–11], (R_c is in a.u). The filtration results have been treated using 4 filtered functions.

Site	R_c=6			R_c=8			R_c=10			R_c=∞			Exp		
	A_1	A_2	A_3	A_1	A_2	A_3	A_1	A_2	A_3	A_1	A_2	A_3	A_1	A_2	A_3
N_s^0	105.10	70.38	70.38	106.33	70.49	70.49	106.88	70.65	70.65	107.81	71.12	71.12	114.03	81.31	81.31
N1N	153.46	73.24	73.24	153.89	73.04	73.04	154.51	73.18	73.18	155.13	73.41	73.41	155.26	81.51	81.51
N2N	120.15	78.19	78.19	121.86	78.43	78.43	122.47	78.56	78.56	123.63	79.15	79.16	126.36	89.20	89.20
N5N	120.11	77.33	77.33	121.03	77.31	77.31	121.88	77.53	77.53	122.88	78.09	77.98	117.95	84.48	84.48
Si-V	78.14	81.69	81.69	78.37	82.28	82.28	78.67	82.55	82.55	78.59	82.49	82.49	76.3	78.9	78.9
Si-H-V	91.72	95.65	95.65	92.93	97.16	97.16	92.24	96.47	96.47	90.80	95.04	95.04	81.1	76.1	76.1
$S_s - V$	1068.47	1074.75	1074.75	1095.53	1102.22	1102.22	1098.31	1105.14	1105.14	1100.72	1107.68	1107.68	1034	1029	1029
S_s	150.14	53.64	53.64	161.58	54.13	54.13	163.71	54.78	54.78	166.00	56.01	56.01	-	-	-
BC-H	16.24	-39.12	-39.12	16.34	-39.17	-39.17	16.31	-39.32	-39.32	16.27	-39.50	-39.50	-	-	-

Table 8.11: Calculated hyperfine tensors (MHz) for P1, N1N, N2N, N5N, Si-V, Si-H-V(w31), S_s, S-V, and Bond-centre H, for the sites identified in figures 8.5 and 8.6. The defect crystallographic orientation has been chosen to facilitate comparison between filtered and unfiltered results with experimental values [7–11]. The filtration results have been treated using 9 filtered functions.

Site	R_c=6			R_c=8			R_c=10			$R_c = \infty$			Exp		
	A_1	A_2	A_3	A_1	A_2	A_3	A_1	A_2	A_3	A_1	A_2	A_3	A_1	A_2	A_3
N_s^0	107.23	71.09	71.09	107.39	70.94	70.94	107.81	71.10	71.10	107.81	71.12	71.12	114.03	81.31	81.31
N1N	155.37	74.10	74.10	154.89	73.44	73.44	155.05	73.43	73.43	155.13	73.41	73.41	155.26	81.51	81.51
N2N	123.15	78.99	78.99	123.15	78.99	78.99	123.48	79.09	79.09	123.63	79.15	79.16	126.36	89.20	89.20
N5N	122.20	78.08	77.97	122.36	77.89	77.78	122.72	78.04	77.92	122.88	77.98	78.09	117.95	84.48	84.48
Si-V	77.38	81.27	81.27	77.62	81.51	81.51	78.21	82.08	82.08	78.59	82.46	82.46	76.30	78.90	78.9
Si-H-V	90.63	94.78	94.29	91.27	95.49	94.97	91.34	95.57	95.07	90.80	95.54	95.04	81.1	76.1	76.1
$S_s - V$	1105.34	1112.38	1112.38	1095.38	1102.28	1102.28	1098.18	1105.14	1105.14	1100.72	1107.68	1107.68	1034	1029	1029
S_s	162.55	054.18	054.18	164.41	055.63	055.63	165.59	055.84	055.84	166.00	056.01	056.01	-	-	-
BC-H	16.29	-39.30	-39.30	16.21	-39.39	-39.39	16.25	-39.40	-39.40	16.27	-39.50	-39.50	-	-	-

Table 8.12: Maximum and mean percentage errors for principal values of the hyperfine tensor, calculated using 4 and 9 filtered basis functions, R_c is in a.u.

N o function	R_c	Max % error	Mean % error
4	6	2.973	1.387
4	8	2.346	0.982
4	10	1.586	0.632
9	6	1.539	0.560
9	8	1.234	0.405
9	10	0.595	0.173

8.8 Conclusion

This chapter has looked at a range of impurities in diamond, including naturally occurring nitrogen-containing centres; transition metal defects and potential shallow dopants. Filtration has focused on a number of properties: vibrational frequencies, ionisation energies, band structures, hyperfine couplings, thereby extending previous published tests of filtration. It has been seen that the vibrational modes are reproduced to a similar degree of accuracy to the bulk materials (percentage changes of order 0.1% relative to unfiltered calculations) and that the changes in band structure caused by filtration are of order 10 meV, again similar to results ion previous chapters for bulk materials. Binding energies are obtained to within 10 meV in energies of order 5-10 eV, again consistent with previous chapters looking at different systems. Finally, filtered basis calculations have been used to calculate hyperfine couplings, again with controlled error. It is seen in all of these tests, the filtered basis calculation is as reliable as the underpinning uncontracted Gaussian calculation, and may be used as a faster alternative for larger calculations.

Part III

Conclusions

Chapter 9

Conclusion and Future work

9.1 Conclusion

The purpose of this thesis has been to test the accuracy the filtration method, and to present the results of using density-functional theory (DFT) to recalculate some observed quantities by using a new basis set (filtered basis set). Conclusions have been presented at the end of each application's chapter, an overall summary of the findings is given in this chapter.

In studying the accuracy of the filtration approach, it must of course be understood that filtration introduces an error which can be made vanishingly small as the cut-off radius (R_c) tends to infinity. The accuracies mentioned here pertain to values of radial cutoff of 8 a.u. for diamond and 10 au for silicon, values which would be computationally efficient. In all sections of the thesis larger and smaller cut-offs have also been tested and it is almost universally the case that larger values of cutoff give much smaller errors than are quoted here.

The filtration method has been presented by Rayson and Briddon in 2009, the idea basically depending upon filtering out contributions from the unoccupied electron states from the basis set. Typically the number of basis functions per atom reaches about 40 in some cases. Simulating a system of 100 atoms, would therefore need 4000 basis functions, which would make the Hamiltonian matrix very large, and would

therefore need a large memory to store such matrices in the computer and it would be required a significant time to process. The idea of reducing the number of basis functions from 40 to 4 wave functions per atom, whilst at the same time, maintaining the accuracy of the calculation is therefore very important.

The work included in this thesis has demonstrated that for convenient choices of filtration cut-off (8 a.u. in diamond and 10 a.u. in silicon), the lattice constants and bulk modulus are modified by only 0.01%, and 0.03%, respectively with respect to the unfiltered values, a small change when considering that the difference between the GGA and experimental value is 0.06%. It has also been demonstrated that the maximum deviation in the occupied band structure (which determines the total energy and is therefore of greatest significance) is less than 20 meV. In fact errors in the lowest conduction states have been shown to be of similar size and the conduction band structure is visually reasonable for up to 5 eV in the conduction band. Filtration has also been shown to perform well for phonon frequencies, with results being perturbed by only 2 cm^{-1} in diamond or silicon, small error in frequencies of order 1000 cm^{-1}.

As a second test, the surface energies of the (111), (110) and (100) clean surfaces of diamond and silicon have been considered. During simulation, we noted that the values of surface energies produced by filtered basis calculations are in excellent agreement with conventional calculations (surface energies are changed by of 1-3 meV per 1×1 cell, with cutoff radii R_c=10 a.u. This conclusion is valid independently of functional (LDA or GGA) and surface considered. In contrast, when comparing previous theoretical calculations there is a scatter of up to 50 meV per 1×1 cell, reflecting technical differences between the calculations, such as different pseudopotentials. It should also be noted that the difference between the LDA and PBE-GGA has been shown to typically be 200 meV per 1×1 cell, a much greater change. The effect of the filtration technique on the accuracy of the calculated values of the electron affinity of H-terminated diamond has been shown to be less than 10 meV again a small change on the scale of the differences between the LDA and GGA difference 0.3 eV. These results show that the filtration algorithm is able to perform well in an extremely in-

homogeneous system. As a separate point, the use of ghost basis functions in the vacuum layer, not used in this work could be easily incorporated into a filtered basis calculation, with no overhead being felt in the ultimately time-dominant O(N^3) diagonalisation.

Studying native point defects in diamond has shown that calculations of the formation energies, binding energies and relative energies with filtered basis calculations were in good agreement with conventional results. A cutoff radius of R_c=8 a.u. was sufficient to converge these energies to around 10 eV per interstitial atom, an extremely small error when it is noted that formation energies are of order 10 eV for example. It should be noted that the energy differences relate to defects with very different structures and bonding patterns some have dangling bonds, others do not making this comparison quite challenging.

Regarding impurities in diamond, it has been shown that the absolute and percentage errors in the vibrational mode values between filtration and standard calculations, for the P1 and H1a centres were typically less than 1 cm^{-1} (less than 0.1%), respectively, an order of magnitude smaller than the difference between theoretical and experimental values, again emphasising that the effect of the filtration is small compared to the intrinsic uncertainty in the LDA and pseudopotential approximations. The accuracy of the band structures is comparable to the bulk materials described above (typically of order 10 meV in the valence states). Calculations of the ionisation energy of the P1 centre gave a similar error in comparison to an unfiltered calculation. This may be regarded as an impressive result, showing that the automatic setting of the filtration temperature and chemical potential easily copes with changes in the physical chemical potential from mid-gap to just below the conduction band in diamond. Similar agreement is produced when studying a number of other different defect centres — either defects containing transition metals or shallow impurities.

In conclusion, the work of this thesis extends previous applications of filtration which have focused only on the total energies of defects in silicon in two regards. First by looking at a greater variety of defect centres in a different material, and

secondly by studying a number of different properties, for example band structure, bulk modulus, electrical levels, ionisation energy, hyperfine coupling. All results have demonstrated an impressive accuracy, showing that a filtered basis run can replace a conventional calculation with no significant reduction in the accuracy or the predictive power of the results.

9.2 Future work

We have shown that applying the filtration method to diamond and silicon has given good results and the approach clearly shows a great ability to maintain the accuracy of calculations. Further assessment of the accuracy of the filtration method needs an analysis of its performance on other parameters. It would be important to test the method on different materials, for example, ionic materials such as ZnO and $SrTiO_3$, or on metals (where results have previously been published only for Al [33]), also applying it on molecular systems. There is no reason to doubt that the accuracy of filtration will be similar, but this should be demonstrated explicitly.

A further step that needs to be performed is the testing of filtration in the calculation of other observable properties (e.g. g-tensors or NMR shifts). The calculation of properties like this is very important for workers using $ab-initio$ calculations. Indeed, the ability to produce a large range of derived properties is one of the key strengths of these calculations and it is clearly vital that the filtration method should also be able to reproduce these accurately if it is to be uniformly used. A more challenging problem would be the calculation of electron energy loss spectra (EELS), where unoccupied states are needed in the calculation. This is more complex, as the filtration method will naturally produce less accurate conduction states unless a modification is made to the filtration technique. An assessment of the accuracy of filtration should also be made with other functionals, for example the screened-exchange now widely used for ionic materials.

A further development, important for improving the speed performance of the

filtration step to make it more competitive for small systems is the automatic setting of ε_f and kT. At present this requires additional SCF cycles, slowing down the run time. Algorithms could be developed to set these quantities locally i.e. in O(N) time rather than $O(N^3)$ as at present. A related issue is the development of an automated method for choosing functions from which the filtration projection will be performed. This is especially important in materials in which semi-core states exist, in which it may be possible to truncate the number of filtered functions used or to optimise in some other way.

Finally, there is the possibility of using a very large primitive basis and filtering from this to make the calculations more converged. This would be very advantageous as the Hamiltonian build and filtration steps (the only ones affected) are O(N) and therefore unimportant for large systems. The subsequent system-wide diagonalisations would not be affected. This essentially enables much greater accuracy to be achieved at a very small cost. It seems clear that this approach has a promising future, especially when these further steps are completed.

Bibliography

[1] C. Skylaris, P. Haynes, A. Mostofi, and M. Payne, "Using ONETEP for accurate and efficient O(N) density functional calculations," *J. Phys. Cond. Matter* **17**, pp. 5757–5769, 2005.

[2] F. Maier, J. Ristein, and L. Ley, "Electron affinity of plasma-hydrogenated and chemically oxidized diamond (100) surfaces," *Phys. Rev. B* **64**, p. 165411, Oct. 2001.

[3] J. B. Cui, J. Ristein, and L. Ley *Phys. Rev. Lett.* **81**, p. 429, 1998.

[4] P. K. Baumann and R. J. Nemanich *Phys. Rev. B* **58**, p. 1643, 1998.

[5] L. Diederich, P. Aebi, O. M. Kuttel, and L. Schlapbach *Surface Sci.* **424**, p. L314, 1999.

[6] E. Gheeraert, S. Koizumi, T. Teraji, and H. Kanda, "Electronic transitions of electrons bound to phosphorus donors in diamond," *Solid State Commun.* **113**, pp. 577–580, 2000.

[7] C. A. J. Ammerlaan, *Semiconductors, Impurities and Defects in Group IV Elements and III-V Compounds*, vol. III22B of *Landolt-Börnstein, New Series.* Springer, Berlin, 1990.

[8] A. Cox, M. E. Newton, and J. M. Baker, "ENDOR studies of the n1 di-nitrogen centre in diamond," *J. Phys. Cond. Matter* **4**, pp. 8119–8130, 1992.

[9] R. M. Mineeva and A. V. Speransky, "EPR studies on the di-nitrogen centers with nonequivalent atoms in a reddish-brown plastically deformed diamond," *Appl. Magn. Reson.* **28(3-4)**, pp. 355–364, 2005.

[10] M. F. Andrew, *Magnetic Resonance studies of Point Defects in Single crystal Diamond*. PhD thesis, University of Warwick, 2008.

[11] J. A. Van Wyk and J. H. N. Loubser *Mater. Sci. Forum* **10-12**, p. 923, 1986.

[12] R. Jones and P. R. Briddon, *The* ab initio *cluster method and the dynamics of defects in semiconductors*, vol. 51A of *Semiconductors and Semimetals*, ch. 6. Academic Press, Boston, 1998.

[13] P. R. Briddon and R. Jones, "LDA calculations using a basis of Gaussian orbitals," *Phys. Status Solidi B* **217**(1), pp. 131–171, 2000.

[14] W. Kohn and L. J. Sham, "Self-consistent equations including exchange and correlation effects," *Phys. Rev.* **140**(4A), pp. A1133–A1138, 1965.

[15] P. Hohenberg and W. Kohn, "Inhomogeneous electron gas," *Phys. Rev.* **136**(3B), pp. 864–871, 1964.

[16] M. J. Rayson and P. R. Briddon, "Rapid iterative method for electronic-structure eigenproblems using localised basis functions," *Computer Phys. Comm.* **178**, p. 128, 2008.

[17] M. J. Rayson and P. R. Briddon, "First principles method for the calculation of zero- field splitting tensors in periodic systems," *Phys. Rev. B* **77**, p. 035119, 2008.

[18] R. Jones, C. D. Latham, M. I. Heggie, V. J. B. Torres, S. Öberg, and S. K. Estreicher, "*Ab initio* calculations of the structure and dynamics of C_{60} and C_{60}^{3-}," *Phil. Mag. Lett.* **65**(6), pp. 291–298, 1992.

[19] S. K. Estreicher, C. D. Latham, M. I. Heggie, R. Jones, and S. Öberg, "Stable and metastable states of $C_{60}H$: buckminsterfullerene monohydride," *Chem. Phys. Lett.* **196**(3-4), pp. 311–316, 1992.

[20] S. Froyen and W. A. Harrison., "Elementary prediction of linear combination of atomic orbitals matrix elements," *Phys. Rev. B* **20**(6), p. 2420, 1979.

[21] J. Widany, T. Frauenheim, T. Köhler, M. Stemberg, D. Porezag, G. Jungnickel, and G. Seifert, "Density-functional-based construction of transferable nonorthogonal tight-binding potentials for B, N, BN, BH, and NH," *Phys. Rev. B* **53**(8), pp. 4443–4452, 1996.

[22] D. Porezag, T. Frauenheim, T. Köhler, G. Seifert, and R. Kaschner, "Construction of tight-binding-like potentials on the basis of density-functional theory: application to carbon," *Phys. Rev. B* **51**(19), pp. 12947–12957, 1995.

[23] L. H. Thomas, "The calculation of atomic fields," *Proc. Cambridge Philosophical Soc.* **23**, pp. 542–548, 1927.

[24] E. Fermi, "Un metodo statistice per la determinazione di alcune proprieta dell'atomo," *Rendiconti Accademia dei Lincei* **6**, pp. 602–627, 1927.

[25] J. Goodisman, "Oscillations in the thomas-fermi-dirac electron density," *Theoretica Chimica Acta* **31**(1), p. 101, 1973.

[26] M. Elstner, D. Porezag, G. Jungnickel, J. Elsner, M. Haugk, T. Frauenheim, S. Shuhai, and G. Seifert, "Self-consistent-charge density-functional tight-binding method for simulations of complex materials properties," *Phys. Rev. B* **58**(11), pp. 7260–7268, 1998.

[27] C. Skylaris, P. Haynes, A. Mostofi, and M. Payne, "Introducing ONETEP: Linear-scaling density functional simulations on parallel computers," *J. Phys. C* **122**, p. 084119, 2005.

[28] N. D. Hine, P. D. Haynes, A. A. Mostofi, C. K. Skylaris, and M. C. Payne, "Linear-scaling density-functional theory with tens of thousands of atoms:expanding the scope and scale of calculations with onetep," *Computer Phys. Comm.* **21**, p. 1041, 2009.

[29] D. R. Bowler and T. Miyazaki, "O(n) methods in electronic structure calculations," *Rep. Prog. Phys.* **75**, p. 036503, 2009.

[30] S. M. Sze, *Physics of Semiconductor Devices*, Wiley-Interscience, New York, 2nd ed., 1981.

[31] S. Barman and G. P. Srivastava, "Quantitative estimate of phonon scattering rates in different forms of diamond," *Phys. Rev. B* **73**(7), p. 073301, 2006.

[32] D. R. Lide, ed., *CRC handbook of chemistry and physics*, CRC Press, London, 75 ed., 1995.

[33] M. J. Rayson and P. R. Briddon, "Highly efficient method for kohn-sham density functional calculations of 500-10000 atom systems," *Phys. Rev. B* **80**(1), p. 205104, 2009.

[34] J. M. Thijssen, *Computational Physics*, Cambridge University Press, Cambridge, 2007.

[35] M. Born and J. R. Oppenheimer, "Zur quantentheorie der molekeln," *Ann. Phys.* **84**, p. 457, 1927.

[36] D. R. Hartree, "The wave mechanics of an atom with a non-Coulomb central field. Part 1. Theory and methods.," *Proc. Cambridge Philosophical Soc.* **24**, p. 89, 1927.

[37] V. Fock, "Näherungsmethode zur lösung des quantenmechanische mehrkörperproblems," *Z. Phys.* **61**, p. 126, 1930.

[38] J. C. Slater, "Note on Hartree's method," *Phys. Rev.* **35**(2), pp. 210–211, 1930.

[39] C. J. Roothaan, "New developments in molecular orbital theory," *Rev. Mod. Phys.* **23**(2), pp. 69–89, 1951.

[40] J. Slater, "A simplification of the Hartree Fock method," *Phys. Rev.* **81**, 1951.

[41] J. Slater and G. Koster, "Simplified LCAO method for the periodic potential problem," *Phys. Rev.* **94**, p. 1498, 1954.

[42] P. R. Briddon, "Ab initio modelling techniques applied to C-Si," in *Properties of Crystalline silicon*, ch. 6.9, pp. 300–356, INSPEC, Institute of Electrical Engineers, London, 1999.

[43] U. von Barth and L. Hedin, "A local exchange-correlation potential for the spin polarized case," *J. Phys. C* **5**, pp. 1629–1642, July 1972.

[44] J. P. Perdew and A. Zunger, "2 theorems on the self-interaction in density functional theory," *Bull. Am. Phys. Soc.* **26**(3), p. 470, 1981.

[45] J. P. Perdew and Y. Wang, "Accurate and simple analytic representation of the electron-gas correlation-energy," *Phys. Rev. B* **45**(23), pp. 13244–13249, 1992.

[46] M. E. John P. Perdew, Kieron Burke, "Generalized gradient approximation made simple," *Phys. Rev. Lett.* **77**, pp. 3865–3868, 1996.

[47] P. E. Blöchl, "Projector augmented-wave method," *Phys. Rev. B* **50**, pp. 17953–17979, Dec. 1994.

[48] M. J. Shaw, P. R. Briddon, J. P. Goss, M. J. Rayson, A. Kerridge, A. H. Harker, and A. M. Stoneham, "Importance of quantum tunneling in vacancy-hydrogen complexes in diamond," *Phys. Rev. Lett.* **95**(10), p. 105502, 2005.

[49] D. Vanderbilt, "Soft self-consisten pseudopotentials in a generalized eigenvalue formalism," *Phys. Rev. B* **41**, pp. 7892–7895, Jan. 1990.

[50] M. T. Yin and M. L.Cohen, "Theory of ab initio pseudopotential calculations," *Phys. Rev. B* **25**, pp. 7403–7412, 1982.

[51] C. Hartwigsen, S. Goedecker, and J. Hutter, "Relativistic separable dual-space gaussian pseudopotentials from H to Rn," *Phys. Rev. B* **58**(7), pp. 3641–3662, 1998.

[52] J. P. Goss, M. J. Shaw, and P. R. Briddon, "Marker-method calculations for electrical levels using gaussian-orbital basis sets," in *Theory of Defects in Semiconductors*, D. A. Drabold and S. K. Estreicher, eds., *Topics in Applied Physics* **104**, pp. 69–94, Springer, Berlin/Heidelberg, 2007.

[53] P. Pulay, *Applications of electronic structure theory*, Plenum Press, New York, 1977.

[54] D. R. Bowler and M. J. Gillan, "An efficient and robust technique for achieving self consistency in electronic structure calculations," *Chem. Phys. Lett.* **325**, pp. 473–476, 2000.

[55] G. Kresse and J. Furthmuller, "Efficient iterative schemes for ab initio total-energy calculations using a plane-wave basis set," *Phys. Rev. Lett.* **54**, pp. 11169–11186, 1996.

[56] E. Polak, *Computational methods in optimisation: a unified approach*, Academic Press, Berkley, California, USA, 1971.

[57] W. Press, *Numerical Methods in Fortran 77*, Cambridge University Press, Cambridge, UK, 1996.

[58] A. Baldereschi, "Mean-value point in the brillouin zone," *Phys. Rev. B* **7**, p. 5212, 1973.

[59] D. J. Chadi and M. L. Cohen, "Special points in the brillouin zone," *Phys. Rev. B* **8**, p. 5747, 1973.

[60] H. J. Monkhorst and J. D. Pack, "Special points for Brillouin-zone integrations," *Phys. Rev. B* **13**(12), pp. 5188–5192, 1976.

[61] D. Neuhauser *J. Phys. C* **100**, p. 5076, 1994.

[62] S. Goedecker *J. Chem. Phys.* **118**, p. 216, 1995.

[63] A. Szabo and N. S. Ostlund, *Modern Quantum Chemistry: Introduction to Advanced Electronic Structure Theory*, (Dover Press), USA, 1982.

[64] J. Ihm and M. L. Cohen *Phys. Rev. B* **21**, p. 1527, 1980.

[65] F. Birch, "Finite elastic strain of cubic crystals," *Phys. Rev.* **71**(11), p. 809, 1947.

[66] J. F. Dobson, M. P. Das, and G. Vignale, eds., *Electronic Density Functional Theory: Recent Progress & New Directions*, Kluwer Academic Publishers, New York, April 1998.

[67] R. M. Dreizler and E. K. U. Gross, *Density Functional Theory*, Springer, Berlin, 1990.

[68] J. Singh, *Physics of semiconductors and their heterostructures*, McGraw-Hill, New York, 1993.

[69] S. Logothetidis, H. M. Petalas, J. Polatoglou, and D. Fuchs, "Origin and temperature dependence of the best direct gap of diamond," *Phys. Rev. B* **46**(8), p. 4683, 1992.

[70] H. R. Philipp and E. A. Taft, "Optical properties of diamond in the vacuum ultraviolet," *Phys. Rev.* **127**, p. 159, 1962.

[71] R. A. Roberts and W. C. Walker, "Optical study of the electronic structure of diamond," *Phys. Rev.* **161**(3), p. 730, 1967.

[72] A. T. Collins, M. Stanley, and G. S. Woods, "Nitrogen isotope effects in synthetic diamonds," *J. Phys. D* **20**, pp. 969–974, 1987.

[73] S. C. Lawson, D. Fisher, D. C. Hunt, and M. E. Newton, "On the existence of positively charged single-substitutional nitrogen in diamond," *J. Phys. Cond. Matter* **10**, pp. 6171–6180, July 1998.

[74] X. Jing, N. Troullir, and J. R. Chelikowsky, "Vibrational modes of silicon nanostructures," *Solid State Commun.* **96**(4), pp. 231–235, 1995.

[75] G. M. Lopez and V. Fiorentini, "Vibrational modes of three-membered self-interstitial clusters," *Chem. of Materials* **15**, pp. 7851–7856, 2003.

[76] J. P. Goss, I. Hahn, R. Jones, P. R. Briddon, and S. Öberg, "Vibrational modes and electronic properties of nitrogen defects in silicon," *Phys. Rev. B* **67**(4), p. 045206, 2003.

[77] N. A. Besley and j. A. Bryan, "Partial hession vibrational analysis of organic moleculaes adsorbed on si(100)," *J. Phys. Chem. C* **112**, pp. 4308–4314, Nov. 2007.

[78] M. D. McCluskey, "Local vibrational modes of impurities in semiconductors," *J. Appl. Phys.* **87**(8), pp. 3593–3617, 2000.

[79] J. M. Pruneda, S. K. Estreicher, J. Junquera, J. Ferrer, and P. Ordejón, "Ab initio local vibrational modes of light impurities in silicon," *Phys. Rev. B* **65**, p. 075210, February 2002.

[80] K. Born, M. Huang, *Dynamical Theory of Crystal Lattices*, Oxford University Press, Oxford, UK, 1954.

[81] R. Jones, J. Goss, C. Ewels, and S. Öberg, "*Ab initio* calculations of anharmonicity of the C–H stretch mode in HCN and GaAs," *Phys. Rev. B* **50**(12), pp. 8378–8388, 1994.

[82] M. J. Rayson, *On Advances in the Kernal and Functionality of Ab Initio Electronic-Structure Calculations*. PhD thesis, School of Physical Sciences, University of Newcastle upon Tyne, Jan. 2005.

[83] E. Flowers, B. H. Mendoza, *Properties of matter*, University of Manchester, UK, 1985.

[84] G. D. Watkins and J. W. Corbett, "Defects in irradiated silicon. I. Electron spin resonance of the Si-*A* centre," *Phys. Rev.* **121**(4), pp. 1001–1014, 1961.

[85] W. V. Smith, P. P. Sorokin, I. L. Gelles, and G. J. Lasher, "Electron-spin resonance of nitrogen donors in diamond," *Phys. Rev.* **115**, pp. 1546–1553, September 1959.

[86] W. V. Smith, L. L. Gelles, and P. P. Sorokin, "Electron spin resonance of acceptor states in diamond," *Phys. Rev. Lett.* **2**(2), pp. 39–40, 1959.

[87] U. Gerstmann and H. Overhof, "Influence of generalized gradient approximations on theoretical hyperfine fields of paramagnetic defects," *Physica B* **273–274**, pp. 88–91, 1999.

[88] B. Hetényi, F. De Angelis, P. Giannozzi, and R. Car, "Reconstruction of frozen-core all-electron orbitals from pseudo-orbitals," *J. Chem. Phys.* **115**, pp. 5791–5795, Oct. 2001.

[89] K. W. Kolasinski, *Surface Scienc*, John Wiley & Sons Ltd, England, 2008.

[90] R. A. Wolkow, "Controlled molecular adsorption on silicon: Laying a foundation for molecular devices," *Annu. Rev. of Physical Chem.* **50**, p. 413, 1999.

[91] M. E. Ahmed, J. P. Goss, R. J. Eyre, P. R. Briddon, and M. A. Taylforth, "Theoretical investiagation on optical characteristics of functionalised silicon quantum dots," *Nanotech2010* **2**, pp. 556–559, 2010.

[92] D. J. Twitchen, *A study of defects and impurities in diamond.* PhD thesis, University of Oxford, 1997.

[93] C. B. Duke, "Surface structures of tetrahedrally coordinated semiconductors: principles,practice, and universality," *Appl. Surf. Sci.* **65**, p. 543, 1993.

[94] R. J. Needs, "Comment on should all surfaces be reconstructed," *Phys. Rev. Lett.* **71**(3), p. 460, 1993.

[95] G. P. Srivastava, "Theory of semiconductor surface reconstruction," *Rep. Prog. Phys.* **60**, p. 561, 1997.

[96] D. Wolf, "Should all surfaces be reconstructed?," *Phys. Rev. Lett.* **70**(53), p. 627, 1993.

[97] T. Frauenheim, U. Stephan, P. Blaudeck, D. Porezag, H. G. Busmann, W. Zimmermannedling, and S. Lauer, "Stability, reconstruction, and electronic-properties of diamond (100) and (111) surfaces," *Phys. Rev. B* **48**(24), pp. 18189–18202, 1993.

[98] J. Deroueta, L. Beaurya, P. Porchera, and P. J. Derenb, "Simple overlap model and crystal field analysis of Cs ZnCl:Co2 correlation with optical and magnetic properties," *J. Alloys and Compounds* **300**, p. 242, 2000.

[99] J. Stekolnikov, A. A. Furthmuller and B. F., "Absolute surface energies of group-iv semiconductors: Dependence on orientation and reconstruction," *Phys. Rev. B* **65**(10), 2002.

[100] L. Diederich, O. M. Kuttel, E. Schaller, and l. Schlapbach, "Photoemission from the negative electron affinity (100) natural hydrogen teminated diamond surface," *Surface Sci.* **349**, pp. 176–184, 1995.

[101] C. Kanai, Y. Shichibu, K. Watanabe, and Y. Takakuwa, "*Ab initio* study on surface segregation of hydrogen from diamond C(100) surfaces," *Phys. Rev. B* **65**, p. 153312, 2002.

[102] M. J. Rutter and J. Robertson, "*Ab initio* calculation of electron affinities of diamond surfaces," *Phys. Rev. B* **57**(15), pp. 9241–9245, 1998.

[103] R. Jones and P. R. Briddon, "The *ab initio* cluster method and the dynamics of defects in semiconductors," *Semiconductors and Semimetals* **51**(PtA), pp. 287–349, 1998.

[104] P. R. Briddon and M. J. Rayson, "Accurate Kohn-Sham DFT with the speed of tight binding: current techiques and future directions in materials modelling," *Phys. Status Solidi* , pp. 1–10, Mar. 2010.

[105] J. P. Perdew, K. Burke, and M. Ernzerhof, "Generalized gradiaent approximation made simple," *Phys. Rev. Lett.* **77**(18), pp. 3865–3868, 1996.

[106] C. Kittel, *Introduction to Solid State Physics*, John Wiley & Sons, Inc, Chichester, 8th ed., 2005.

[107] W. Saslow, T. K. Bergstresser, and L. C. Marvin, "Band structure and optical properties of diamond," *Phys. Rev. Lett.* **16**(9), pp. 354–356, 1966.

[108] A. T. Paul and C. E. Hathaway, "Multiphonon raman spectrum of silicon," *Phys. Rev. B* **7**, p. 3685, 1973.

[109] K. Uchinokura, T. Sekine, and E. Matsuura, "Critical-point analysis of the two-phonon Raman spectrum of silicon," *J. Phys. Chem. Solids* **35**, pp. 171–180, 1974.

[110] S. A. Solint and A. K. Ramdas, "Raman spectrum of diamond," *Phys. Rev. Lett.* **1**, 1969.

[111] G. Davies, "Decomposing the IR absorption spectra of diamonds," *Nature* **290**, pp. 40–41, 1981.

[112] P. A. temple and C. E. hathaway, "Multiphonon ramman spectrum of silicon," *Phys. Rev. B* **7**, pp. 3685–3697, April 1973.

[113] S. A. Solin and A. K. Ramdas, "Raman spectrum of diamond," *Phys. Rev. B* **4**(12), 1970.

[114] F. A. Johnson and R. Loudon *Proc. R. Soc.* **A281**, p. 274, 1964.

[115] A. K. Abdullah, K. A. Maslin, and T. J. Parker, "Observation of two-phonon difference bands in the Fir transmission spectrum of si," *Infrared Phys.* **24**(2-3), pp. 185–188, 1984.

[116] S. K. Estreicher and F. Ruymgaart, "Thermodynamics of impurities in semiconductors," *Phys. Rev. B* **70**(10), p. 125209, 2004.

[117] I. Barin, *Thermochemical Data of Pure Substances*, (VCH, Weinhem), 1995.

[118] P. W. May *Phil. Trans. R. Soc. A* **358**, p. 473, 2000.

[119] R. S. Balmer et al *J. Phys. Cond. Matter* **21**(Algorithmica), p. 364221, 2009.

[120] M. Werner, M. Adamschik, P. Gliche, E. Kohn, and H. J. Fecht, *in Proceedings of IEEE International Symposium On Industrial Electronics (ISIE 98)*, (IEEE. New York, 1998), 1998.

[121] M. Thumm, "MPACVD-diamond windows for high-power and long-pulse millimeter wave transmission," *Diamond Relat. Mater.* **10**, p. 1692, 2001.

[122] K. T. Amite, J. P. Goss, P. R. Briddon, G. W. Nick, B. H. Alton, R. Jones, H. Pinto, and M. J. Rayson, "Calculated electron affinity and stability of halogen-terminated diamond," *Phys. Rev. B* **84**(9), 2011.

[123] D. A. Yang, S. H. Drabold and J. B. Adams, "Ab initio study of diamond c(100) surfaces," *Phys. Rev. B* **48**, p. 5261, 1993.

[124] M. Zhang, Z. Wensell and J. Bernholc, "surface structures and electron affinities of bare and hydrogenated diamond c(100) surfaces," *Phys. Rev. B* **51**(8), p. 5291, 1995.

[125] C. Chu, M. P. D'Evelyn, R. H. Hauge, and J. L. Margrave, "Mechanism of diamond growth by chemical vapor deposition on diamond (100), (111), and (110) surfaces: carbon-13 studies," *J. Appl. Phys.* **70**, p. 1695, 1991.

[126] J. E. Northrup and S. Froyen *Phys. Rev. B* **50**, p. 2015, 1994.

[127] G. P. Srivastava and S. J. Jenkins *Phys. Rev. B* **53**, p. 12589, 1996.

[128] C. D. Latham, M. I. Heggie, R. Jones, and P. R. Briddon, "The energetics of hydrogenic reactions at diamond surfaces calculated by a local spin-density functional theoretical method," *Diamond Relat. Mater.* **3**(11–12), pp. 1370–1374, 1994.

[129] R. Sque, S. J. Jones and P. R. Briddon *Phys. Rev. B* **73**, p. 085313, 2006.

[130] P. K. Baumann and R. J. Nemanich, "Negative electron affinity effects on H plasma exposed diamond (100) surfaces," *Diamond Relat. Mater.* **4**, pp. 802–805, 1995.

[131] N. Eimori, Y. Mori, A. Hatta, T. Ito, and A. Hiraki, "Photoyield measurements of cvd diamond," *Diamond Relat. Mater.* **4**, p. 806, 1995.

[132] R. Sque, S. J. Jones and B. P. R. *Phys. Status Solidi A* **202**, p. 2091, 2005.

[133] N. Fall, C. J. Bingeli and A. Baldereschi *J. Phys. Cond. Matter* **11**, p. 2689, 1999.

[134] G. Kern and j. Hafner, "Ab initio calculations of the atomic electronic structure of clean and hydrogenated diamond (110) surfaces," *Phys. Rev. B* **56**, p. 4203, 1997.

[135] M. Zhang, Z. Wensell and J. Bernholc, "surface strucrures and electron affinities of bare and hydrogented diamond c(100) surfaces," *Phys. Rev. B* **51**(8), pp. 5291–5296, 1994.

[136] J. Kern, G. Hafiner and G. Kresse, "Atomic and electronic structure of diamond (111) surfaces I. reconstruction and hydrogen-induced de-reconstructuction of the one dangling- bond surface," *Surface Sci.* **366**, pp. 445–463, 1996.

[137] J. P. Goss, B. J. Coomer, R. Jones, T. D. Shaw, P. R. Briddon, M. Rayson, and S. Öberg, "Self-interstitial aggregation in diamond," *Phys. Rev. B* **63**(19), p. 195208, 2001.

[138] E. Hannah, A. Smith, M. E. Gordon Daviesa, b. Newtona, and H. Kandac, "Mapping the energy levels of the self-interstitial in diamond," *Physica B* **340-342**, pp. 111–115, 2003.

[139] P. R. Briddon and R. Jones, "Theory of impurities in diamond," *Physica B* **185**(1–4), pp. 179–189, 1993.

[140] J. S. Andrew, *A First-Principles Study on Bulk and Transfer Doping of Diamond*. PhD thesis, University of Exeter, 2005.

[141] M. H. Nazaré, "Optical and paramagnetic resonsnce properties of nickel in diamond," in *Properties and Growth of Diamond*, G. Davies, ed., *EMIS Datareviews Series*(9), ch. 4.1, pp. 129–132, INSPEC, Institute of Electrical Engineers, London, 1994.

[142] D. A. Liberman, "Slater transition-state band-structure calculations," *Phys. Rev. B* **62**(11), pp. 6851–6853, 2000.

[143] B. Bech Nielsen, K. Tanderup, M. Budde, K. Bonde Nielsen, J. L. Lindstrom, R. Jones, S. Öberg, B. Hourahine, and P. R. Briddon, "Local vibrational modes of weakly bound O–H complexes in Si," *Mater. Sci. Forum* **258–263**(Pt1–3), pp. 391–398, 1997.

[144] J. P. Goss, R. Jones, P. R. Briddon, G. Davies, A. T. Collins, A. Mainwood, J. A. Van Wyk, J. M. Baker, M. E. Newton, A. M. Stoneham, and S. C. Lawson, "Comment on "Electronic structure of the N-V center in diamond: theory"," *Phys. Rev. B* **56**(24), pp. 16031–16032, 1997.

[145] J. E. Northrup and S. B. Zhang, "Dopant and defect energetics: Si in GaAs," *Phys. Rev. B* **47**(11), pp. 6791–6794, 1993.

[146] R. Farrer, "On the substitutional nitrogen donor in diamond," *Solid State Commun.* **7**, p. 685, 1969.

[147] J. P. Goss, P. R. Briddon, S. J. Sque, and R. Jones, "Donor and acceptor states in diamond," *Diamond Relat. Mater.* **13**(4–8), pp. 684–690, 2004.

[148] S. J. Sque, R. Jones, J. P. Goss, and P. R. Briddon, "Shallow donors in diamond: Chalcogens, pnictogens, and their hydrogen complexes," *Phys. Rev. Lett.* **92**(1), p. 017402, 2004.

[149] L. G. Wang and A. Zunger, "Phosphorus and sulphur doping of diamond," *Phys. Rev. B* **66**, p. 161202(R), Apr. 2002.

[150] R. J. Eyre, J. P. Goss, P. R. Briddon, and M. G. Wardle., "Multi-impurity complexes for n-type diamond: a computational study," *Phys. Status Solidi* **204**, pp. 297–2977, Aug. 2007.

[151] R. J. Eyre, J. P. Goss, P. R. Briddon, and J. P. Hagon, "Theory of Jahn-Teller distortions of the P donor in diamond," *J. Phys. Cond. Matter* **17**, pp. 5831–5837, 2005.

[152] O. D. Tucker, M. E. Newton, and J. M. Baker, "EPR and ^{14}N electron-nuclear double-resonance measurements on the ionized nearest-neighbor dinitrogen center in diamond," *Phys. Rev. B* **50**, pp. 15586–15596, December 1994.

[153] M. Y. Shcherbakova, E. V. Sobolev, N. D. Samsonenko, and V. K. Aksenov, "Electron paramagnetic resonance of ionized nitrogen pairs in dimaond," *Sov. Phys. Solid State* **11(5)**, pp. 1104–1106, 1969.

[154] M. E. Newton and J. M. Baker, "Models for the ddi-nitrogen centres found in brown diamond," *J. Phys. Cond. Matter* **3**, pp. 3605–3616, 1991.

[155] M. Shcherbakova, E. V. Sobolev, V. E. Nadolinnyi, and V. K. Aksenov, "Defects in plastically-deformed diamonds, as idenified by optical and ESR spectra," *Sov. Phys. Dokl.* **20(11)**, pp. 725–728, 1975.

[156] C. M. Welbourn, "EPR studies of a two-nitrogen-atom centre in natural, plastically deformed diamond," *Solid State Commun.* **26**, p. 255, 1978.

[157] J. P. Goss, P. R. Briddon, and M. J. Shaw, "Density functional simulation of silicon-containing point defects in diamond," *Phys. Rev. B* **76**, pp. 75204–1, Aug. 2007.

[158] J. M. Baker, J. A. van Wyk, J. P. Goss, and P. R. Briddon, "Electron paramagnetic resonance of sulfur at a split-vacancy site in diamond," *Phys. Rev. B* **78**, p. 235203, 2008.

[159] S. Chawla and R. P. Messmer, "Hyperfine properties of bond-center muonium and hydrogen in diamond," *Appl. Phys. Lett.* **69**(21), pp. 3251–3253, 1996.

[160] G. L. Bendazzoli and O. Donzelli, "UHF calculations of hyperfine coupling constants of anomolous muonium in C, Si and Ge," *J. Phys. Cond. Matter* **1**, pp. 8227–8234, 1989.

[161] N. Paschedag, H. U. Suter, Dj. M. Maric, and P. F. Meier, "Configuration interaction calculation of hyperfine properties for bond-centered muonium in diamond," *Phys. Rev. Lett.* **70**, pp. 154–157, January 1993.